Pulsar astrometry with VLBI and beyond

Dissertation

zur

Erlangung des Doktorgrades (Dr. rer. nat.)

der

Mathematisch-Naturwissenschaflichen Fakultät

der

Rheinischen Friedrich-Wilhelms-Universität Bonn

vorgelegt von

Franz Kirsten

aus

Bernau bei Berlin

Bonn, August 2014

Angefertigt mit Genehmigung der Mathematisch-Naturwissenschaftlichen Fakulät
der

Rheinischen Friedrich-Wilhelms-Universität Bonn

1. Gutachter: Prof. Dr. Michael Kramer
2. Gutachter: Prof. Dr. Frank Bertoldi
Tag der Promotion: 20.10.2014
Erscheinungsjahr: 2014

Abstract

Stars with masses about fifteen times that of the Sun end their lives in core-collapse supernovae. The outcome of the gravitational collapse of the stellar core is a compact object known as a neutron star. Typically, these stars are observable as pulsars, highly magnetized rapidly rotating neutron stars. This thesis presents the results of two multi-epoch (global) very long baseline interferometry (VLBI) campaigns, conducted to measure the parallax and proper motion of several pulsars. In addition, it also demonstrates the implementation of, and presents the first results obtained with a new phased-array observing mode developed for global VLBI observations, aiming at performing standard pulsar timing with VLBI.

The first global VLBI campaign discussed, deals with seven observations of the globular cluster M15, spread out over a timespan of two years. The sensitivity of the observations allows us to put very tight constraints on the upper mass limit of the intermediate mass black hole (IMBH) proposed to reside at the core of the cluster. Our 3σ upper mass limit of $500\,\mathrm{M}_\odot$ is based on a non-detection of any significant radio emission. Thus, we rule out an IMBH to be the sole central object determining cluster dynamics.

In the same observations we detect two of the eight pulsars and one of the two low-mass X-ray binaries known to be hosted by M15. Moreover, we observe two further hitherto unclassified sources within the field of view of the interferometric array. We perform a parallax and proper motion analysis for all detected sources, revealing that one of the unclassified sources is a background quasar while the other one is a compact foreground source. Our astrometry of the cluster members is consistent with earlier measurements obtained from pulsar timing and improves upon the accuracy of the earlier results. For the double neutron star system M15C our data indicate that due to geodetic precession the rotational axis of the observable pulsar shifted in space moving a different part of the emission cone than that observable previously into our line of sight.

Aiming at confirming or rejecting the claim that the runaway star ζ Oph and the

pulsar B1929+10 once formed a binary system in Upper Scorpius, we observed the pulsar in another multi-epoch global VLBI campaign. In the same observations we also observed the pulsars B2020+28 and B2021+51 that were claimed to have once formed a binary system in the Cygnus Superbubble. Using our astrometric measurements we perform Monte Carlo simulations tracing the trajectory of each object back in time. The results of our simulations rule out a binary origin for both pairs B1929+10/ ζ Oph and B2020+28/ B2021+51.

Finally, in collaboration with the Joint Institute for VLBI in Europe (JIVE) we develop and test a new correlation mode for global VLBI observations. Instead of cross-correlating the data, it is summed coherently, thus mimicking a single radio antenna with the joint collecting area of all participating telescopes. Using one of the observations of the globular cluster M15, we test the algorithm on the known pulsars. We are able to detect the observed pulsars, although at a lower signal-to-noise ratio than expected.

Acknowledgement

Wow. It's been quite a ride. And a fun one, too! I believe this is actually one of the main reasons, why this thesis now exists – that I enjoyed every bit of the way. Despite the moods of my closest friends: AIPS, CASA, ParselTongue and co!
Of course, I would not have come to this point if it was not for the constant support and help – both scientifically and personally – of quite a number of people. The first one on this list are you, Wouter. I very much enjoyed being first your master student and then your Ph.D. student for two main reasons: You always gave me the room, time, and freedom that I needed, while still softly pushing me in the right direction. I especially value your constant availability, no matter whether you are at home with the kids or at a conference in South Africa. I still get worried when it takes you longer than two hours to reply to one of my e-mails. It has been a pleasure having you as my advisor, and a friend!
Michael, Huib, and Frank, besides the (very) generous financial support that you gave me throughout the last three years, I am grateful that you had me involved with your respective groups. I learned a great deal besides the main focus of my thesis and look forward to staying in contact and working with you in the future! Aard, thank you so much for all the coding and your endless patience with all my questions.
As is the case with every Ph.D. student, you need to find a way to stay sane, to take your mind off work. For me this was easy because I have you, Ines. And Karl. Coming home there was no other way than to change mental gear – both of you would always completely absorb my attention and, thus, free my mind of visibilities, coding, and the part of the paper that I did not manage to finish that day – again. You keep refreshing my batteries and put things back into perspective: Who cares about calibrating visibilities when you can change diapers or construct a wooden train track instead?
Miriam, Andrés, Matthias and Elvire, thank you so much for always having a moment to chat and sometimes even forcing me to get a cup of coffee! All of you never were just colleagues and fellow Ph.D. students but good friends instead! Sometimes going to the institute felt like going to school – soooo much gossip around! I would have totally missed out on most of it without you guys.

Reinke and Jojo. Remember? – Back in the day in either of your kitchens? I am glad I had you guys to go through all this sweet pain together. It even made solving problems from Jackson a worthwhile experience. I am so very happy that I did not take the Blue Pill!

At last, there are my dear parents. Throughout all those years you have always supported whatever I decided I would like to do – particularly morally. It is thanks to the way you raised the three of us, thanks to the cosy home we always had, that I had the confidence and strength to pursue the way that took me to this point. All I can ever hope for is to be able to carry on your philosophy of raising children and providing as cosy a home for Karl (and ??? to come) as you did for us.

Contents

List of Figures

List of Tables

1 Introduction

Radio astronomy is the area of astronomy that deals with the lower frequency range of the electromagnetic spectrum. Typical observing frequencies range from $\nu \sim 300\,\mathrm{MHz}$ to $\nu \sim 25\,\mathrm{GHz}$, but observing frequencies as low as $\nu \sim 30\,\mathrm{MHz}$ and as high as $\nu \sim 90\,\mathrm{GHz}$ are not uncommon.[1] The science targets cover all aspects of astronomy and astrophysics going from Solar System studies via Galactic and extragalactic sources all the way to cosmology. As is the case for all other observing ranges covering the spectrum from the infrared to high energy gamma-rays, also the sensitivity of radio telescopes depends on the total collecting area, the bandwidth, and the time span of the observations. For this reason, early radio observations that were conducted with small apertures (diameter $D \sim 9$ m) and limited bandwidths ($\Delta\nu \sim$a few MHz, e.g. Reber 1944) were restricted to the brightest celestial objects such as, e.g., active galactic nuclei. The construction of ever larger radio dishes – with the currently largest radio telescope being the Arecibo telescope ($D \sim 300\,\mathrm{m}$) and the Five-hundred-meter Aperture Spherical Telescope (FAST, $D \sim 500\,\mathrm{m}$, Nan et al., 2011) being under construction – and the advance in receiver technology allowing bandwidths of up to $\Delta\nu \sim 2.4\,\mathrm{GHz}$ (Ultra Broad Band reveiver[2]) ever fainter astronomical sources have become observable.

Alternatively to increasing the size of the collecting area of a radio telescope (which is physically limited by the stability and steerability of the telescope), it is also possible to combine several telescopes to form a radio interferometer. This not only has the advantage of an increased sensitivity which scales with the geometric mean of the individual collecting areas, but it also provides a higher angular resolution $\theta \propto \lambda/D$. The latter depends on the observing wavelength λ and in case of an interferometer the telescope diameter D is given by the distance between the individual telescopes. Thus, the angular resolution can be tuned by placing telescopes closer and farther apart, with the largest Earth bound separations being limited only by the diameter of Earth. The observations and derived science discussed in

[1] Here, we consider observing frequencies at and beyond 90 GHz not as classical radio frequencies but rather as belonging to mm-astronomy.

[2] `http://www3.mpifr-bonn.mpg.de/staff/pfreire/BEACON.html`

this thesis were all based on this observing technique known as very long baseline interferometry (VLBI). Similarly to single dish observations, technological advances in receiver technology and particularly in data recording and data processing hardware allowed detections of faint radio sources also with interferometers. While early interferometers, were also limited to a bandwidth of only a few MHz (e.g. Elsmore et al., 1966), modern VLBI observations are performed at recording rates of up to $2\,\mathrm{Gbit\,s^{-1}}$, allowing for bandwidths $\Delta\nu \sim 2\,\mathrm{GHz}$. Thanks to the sensitivity of observations of this kind, also faint sources such as pulsars in globular cluster (GC) – the subject of chapter 6 – can be observed.

Pulsars, the main science target of this thesis, are rapidly rotating neutron stars (spin periods $P \sim 0.001 - 10\,\mathrm{s}$) believed to be the outcome of core collapse supernovae (chapter 2.1). They are among the most compact objects (besides black holes) known in the Galaxy and as such are ideal laboratories to test the laws of physics under extreme conditions. The equation of state of neutron star matter is still under debate (e.g. Lattimer & Prakash, 2001; Gandolfi et al., 2014) but recent pulsar observations put stringent constraints on the allowed range of parameters (Antoniadis et al., 2013). Moreover, being extremely stable clocks, pulsars are ideal objects to probe the validity of different theories of gravity (e.g. Freire et al., 2012) by measuring the time of arrival of individual pulses via pulsar timing (chapter 2.3). In this thesis we focus on measuring pulsar distances and their motion within their host environment – either the Galaxy or a globular cluster – via directly measuring the positions at different times with high resolution ($\theta \sim 5\,\mathrm{mas}$) global VLBI observations. Measurements of this kind are vital to infer birth locations of pulsars and, thereby, constrain neutron star formation scenarios, pulsar ages and pulsar spin down models. In the case of pulsars in globular cluster, pulsar kinematics are excellent probes of cluster dynamics and can help to constrain the central mass distribution of GCs. Based on their stellar mass ($\sim 10^6$ solar masses, $\mathrm{M}_\odot$) and central stellar velocity dispersion, several GCs have been proposed to host an intermediate mass black hole (IMBH, $M \sim 10^{3-5}\,\mathrm{M}_\odot$) at their centre (e.g. Gebhardt et al., 2002; Gerssen et al., 2003; van der Marel & Anderson, 2010). High sensitivity, high resolution VLBI observations of these clusters can either provide direct evidence for the existence of these objects at the core of GCs by measuring their radio flux densities. Alternatively, high precision astrometry can provide such evidence indirectly by measuring the orbits of suitable compact objects, such as pulsars, in close proximity ($\leq 0.1\,\mathrm{pc}$) to the cluster core.

Besides measuring pulsar parallaxes and proper motions, a novel method for combining the data of global VLBI observations was developed as part of this thesis. In this method, the data of the individual telescopes are coherently added delivering the equivalent of a single dish radio observation with a dish that has an effective collecting area of all participating telescopes together. As such, the sensitivity of this observing mode is expected to be much higher than that of a single dish and will provide more accurate pulsar timing measurements than what any single dish radio telescope is capable of.

This thesis is organised as follows: In chapters 2 and 3 we will introduce the astronomical targets – pulsars and globular cluster – observed for this thesis while our observing technique, VLBI, will be discussed in great detail in chapter 4. Chapter 5 deals with the results obtained from observing one exemplary globular cluster, M15 (NGC 7078), where we tried to find evidence for an IMBH proposed to reside at the cluster core. The same globular cluster is also the subject of chapter 6, this time focusing on the proper motion of the cluster pulsars and other compact objects within and external to the cluster. In chapter 7 we present parallax and proper motion measurements of three further isolated pulsars obtained with global VLBI observations and discuss their implications concerning the pulsars birth locations. Chapter 8 introduces the new phased-array mode developed for VLBI observations and the first test results are discussed. In chapter 9 we summarize the main findings of this thesis.

References

Antoniadis, J., Freire, P. C. C., Wex, N., et al. 2013, Science, 340, 448

Elsmore, B., Kenderdine, S., & Ryle, Sir, M. 1966, MNRAS, 134, 87

Freire, P. C. C., Wex, N., Esposito-Farèse, G., et al. 2012, MNRAS, 423, 3328

Gandolfi, S., Carlson, J., Reddy, S., Steiner, A. W., & Wiringa, R. B. 2014, European Physical Journal A, 50, 10

Gebhardt, K., Rich, R. M., & Ho, L. C. 2002, ApJL, 578, L41

Gerssen, J., van der Marel, R. P., Gebhardt, K., et al. 2003, AJ, 125, 376

Lattimer, J. M. & Prakash, M. 2001, ApJ, 550, 426

Nan, R., Li, D., Jin, C., et al. 2011, International Journal of Modern Physics D, 20, 989

Reber, G. 1944, ApJ, 100, 279

van der Marel, R. P. & Anderson, J. 2010, ApJ, 710, 1063

2 Pulsars

In 1967 Jocelyn Bell was analysing radio observations conducted with a radio antenna consisting of 500 dipoles at Cambridge University. Jocelyn Bell was a PhD student of Antony Hewish studying quasars. While scanning through the 100s of meters of her chart-recorder paper output, she recognised a signal resembling radio frequency interference. That signal, however, was far more systematic – periodic in fact – and only appeared when the telescope was scanning one particular part of the sky. It was not before long that Bell's observation was linked to a type of star that was first proposed by Baade and Zwicky in 1934 – a neutron star. Today, about 2400 such neutron stars (NSs) that are observable as pulsars are known.

2.1 Neutron stars as pulsars

Pulsars were first detected at radio frequencies and still today the bulk of the population is only observable at these long wavelengths. Nevertheless, a considerable fraction also shows pulsed emission in the optical and in the X-ray regime. Since the launch of the Fermi Satellite (June 2008) an increasing number of radio pulsars have also been confirmed to be pulsating at $\gamma-$frequencies and, even more interestingly, many of the unidentified Fermi LAT (Large Area Telescope) sources are indeed pulsars that are not observable in the radio regime (Abdo et al., 2009; Saz Parkinson et al., 2010; Abdo et al., 2013).

In general, the pulsation periods of pulsar cover the range from a few milliseconds up to about ten seconds. There is, however, a clear bimodality in the pulse period distribution with the two peaks lying at just below one second and at about three milliseconds (Figure 2.1). The latter population is to a large part associated with binary systems and will be discussed in greater detail in the following section. Common to both populations in the radio regime is the highly linearly polarized emission (e.g. Graham-Smith, 2003) and the steep spectral energy distribution (SED) following a power law of the form $S_\nu \propto \nu^\alpha$. The canonical value for the spectral index $\alpha = -1.8 \pm 0.2$ (Maron et al., 2000) with the most recent analysis arriving at a much broader distribution $\alpha = -1.4 \pm 0.96$ (Bates et al., 2013). In any case, the

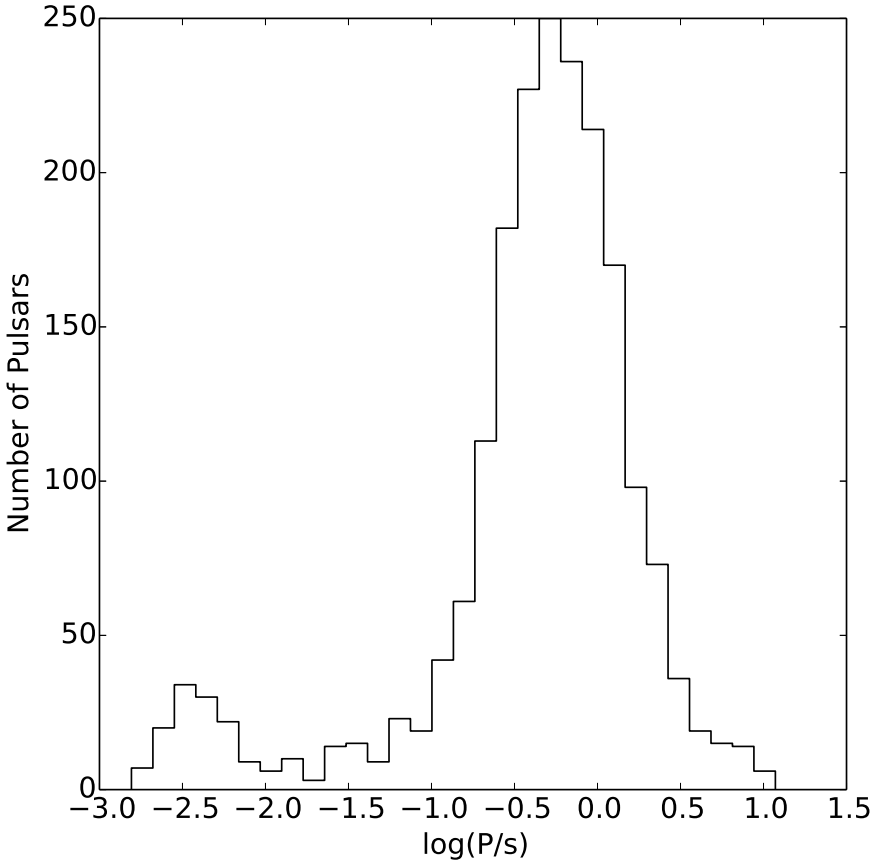

Fig. 2.1: Pulse period number counts showing a clear bimodality. Data taken from the *ATNF pulsar catalogue* (Manchester et al., 2005).

overall trend is for pulsars to have much higher flux density S_ν at low frequencies ν. In combination, the polarization characteristics and the SED point to the notion that pulsar emission is non-thermal but coherent curvature radiation instead. Thus, it originates from charged particles – mostly relativistic electrons – that are being accelerated in strong magnetic fields. Based on the extremely stable yet individually different pulsation characteristic of these signals it has been concluded that their origin must be rapidly rotating objects, whose beams of emission only strike the observer at intervals equal to the rotation rate of the emitting sources. The fact that the emission is beam-like, meaning that it is not isotropic but directional instead, together with the aforementioned spectral characteristics of the emission, points to a magnetized rotator whose rotational axis is misaligned with the magnetic field axis. The current understanding is that these objects are fast spinning neutron star with a strong dipolar magnetic field – pulsars.

The standard formation scenario for a neutron star is based on the gravitational collapse of a massive star ($8 < M_*/M_\odot < 25$, see Lattimer & Prakash 2004 for a review on NSs). At the end of its life time, such a star has burned all its nuclear fuel and, hence, radiation pressure can no longer balance the gravitational pressure. Accordingly, the star collapses under its own gravity in a process that becomes visible as a core-collapse supernova (SN, see e.g. Janka et al. 2007 for a review on SNe).[1] During the collapse of the core, most of the stellar mass is being ejected in a rebounce process forming the later observable supernova remnant (SNR). The most prominent example for an SNR is the Crab nebula hosting a 33-ms pulsar close to its centre (Lovelace et al., 1968; Comella et al., 1969).

In the core region of the former star the mass density exceeds that of atomic nuclei during collapse, leading to the capture of electrons by protons (inverse β-decay, $e^- + p^+ \rightarrow n + \nu_e$) and, hence, the formation of neutron rich nuclei and eventually a neutron gas. Finally, the core collapse leads to the formation of a compact object primarily composed of neutrons – a neutron star.[2] Further collapse of this object into a black hole is only prevented by the neutron degeneracy pressure balancing gravity. The neutrinos produced during the gravitational collapse of the core take away most ($\sim 99\%$) of the gravitational binding energy released during collapse ($\sim 10^{53}\,\mathrm{erg}$). Both the ejection of the outer layers of the former star and also the neutrino flux might be anisotropic leading to a somewhat asymmetric explosion. Only a small ($\sim 1\%$) asymmetry in either would lead to a 'kick' imparted on the collapsing core (e.g. Woosley, 1987; Janka & Mueller, 1994; Scheck et al., 2006) that is sufficient to explain the observed large (a few $100\,\mathrm{km\,s^{-1}}$) space velocities of NSs (chapter 7, Arzoumanian et al., 2002; Hobbs et al., 2005; Faucher-Giguère & Kaspi, 2006).

During core collapse, angular momentum and magnetic flux are conserved and, therefore, the newborn NS having a radius of roughly 10 km only (compared to several thousand kilometres of the progenitor star) is rotating rapidly and is highly magnetized. The spin axis and the magnetic field axis can be misaligned yielding a rotating magnetic field in space (Figure 2.2). The rotating magnetic field, in turn, induces an electric field on the surface of the NS that easily extracts charged particles from the surface into the magnetosphere of the star (see, e.g., Lorimer & Kramer, 2005). This plasma, once its density has build up sufficiently to balance

[1] Core collapse SNe are SNe Type Ib, Ic and Type II. Type Ia SN are the result of a nuclear fusion runaway process after which no remnant is left behind.

[2] The very core itself could be composed of exotic matter like pion condensates, lambda hyperons, delta isobars, and quark-gluon plasmas.

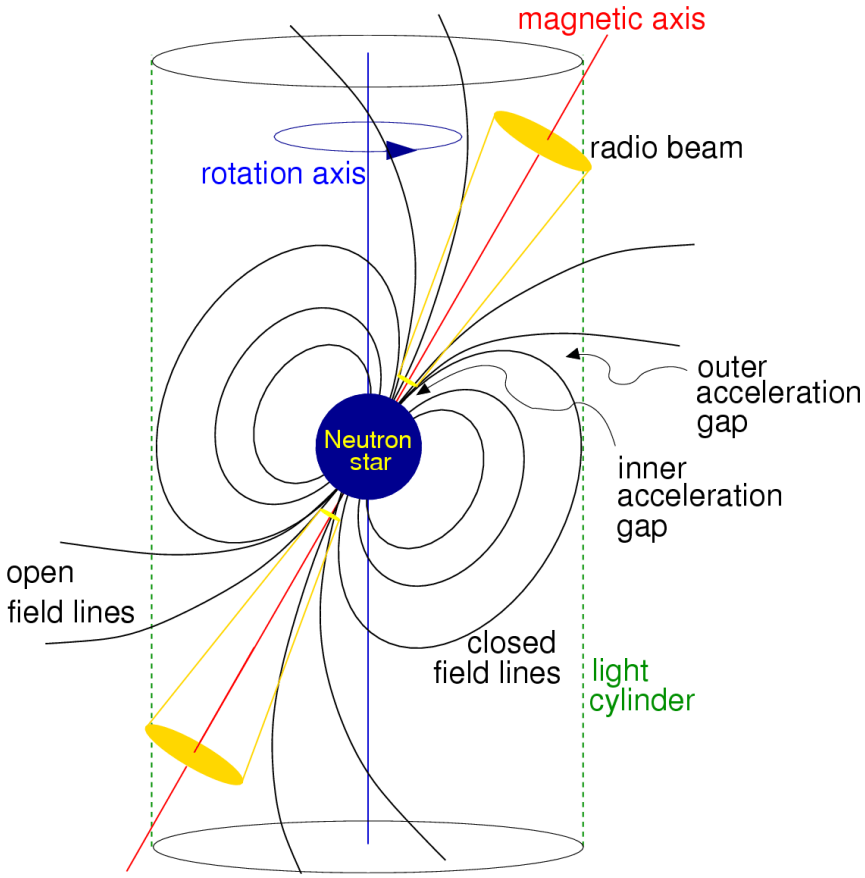

Fig. 2.2: Sketch of a pulsar showing the misalignment of the rotational and magnetic field axes. Also indicated are the possible regions where particles are accelerated to produce the observed coherent emission. Figure taken from Lorimer & Kramer (2005).

the surface electric field, couples to the magnetic field and co-rotates with the star out to the radius at which the orbital velocity is still below the speed of light. This radius defines the so-called light cylinder outside of which the field lines of the dipolar magnetic field are no longer closed. The region interior to where the first open field lines enter the NS surface is what is know as the polar cap. It is this region where the beamed emission of pulsars is thought to be produced, although the exact mechanism still eludes our understanding. Most models agree that the acceleration of charged particles to relativistic speeds must occur in a region that is depleted of plasma – a gap – such that a residual strong electric field parallel to the magnetic field lines exists. A large number of particles being accelerated while also emitting photons simultaneously are required to explain the strong coherent emission of pulsars. The reader is referred to Lorimer & Kramer (2005) for a compilation and discussion of the different mechanisms proposed to explain the observations.

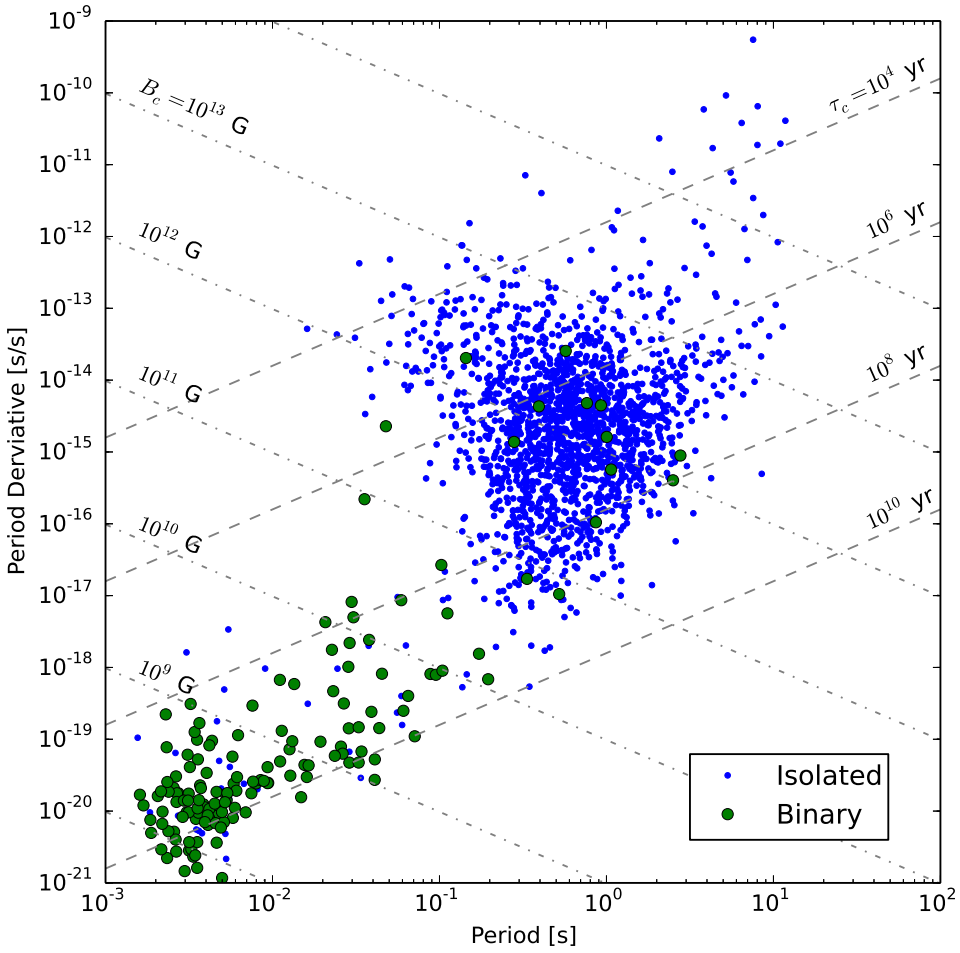

Fig. 2.3: Distribution of pulsars spin down rates as a function of spin period. Pulsars with short periods ($P < 30\,\mathrm{ms}$) are much more likely to be associated with a binary system (green circles) than the the normal ones (blue dots). Also indicated are the characteristic age, τ_c, and the characteristic magnetic field strength, B_c. Data taken from the *ATNF Pulsar Catalogue*.

2.2 Millisecond pulsars

The two main populations of neutron stars visible in the $P - \dot{P}$- diagram (Figure 2.3) differ by several orders of magnitude in both the observed pulse period P and the spin-down rate $\dot{P}$: the normal pulsars complete a full rotation in just below one second and slow down at at a rate of roughly $10^{-15}\,\mathrm{s\,s^{-1}}$ while the fast pulsars have spin periods of a few milliseconds slowing down at a much lower rate of about $10^{-20}\,\mathrm{s\,s^{-1}}$. Directly related to the two observables P and $\dot{P}$ are the characteristic age $\tau_c = P/2\dot{P}$ and the characteristic magnetic field strength at the surface of the NS $B_c \propto \sqrt{P\dot{P}}$. MSPs seem to be a lot older ($\tau_c \sim 10^{10}\,\mathrm{yr}$) and have much weaker

magnetic fields ($B_c \sim 10^8$ G) than normal NSs ($\tau_c \sim 10^7$ yr, $B_c \sim 10^{12}$ G). Both these derived values need to be treated with care, though, since they are derived under the assumption that pulsar spin-down is solely due to magnetic breaking. Magnetic braking assumes that the energy source powering the electromagnetic dipole radiation caused by the rotating magnetic field is the rotational kinetic energy of the pulsar itself. The general mathematical ansatz to describe the spin evolution of a pulsar is a simple power law of the form $\dot{P} \propto P^{2-n}$, where $n = 3$ for pure magnetic dipole radiation. The measured values for n span, however, a range from 1.4 (Lyne et al., 1996) to 2.9 (Camilo et al., 2000). Thus, further mechanisms such as the emission of a pulsar wind and also high energy emission play a role in the spin-down of a pulsar.

The key to understand the dichotomy in the pulse period distribution is the fact, that the vast majority of MSPs have a binary companion whereas the normal pulsars are mostly isolated. The broad picture is that pulsars are typically born with spin periods between a few tens up to several hundred milliseconds (Faucher-Giguère & Kaspi, 2006; Perna et al., 2008) slowing down continuously and switching off eventually. The latter is believed to be due to a decrease of the electric field strength below a critical value beyond which particles can no longer be accelerated to relativistic velocities (e.g. Ruderman & Sutherland, 1975). However, if the progenitor star was in a binary system surviving the SN or if the isolated NS encounters another star forming a new binary (e.g. in a globular cluster, cf. section 3.2), further evolution of the NS is altered significantly. Once the NS-companion evolves to a stage that it fills its Roche Lobe (or looses mass through a stellar wind), mass and angular momentum are being transferred onto the NS. During this phase, the system becomes observable as a bright X-ray source mostly because of the release of gravitational potential energy by matter that is falling onto the NS surface. Depending on the mass of the companion star these systems are classified either as low-mass X-ray binaries (LMXBs, $M_c < 1.5\,M_\odot$), as intermediate-mass X-ray binaries (IMXBs, $2 < M_c/M_\odot < 8$), or as high-mass X-ray binaries (HMXBs, $M_c > 8\,M_\odot$). The accretion of mass and, in particular, the gain in angular momentum through mass accretion, leads to an increase of the rotation rate of the NS (Lamb et al., 1973; Ghosh & Lamb, 1979). At the same time, mass accretion also induces a decay of the magnetic field strength, the exact mechanism of which is not fully understood yet. Models include ohmic dissipation caused by the increasing temperature of the NS-surface when the accreted matter undergoes nuclear burning (e.g. Geppert & Urpin, 1994; Konar & Bhattacharya, 1997; Cumming et al., 2004), the screening

of the surface magnetic field by the accreted matter (Zhang, 1998; Choudhuri & Konar, 2002; Konar & Choudhuri, 2004), and also the expulsion of magnetic flux tubes during spin-down (e.g. Jahan-Miri, 2000). Typically, the final outcome of the evolution of both stars in such a system is a recycled neutron star (a MSP) plus either a He-white dwarf (LMXB), a CO-white dwarf (IMXB), another NS or even a black hole (HMXB, Tauris & van den Heuvel, 2006).

Observational evidence for the above formation scenario of MSPs is not only given by the aforementioned membership of most MSPs in a binary system but also by the over-abundance of observed LMXBs in dense stellar systems like GCs (cf. chapter 3). In such environments the likelihood for stellar encounters and, hence, tidal capture are much larger compared to the field. Accordingly, almost half of all known MSPs are members of GCs. Most recently, very compelling evidence for the connection between a MSP and a LMXB has been presented by Patruno et al. (2014) who show that the MSP J1023+0038 is switching back and forth between being observable as an X-ray quiescent radio MSP and being observable as an actively accreting NS without any hint for radio pulsations.

2.3 Pulsar timing

Pulsars are typically observed with large single dish radio telescopes aiming at measuring the time of arrival (TOA) of individual pulses, defined as the time at which the pulse closest to the mid-point of the observation arrives (Lorimer & Kramer, 2005). Since the separation between individual pulses must be an integer multiple of the rotation period of the pulsar, the TOAs of a pulse can be predicted precisely once the TOA of a particular observational period has been measured and an accurate geometric model of the pulsar-Earth system is known. The latter, however, is quite involved and regular ($\sim$weeks to months) observations spanning long time ranges (>few years) are required to measure the basic parameters (e.g. position, parallax, proper motion) of the normal pulsars with high precision. Due to the higher spin frequency and also larger rotational stability, the TOAs of MSPs can be determined with much higher precision and, thus, it requires less time to determine the parameters mentioned above accurately.

The TOAs of a pulse are typically measured from a pulse profile that has been obtained by averaging the observations in both time and frequency. The averaging in time is performed via pulse folding which essentially means that the observational

data is split into chunks of the same length as the known rotational period. The individual chunks are then added up yielding the integrated pulse profile which has been shown to be very stable over long periods of time (as opposed to the individual pulses, see e.g. Lorimer & Kramer, 2005). Averaging the data in frequency requires an intermediate step known as de-dispersion. The broadband radio pulse emitted by the pulsars traverses the interstellar medium (ISM) on its way to Earth and, therefore, interacts with the ionized part of the ISM. Apart from scintillation (affecting the brightness of the pulse) and scattering (broadening an otherwise intrinsically sharp pulse) the pulse is being dispersed which causes lower frequencies to arrive later than higher ones. This delay needs to be compensated for before adding up the signals in the individual frequency channels. The delay Δt between the arrival times of adjacent frequencies ν_1 and ν_2 depends on the electron density n_e along the line of sight dl in the following way:

$$\Delta t\,(\nu_1 < \nu_2) = \frac{e^2}{2\pi m_e c}\left(\frac{1}{\nu_1^2} - \frac{1}{\nu_2^2}\right) \cdot \int_0^d n_e\, dl\,.$$

Here, the constants e^2, m_e, and c are the electron charge, the electron mass, and the speed of light respectively. The integral in the above expression is known as the dispersion measure (DM) which is the prime measurable to determine pulsar distances d. Obviously, using the DM to determine d requires the knowledge of n_e along a particular line of sight. Although known to be uncertain by factors of a few along some directions, the best and commonly used model of the electron distribution throughout the Galaxy is the NE2001 model published by Cordes & Lazio, 2003.

The pulse profile obtained following the recipe described above is subsequently used to measure the TOA and it is compared to a template profile and its implied TOA at the epoch of observation. In general, TOAs are computed in reference to the centre of mass of the Solar System - the so-called Solar System barycentre (SSB). This is done mostly to measure the TOAs in an inertial reference frame and it has the useful side-effect that TOAs from different telescopes can be compared. In order to perform the transformation of TOAs from the coordinate system of the telescope to the SSB an accurate ephemeris for the Solar System is required (such as DE405[3]). Furthermore, to predict the TOAs of the pulses at the SSB the pulsar intrinsic parameters summarized in the pulsar ephemeris need to be know. Those include the pulse period and its derivatives; the astrometric parameters position, proper motion and parallax; and if applicable the binary parameters. In the majority of binary

[3] `http://iau-comm4.jpl.nasa.gov/de405iom/de405iom.pdf`

systems the latter are the five Keplerian parameters orbital period (P_b), the projected semi-major orbital axis ($a \sin i$, where i is the inclination angle of the orbital plane with respect to the line of sight and a is the semi-major axis of the orbital ellipse), the orbital eccentricity (e), the longitude of periastron (ω), and the epoch of periastron (T_0). In most binaries those parameters can be considered as constants while in some – notably in the relativistic ones – the above parameters are subject to change. Within the scope of this thesis the change in the orbital period $\dot{P}_b = dP_b/dt$ is of particular interest. In general, the observed orbital period decay $\dot{P}_b^{\rm obs}$ is the superposition of an intrinsic ($\dot{P}_b^{\rm int}$) and a kinetic term ($\dot{P}_b^{\rm kin}$) (Lorimer & Kramer, 2005; Deller, 2009)

$$\dot{P}_b^{\rm obs} = \dot{P}_b^{\rm int} - \dot{P}_b^{\rm kin} \,, \tag{2.1}$$

where

$$\dot{P}_b^{\rm int} = \dot{P}_b^{\rm GW} + \dot{P}_b^{\rm drag} + \dot{P}_b^{\rm tid} + \dot{P}_b^{\dot{m}} \tag{2.2}$$

$$\dot{P}_b^{\rm kin} = \dot{P}_b^{\rm acc} + \dot{P}_b^{\rm Shk} \,. \tag{2.3}$$

The intrinsic contributions are due to gravitational wave damping ($\dot{P}_b^{\rm GW}$), an atmospheric drag ($\dot{P}_b^{\rm drag}$), tidal dissipation of the orbit ($\dot{P}_b^{\rm tid}$), and mass loss from the system ($\dot{P}_b^{\dot{m}}$). The kinetic term, on the other hand, is composed of an acceleration of both the pulsar and the SSB ($\dot{P}_b^{\rm acc}$, caused by, e.g., differential Galactic rotation, the gravitational field in a globular cluster) and a contribution from the transverse motion of the system known as the Shklovskii effect (Shklovskii, 1970)

$$\frac{\dot{P}_b^{\rm Shk}}{P_b} = \frac{v_T^2}{cd} \,, \tag{2.4}$$

where v_T^2 is the transverse velocity. The Shklovskii term is the one that is typically most poorly determined because of the large uncertainty in distance measurements obtained from the DM, and therefore, also the transverse velocity is constrained with insufficient accuracy. At this point, alternative methods to measure the distance and the proper motion of pulsars can be of help to improve the measurements of the remaining terms in $\dot{P}_b^{\rm obs}$ and, thereby, yield a more accurate overall timing model of a pulsar. The observing technique capable of supplying such an independent measurement with high enough accuracy is very long baseline interferometry (VLBI, chapter 4).

References

Abdo, A. A., Ackermann, M., Ajello, M., et al. 2009, Science, 325, 840
Abdo, A. A., Ajello, M., Allafort, A., et al. 2013, ApJS, 208, 17
Arzoumanian, Z., Chernoff, D. F., & Cordes, J. M. 2002, ApJ, 568, 289
Bates, S. D., Lorimer, D. R., & Verbiest, J. P. W. 2013, MNRAS, 431, 1352
Camilo, F., Lorimer, D. R., Freire, P., Lyne, A. G., & Manchester, R. N. 2000, ApJ, 535, 975
Choudhuri, A. R. & Konar, S. 2002, MNRAS, 332, 933
Comella, J. M., Craft, H. D., Lovelace, R. V. E., & Sutton, J. M. 1969, Nature, 221, 453
Cordes, J. M. & Lazio, T. J. W. 2003, ArXiv Astrophysics e-prints
Cumming, A., Arras, P., & Zweibel, E. 2004, ApJ, 609, 999
Deller, A. T. 2009, PhD thesis, PhD Thesis, 2009
Faucher-Giguère, C.-A. & Kaspi, V. M. 2006, ApJ, 643, 332
Geppert, U. & Urpin, V. 1994, MNRAS, 271, 490
Ghosh, P. & Lamb, F. K. 1979, ApJ, 234, 296
Graham-Smith, F. 2003, Reports on Progress in Physics, 66, 173
Hobbs, G., Lorimer, D. R., Lyne, A. G., & Kramer, M. 2005, MNRAS, 360, 974
Jahan-Miri, M. 2000, ApJ, 532, 514
Janka, H.-T., Langanke, K., Marek, A., Martínez-Pinedo, G., & Müller, B. 2007, Physics Reports, 442, 38
Janka, H.-T. & Mueller, E. 1994, A&A, 290, 496
Konar, S. & Bhattacharya, D. 1997, MNRAS, 284, 311
Konar, S. & Choudhuri, A. R. 2004, MNRAS, 348, 661
Lamb, F. K., Pethick, C. J., & Pines, D. 1973, ApJ, 184, 271
Lattimer, J. M. & Prakash, M. 2004, Science, 304, 536
Lorimer, D. R. & Kramer, M. 2005, Cambridge University Press
Lovelace, R. B. E., Sutton, J. M., & Craft, H. D. 1968, IAU Circ., 2113, 1
Lyne, A. G., Pritchard, R. S., Graham-Smith, F., & Camilo, F. 1996, Nature, 381, 497
Manchester, R. N., Hobbs, G. B., Teoh, A., & Hobbs, M. 2005, AJ, 129, 1993
Maron, O., Kijak, J., Kramer, M., & Wielebinski, R. 2000, A&AS, 147, 195
Patruno, A., Archibald, A. M., Hessels, J. W. T., et al. 2014, ApJL, 781, L3
Perna, R., Soria, R., Pooley, D., & Stella, L. 2008, MNRAS, 384, 1638
Ruderman, M. A. & Sutherland, P. G. 1975, ApJ, 196, 51
Saz Parkinson, P. M., Dormody, M., Ziegler, M., et al. 2010, ApJ, 725, 571
Scheck, L., Kifonidis, K., Janka, H.-T., & Müller, E. 2006, A&A, 457, 963
Shklovskii, I. S. 1970, Sov. Astron., 13, 562
Tauris, T. M. & van den Heuvel, E. P. J. 2006, Formation and evolution of compact stellar X-ray sources, ed. W. H. G. Lewin & M. van der Klis, 623–665
Woosley, S. E. 1987, in IAU Symposium, Vol. 125, The Origin and Evolution of Neutron Stars, ed. D. J. Helfand & J.-H. Huang, 255–270
Zhang, C. M. 1998, A&A, 330, 195

3 Globular clusters

Globular clusters (GCs) are gravitationally bound nearly spherical stellar systems that can be found in the bulge and in the halo of the Galaxy. They are composed of roughly 10^6 stars confined to a region of about $4000\,\mathrm{pc}^3$ as given by the half-light radius of GCs ($R_h < 10\,\mathrm{pc}$ for most GCs, van den Bergh 2008). The implied stellar density exceeds that of the solar neighbourhood by three orders of magnitude (Reid et al., 2002). Measurements of the metallicity of GCs have revealed that these systems formed at a very early stage in the history of the Milky Way and, hence, are among the oldest stellar systems with ages typically beyond 10 Gyr (e.g. Harris, 2010). Accordingly, all of the high mass stars that formed early during the lifetime of a GC have gone supernova by now, leaving behind compact objects such as neutron stars and black holes. Today, 157 globular clusters are known throughout the Galaxy (Harris, 1996, 2010 edition), 28 of which host a total of 144 known pulsars.[1]

3.1 Formation and evolution of globular clusters

Based on the low metallicity and small spread in Galactic GC parameters, early GC formation scenarios describe GCs as being special in the sense that they formed early on during cosmic time under very similar conditions. These models either find that GCs are the descendants of gravitationally unstable clouds of Jeans mass $m_J \approx 10^6\,\mathrm{M}_\odot$ and temperature $T \approx 10^4\,\mathrm{K}$ that collapsed shortly after recombination (Peebles & Dicke, 1968). Hence, GCs would represent the first bound stellar systems predating galaxies. The lack of intergalactic GCs and the correlation of metallicity with position in the host galaxy led Fall & Rees (1985) to develop the scenario that GCs formed in protogalactic clouds due to thermal instabilities. In both cases GCs represent stellar systems that formed from primordial gas and no further GC formation would be expected today.

Observations of high metallicity GCs in the thick disk of the Milky Way and also in elliptical galaxies infer that the progenitor clouds from which these GCs formed

[1] See the web page by Paulo Freire for a complete compilation: `http://www.naic.edu/~pfreire/GCpsr.html`.

must have been pre-enriched with heavy elements (Ashman & Zepf, 2001). Furthermore, the physical conditions required for GC formation as discussed in Fall & Rees (1985) are difficult to meet for the lowest mass galaxies that evidently host a system of GCs (Ashman & Zepf, 1998). Finally, the observed bimodality in the GC metallicity distribution for a given galaxy (e.g. Harris et al., 1992; Peng et al., 2008) and the fact that GCs can be formed in starbursts and galaxy merger events in the current epoch (Li et al., 2004; Hartwick, 2009) suggest that there is nothing particularly special about the formation process of GCs.

The current understanding of the formation of GCs is that they are the outcome of star formation in giant molecular clouds (GMCs) and that they still form under the right physical conditions in colliding and starburst galaxies in the current epoch (see Harris, 2001, for a comprehensive review). Numerical simulations show that GCs can be formed in GMCs in a Milky Way-size galaxy as early as at redshift $z \sim 12$ with the best conditions occurring at $z \sim 3-5$ (Kravtsov & Gnedin, 2005). In those simulations the GC formation efficiency as given by the ratio of final GC mass and initial mass of the parent GMC (M_{mc}) is about 10^{-3} implying $M_{mc} \sim 10^9\,M_\odot$ for the most massive GCs. The lack of molecular clouds of this mass in the Galaxy at the current epoch explains why there is no on-going GC formation in the Milky Way.

The general picture is that GCs form hierarchically from the collisions of small dense clumps of gas within the GMC. This so-called protocluster keeps on accreting or colliding with smaller mass clumps until it has grown to a point at which star formation sets in. Once this process started the protocluster turns into a star cluster and most of the gas that is not forming stars is ejected back into the parent GMC (Harris, 2001). The subsequent evolution of the cluster is driven by two main aspects: i) The initial mass function (IMF) describing the relative abundance of high and low mass stars; ii) dynamical encounters of cluster members.[2] The massive stars in the cluster evolve most quickly ending their lives in supernovae (SNe). The shocks introduced into the cluster environment by the SNe lead to the ejection of most of the cluster gas. In the majority of cluster evolution models a particular realization of the IMF is taken as a given and cluster evolution is modelled from thereon. In some scenarios the IMF of the cluster builds up gradually during the protocluster phase reflecting the dissimilar evolution timescales of high and low mass stars. In the model of Bailin & Harris (2009) the most massive stars ($M > 20\,M_\odot$) evolve

[2]The tidal field of the host galaxy also plays a role in that sense, that it decreases the volume within which gas and stars are bound to the cluster.

to the SN-stage on a timescale that is shorter than the formation timescale of low mass stars ($M < 1\,M_{\odot}$) leading to self-enrichment of the protocluster. This kind of scenario can explain the observed cluster-to-cluster spread in metallicity (Harris et al., 2006) and observational evidence can be found in Fensch et al. (2014).

Irrespective of the chosen IMF, the more massive stars not only evolve first but they also sink to towards the centre of the cluster through two-body interactions with lower mass stars. During their encounter kinetic energy is transferred from the high mass star to the low mass star (Spitzer, 1969; Vishniac, 1978) leading to what is known as mass segregation: massive stars are much more concentrated in the core region of a cluster while the low mass stars populate mostly the halo of the cluster (e.g. Gürkan et al., 2004, and references therein). Mass segregation certainly also plays a role in a rather recent observational peculiarity of many intermediate age and old globular clusters: the existence of multiple stellar populations. GCs such as NGC 2808 (Piotto et al., 2007) and NGC 6397 (Milone et al., 2012a) contain more than one main sequence indicating several stages of star formation. A further prominent example is the GC 47 Tuc (NGC 104) that hosts stars populating two distinct main sequences (Milone et al., 2012b). Additionally, Li et al. (2014) have shown that there is a radial trend of stellar age in 47 Tuc – the more metal rich stars and, hence, stars that formed at a later epoch are more concentrated towards the core region of the cluster. This observation nicely supports the models of D'Ercole et al. (2008) and also Conroy & Spergel (2011) who suggest that during the early cluster evolution the first generation of high mass stars end their lives in Type II SNe that, along with the ram pressure from the ambient medium, strip the cluster of any gas left halting further star formation. During the next several 10^8 yr the first generation lower mass stars evolve to the asymptotic giant branch losing mass that is subsequently accumulated in the central region of the cluster. Stars formed from this metal enriched gas would mostly populate the central region of the cluster and be observable as a separate stellar population. As with the first generation of stars, SNe and ram pressure again deplete the cluster of most of its gas ending the star formation cycle.

A further consequence of mass segregation and the increase of the central density of a star cluster is that the core region not only becomes hotter but also that the relaxation time in the core becomes much shorter compared to the outer regions. Accordingly, the core can be considered thermally independent of the outer halo (Heggie & Hut, 2003) evolving at a different pace. At that point the central region can be treated as an isothermal sphere heating up and contracting further due to

the negative heat capacity of this self-gravitating system. This process is referred to as core collapse and was initially introduced by Lynden-Bell & Wood (1968) as the gravo-thermal catastrophe. The collapse would go on indefinitely if it was not for the formation of several massive binaries in few-body encounters (Converse & Stahler, 2011; Tanikawa et al., 2012, 2013). These binaries heat the core region and halt further contraction. Observationally, GCs that have undergone core collapse (prominent examples are M15 and M30, McLaughlin & van der Marel, 2005) exhibit both a steady increase of luminosity and stellar velocity dispersion towards the very centre of the cluster, indicative of the high stellar density and deep potential well at the core of the cluster.

The aforementioned high stellar density and high central brightness of the GCs assumed to have undergone core collapse also led to speculations those GCs could host an intermediate mass black hole (IMBH, $M_\bullet \sim 10^{3-5}\,M_\odot$) at their centre (e.g. Bahcall & Ostriker, 1975; Newell et al., 1976). Black holes in that mass range are expected to exist since stellar mass black holes ($M_\bullet \sim 10^{1-2}\,M_\odot$, remnants of high mass stars) and also super-massive black holes (SMBH, $M_\bullet \sim 10^{6-9}\,M_\odot$, located at the centre of galaxies) have been confirmed observationally (e.g. Kormendy & Richstone, 1995; Casares, 2007). IMBHs can form in GCs both dynamically through collisions of stars (Portegies Zwart & McMillan, 2002; Gürkan et al., 2004; Portegies Zwart et al., 2004) and also through mass accretion by a stellar mass seed black hole at the core of a cluster (Vesperini et al., 2010). If such an IMBH is to reside in a GC it can be expected to be accreting material from its environment. Just like for SMBHs at the centre of galaxies, the accretion process should be detectable at both X-ray wavelength (emitted by the hot accretion disk) and radio wavelength (synchrotron emission generated in relativistic outflows). As part of this thesis the core collapse globular cluster M15 was observed at radio wavelengths to detect signatures of the proposed IMBH (see chapter 5).

3.2 Globular clusters as nursery for millisecond pulsars

As already mentioned above the majority of Galactic GCs have estimated ages exceeding $10^{10}\,\mathrm{yr}$. None of the massive ($M > 8\,M_\odot$) first generation and also none of massive second generation stars still exist today but, instead, they have gone supernova long ago forming neutron stars (NS) in the process (section 2.1). The majority of NSs and pulsars born during those early epochs in GC evolution will

have been ejected from their host GC due to the large kick they received at birth ($v_{\rm kick} \sim 400\,{\rm km\,s^{-1}}$, Hobbs et al. 2005; Faucher-Giguère & Kaspi 2006) and due to the shallow gravitational potential of GCs (escape velocity $v_{\rm esc} \sim 20\,{\rm km\,s^{-1}}$, Gnedin et al. 2002). Nevertheless, a substantial fraction ($5 - 20\%$, Drukier, 1996) of NSs remains bound to the cluster either because they were born in the low-velocity tail of the distribution or because they were born in an electron-capture supernova. The later formation channel is probably the dominating one in GCs (Ivanova et al., 2008) because it leads to ten times lower kick velocities than core-collapse SNe and can occur for both isolated stars and also in binaries (Podsiadlowski et al., 2004). In binaries the collapse is induced by accretion of matter onto an ONeMg-WD and becomes visible as Type Ia SN.

Regardless of the formation channel, due to mass segregation, a high concentration of compact remnants such as white dwarfs (WDs), neutron stars, and stellar mass black holes (BHs) can be expected in the central region of GCs. Being born in the early stages of cluster evolution, most if not all normal NSs that were observable as pulsars at some point would have faded beyond detection by today. However, the high central stellar density of GCs facilitates the formation of binary systems, including those that contain a NS and a main sequence star. As described in section 2.2, NSs can be recycled and spun up to become millisecond pulsars (MSPs, rotation periods $P < 30\,{\rm ms}$) in binary systems through transfer of mass and angular momentum. During the mass-transfer phase, such systems become observable as low-mass X-ray binaries (LMXBs, cf. section 2.2) and already forty years ago Clark (1975) noticed an over-abundance of LMXBs in GCs compared to the Milky Way disk. It was not before long that the correlation between stellar density and LMXB-abundance in GCs was established by Verbunt & Hut (1987). These authors developed the stellar encounter rate $\Gamma \propto \rho_c^{1.5} r_c^2$, where ρ_c and r_c are the core density and radius, respectively. Both the number of X-ray binaries and that of MSPs in GCs are well described using Γ (e.g. Johnston et al., 1992). Today, 302 MSPs are known throughout the Galaxy, about 50% of which reside in GCs. Moreover, only 13 pulsars of the total GC pulsar-population have rotation periods larger than 30 ms.[3]

The stellar encounter rate above is a good measure for the formation rate of the first binary system a NS might be or have been part of. However, Verbunt & Freire (2014) note that Γ does not take into account any subsequent encounters between a binary system and a further isolated star or another binary. Such encounters significantly alter the evolution of an MSP and, as shown by the authors, shape

[3] http://www.atnf.csiro.au/research/pulsar/psrcat/ , accessed 13 June 2014

the properties of the MSP-population of a GC. In particular, the rate of encounters between a binary system and a single star, $\gamma \propto \sqrt{\rho_c}/r_c$, correlates well with the number of isolated MSPs compared to the number of MSPs currently in a binary for a certain GC. The general trend outlined in Verbunt & Freire (2014) is that the higher γ the lower is the ratio between the number of binary MSPs and isolated MSPs in GCs. Furthermore, the authors show that the same high density GC are more likely to host slower MSPs than their lower density cousins. This indicates that in more dense clusters binary systems are easier disrupted hence halting the evolution of a normal pulsar to an MSP before mass transfer and spin-up are completed. Still, the subsequent formation of a secondary binary can further spin up a partially recycled MSP.

In sum, the high stellar density of GCs leads to both the formation and also destruction of binary systems. Consequently, GC pulsars as we see them today are very likely to have gone through multiple stellar encounters and, therefore, evolved in more than only one spin-up process.

In addition to formation and destruction rates of binary systems, pulsars in GCs can help to constrain further GC parameters that are otherwise difficult to obtain. Due to their mostly close proximity to the cluster core, pulsars can be used to probe cluster dynamics in terms of their orbits about the central mass and they are also excellent probes to study the motion of the GC itself (see chapter 6). The latter measurement probes the orbit of GCs about the Galaxy and, hence, allows predictions about the effects of tidal stripping on GCs. If accurate proper motions and orbits of a sufficient number of GCs are known, even the gravitational potential and mass distribution of the Milky Way can be probed.

Timing observations of GC MSPs have also revealed several MSPs with a negative spin down rate $\dot{P}$, all except two being associated with a GC. Those pulsars' observed spin down rates are clearly dominated by an acceleration along the line of sight within the host cluster gravitational potential. Phinney (1993) used the negative $\dot{P}$ of the two pulsars closest to the core of the GC M15, B2127+11A and B2127+11D, to constrain the central mass surface density and also the central mass-to-light ratio of M15. Furthermore, the large number and distribution of MSPs in the globular cluster 47 Tucanae allowed Freire et al. (2001) to put constraints on the cluster electron density. In their findings, the authors used the differential dispersion measure of pulsars located towards the closer and farther end of the cluster, assuming an otherwise homogeneous electron density along the line of sight to the MSPs.

The aforementioned influence of the gravitational field of the GC on pulsar timing also extends to the determination of binary system parameters. For a stable MSP in a close orbit ($P_b \sim$ a few hours) with another compact object (a WD, NS or a BH), it is possible to measure the orbital period decay because of the emission of gravitational waves (Weisberg & Taylor, 2005). In the case of binary-MSPs in GCs, this is, however, difficult to achieve because of the extra acceleration within the cluster potential (Eq. 2.3). Additionally, the transverse motion of the binary system contributes to the observed change in the binary period due to the Shklovskii effect (Eq. 2.4). In general, this term increases the observed value of the orbital period decay (Lorimer & Kramer, 2005) and needs to be disentangled from the cluster acceleration. On the other hand, in case the proper motion of such a binary is accurately known, and assuming general relativity is the correct description of gravity, the acceleration of the binary due to the cluster potential can be measured. The ideal way to determine the proper motion of a pulsar independent of any model is through radio interferometric observations, in particular global very long baseline interferometry. The principles of this observing mode will be discussed in the following chapter.

References

Ashman, K. M. & Zepf, S. E. 1998, Cambridge Astrophysics Series, 30
Ashman, K. M. & Zepf, S. E. 2001, AJ, 122, 1888
Bahcall, J. N. & Ostriker, J. P. 1975, Nature, 256, 23
Bailin, J. & Harris, W. E. 2009, ApJ, 695, 1082
Casares, J. 2007, in IAU Symposium, Vol. 238, IAU Symposium, ed. V. Karas & G. Matt, 3–12
Clark, G. W. 1975, ApJL, 199, L143
Conroy, C. & Spergel, D. N. 2011, ApJ, 726, 36
Converse, J. M. & Stahler, S. W. 2011, MNRAS, 410, 2787
D'Ercole, A., Vesperini, E., D'Antona, F., McMillan, S. L. W., & Recchi, S. 2008, MNRAS, 391, 825
Drukier, G. A. 1996, MNRAS, 280, 498
Fall, S. M. & Rees, M. J. 1985, ApJ, 298, 18
Faucher-Giguère, C.-A. & Kaspi, V. M. 2006, ApJ, 643, 332
Fensch, J., Mieske, S., Mueller-Seidlitz, J., & Hilker, M. 2014, ArXiv e-prints
Freire, P. C., Kramer, M., Lyne, A. G., et al. 2001, ApJL, 557, L105
Gnedin, O. Y., Zhao, H., Pringle, J. E., et al. 2002, ApJL, 568, L23
Gürkan, M. A., Freitag, M., & Rasio, F. A. 2004, ApJ, 604, 632
Harris, G. L. H., Geisler, D., Harris, H. C., & Hesser, J. E. 1992, AJ, 104, 613
Harris, W. E. 1996, AJ, 112, 1487
Harris, W. E. 2001, Globular Cluster Systems, 223
Harris, W. E. 2010, Royal Society of London Philosophical Transactions Series A, 368, 889

Harris, W. E., Whitmore, B. C., Karakla, D., et al. 2006, ApJ, 636, 90
Hartwick, F. D. A. 2009, ApJ, 691, 1248
Heggie, D. & Hut, P. 2003, The Gravitational Million-Body Problem: A Multidisciplinary Approach to Star Cluster Dynamics
Hobbs, G., Lorimer, D. R., Lyne, A. G., & Kramer, M. 2005, MNRAS, 360, 974
Ivanova, N., Heinke, C. O., Rasio, F. A., Belczynski, K., & Fregeau, J. M. 2008, MNRAS, 386, 553
Johnston, H. M., Kulkarni, S. R., & Phinney, E. S. 1992, in X-Ray Binaries and the Formation of Binary and Millisecond Radio Pulsars, 349–364
Kormendy, J. & Richstone, D. 1995, ARAA, 33, 581
Kravtsov, A. V. & Gnedin, O. Y. 2005, ApJ, 623, 650
Li, C., de Grijs, R., Deng, L., et al. 2014, ArXiv e-prints
Li, Y., Mac Low, M.-M., & Klessen, R. S. 2004, ApJL, 614, L29
Lorimer, D. R. & Kramer, M. 2005, Cambridge University Press
Lynden-Bell, D. & Wood, R. 1968, MNRAS, 138, 495
McLaughlin, D. E. & van der Marel, R. P. 2005, ApJS, 161, 304
Milone, A. P., Marino, A. F., Piotto, G., et al. 2012a, ApJ, 745, 27
Milone, A. P., Piotto, G., Bedin, L. R., et al. 2012b, ApJ, 744, 58
Newell, B., Da Costa, G. S., & Norris, J. 1976, ApJL, 208, L55
Peebles, P. J. E. & Dicke, R. H. 1968, ApJ, 154, 891
Peng, E. W., Jordán, A., Côté, P., et al. 2008, ApJ, 681, 197
Phinney, E. S. 1993, in Astronomical Society of the Pacific Conference Series, Vol. 50, Structure and Dynamics of Globular Clusters, ed. S. G. Djorgovski & G. Meylan, 141
Piotto, G., Bedin, L. R., Anderson, J., et al. 2007, ApJL, 661, L53
Podsiadlowski, P., Langer, N., Poelarends, A. J. T., et al. 2004, ApJ, 612, 1044
Portegies Zwart, S. F., Baumgardt, H., Hut, P., Makino, J., & McMillan, S. L. W. 2004, Nature, 428, 724
Portegies Zwart, S. F. & McMillan, S. L. W. 2002, ApJ, 576, 899
Reid, I. N., Gizis, J. E., & Hawley, S. L. 2002, AJ, 124, 2721
Spitzer, Jr., L. 1969, ApJL, 158, L139
Tanikawa, A., Heggie, D. C., Hut, P., & Makino, J. 2013, Astronomy and Computing, 3, 35
Tanikawa, A., Hut, P., & Makino, J. 2012, New Astronomy, 17, 272
van den Bergh, S. 2008, MNRAS, 385, L20
Verbunt, F. & Freire, P. C. C. 2014, A&A, 561, A11
Verbunt, F. & Hut, P. 1987, in IAU Symposium, Vol. 125, The Origin and Evolution of Neutron Stars, ed. D. J. Helfand & J.-H. Huang, 187
Vesperini, E., McMillan, S. L. W., D'Ercole, A., & D'Antona, F. 2010, ApJL, 713, L41
Vishniac, E. T. 1978, ApJ, 223, 986
Weisberg, J. M. & Taylor, J. H. 2005, in Astronomical Society of the Pacific Conference Series, Vol. 328, Binary Radio Pulsars, ed. F. A. Rasio & I. H. Stairs, 25

4 Very long baseline interferometry

The sensitivity and the angular resolution of a telescope both increase with the angular diameter D of the collecting area. Since pulsars are rather faint radio sources at large distances from Earth (one of the closest known pulsar is the MSP J0437-4715 at $d = 157 \pm 2.4\,\mathrm{pc}$, Verbiest et al. 2008) big radio dishes are needed to detect the bulk of the pulsar population. Even the biggest radio telescopes currently in operation do not, however, provide sufficient angular resolution to directly measure the parallax and the proper motion of pulsars in the image plane.[1] The parallax and proper motion of pulsars are typically on the order of mas and $\mathrm{mas\,yr^{-1}}$, respectively, while the angular resolution at a typical pulsar observing frequency of $\nu = 1.4\,\mathrm{GHz}$ of the largest radio telescope, the Arecibo Observatory ($D \approx 300\,\mathrm{m}$) is $\theta = 1.22\frac{\lambda}{D} \approx 3\,\mathrm{arcmin}$. The solution is to employ radio interferometry which combines two or more telescopes to mimic a single dish with a diameter equal to that of the largest separation of any two dishes being part of the telescope array. The biggest separation between any two telescopes – also known as the longest baseline – is achievable with telescopes spread across the globe ($D \approx 10000\,\mathrm{km}$)[2]. This observing technique is called very long baseline interferometry (VLBI).

4.1 Principles of VLBI

Typically, radio interferometric observations are performed with arrays consisting of a large number of telescopes. The principle observables that are obtained from such measurements are, however, the responses of pairs of antennas only. In the following I will show the main steps of the derivation of the response of an interferometer. For a full description see, e.g., Thompson (1999).

In order to understand the principles of radio interferometry it suffices to consider a basic two-element aperture as depicted in Figure 4.1. The two telescopes are separated by a distance $\boldsymbol{b}$ and observe a source in the direction of $\mathbf{s}$. In general it is

[1] It is possible in the time domain with pulsar timing, though (cf. section 2.3).

[2] Even longer baselines are achievable when a radio telescope in space, such as RadioAstron (Kardashev et al., 2013), is involved.

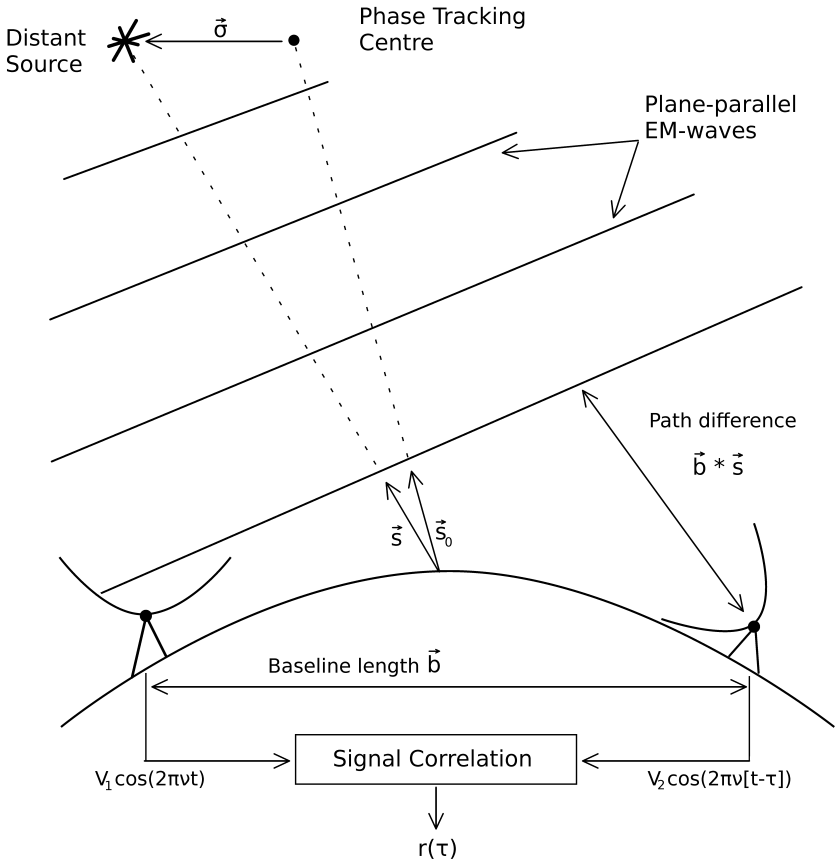

Fig. 4.1: 2-Element interferometer observing a source in the far-field.

sufficient to consider the far-field regime in which the arriving electro-magnetic waves can be approximated as plane waves since the majority of astrophysical sources are at large distances from Earth, i.e. far beyond the Solar System. The time of arrival of a wave front at one antenna lags behind that at the other antenna by the geometric time delay τ because of a simple difference in path length

$$\tau = \frac{\boldsymbol{b} \cdot \mathbf{s}}{c}\,, \tag{4.1}$$

where c is the speed of light. The responses of the individual antennas to the signal are sinusoidal voltages $V_1(t) = V_1 \cos(2\pi\nu t)$ and $V_2(t) = V_2 \cos(2\pi\nu\,[t-\tau])$, respectively. The combination of the two signals is performed via cross-correlation which is defined as the time average of the product of the two signals. The output power $r\,(\tau)$ of this correlator is thus

$$r(\tau) = \langle V_1(t)\, V_2(t) \rangle = V_1 V_2 \cos(2\pi\nu\tau)\,. \tag{4.2}$$

The product of the amplitudes V_1 and V_2 is a representation of the total power

received from the source and depends on both the specifications of the array, i.e. the effective collecting area $A(\mathbf{s}) = \sqrt{A_1(\mathbf{s}) \cdot A_2(\mathbf{s})}$ and the bandwidth of the receiver system $\Delta\nu$, as well as the source properties, i.e. the specific surface brightness $I(\mathbf{s})$ and the two dimensional angular extent S. Hence, the output power can be described by the following integral over the solid angle $d\Omega$:

$$r = \Delta\nu \int_S A(\boldsymbol{s}) I(\boldsymbol{s}) \cos(2\pi\nu\tau) d\Omega \,. \tag{4.3}$$

The correlation of the data from the individual telescopes is always performed for one particular position within the field of view (FOV) – typically the pointing centre of all telescopes. This is the so-called phase-tracking centre lying in the direction of the unit vector $\hat{\mathbf{s}}_0$ such that $\mathbf{s} = \hat{\mathbf{s}}_0 + \boldsymbol{\sigma}$ (Figure 4.1). Rewriting Eq. 4.3 in terms of $\hat{\mathbf{s}}_0$ yields:

$$\begin{aligned} r =& \Delta\nu \cos\left(\frac{2\pi\nu \boldsymbol{b} \cdot \hat{\boldsymbol{s}}_0}{c}\right) \cdot \int_S A(\boldsymbol{\sigma}) I(\boldsymbol{\sigma}) \cos\frac{2\pi\nu \boldsymbol{b} \cdot \boldsymbol{\sigma}}{c} d\Omega \\ & - \Delta\nu \sin\left(\frac{2\pi\nu \boldsymbol{b} \cdot \hat{\boldsymbol{s}}_0}{c}\right) \cdot \int_S A(\boldsymbol{\sigma}) I(\boldsymbol{\sigma}) \sin\frac{2\pi\nu \boldsymbol{b} \cdot \boldsymbol{\sigma}}{c} d\Omega \\ =& A_0 |V| \Delta\nu \cos\left(\frac{2\pi\nu \boldsymbol{b} \cdot \hat{\boldsymbol{s}}_0}{c} - \phi_v\right) . \end{aligned} \tag{4.4}$$

In the last step the complex visibility function

$$V = |V| \cdot e^{i\phi_v} = \int_S A_r(\boldsymbol{\sigma}) I(\boldsymbol{\sigma}) e^{-i2\pi\nu \boldsymbol{b}\cdot\boldsymbol{\sigma}/c} d\Omega \tag{4.5}$$

is introduced. The parameter $A_r(\boldsymbol{\sigma}) = A(\boldsymbol{\sigma})/A_0$ denotes the antenna response relative to its maximal value A_0 when the source position falls directly into the beam centre of the antenna. In Eq. 4.4 it becomes obvious that the amplitude and the phase of the correlator output are measures for the amplitude and the phase of the visibility function, respectively. On the other hand, Eq. 4.5 reveals that the visibility phase carries the information about the position of the source relative to the phase tracking centre. Hence, $\phi_\nu = 0$ implies immediately $\boldsymbol{\sigma} = 0$ meaning the source is located in the direction of $\hat{\boldsymbol{s}}_0$.

Thus far, only a monochromatic observation was considered but in reality observations are conducted at as large a bandwidth $\Delta\nu$ as possible to achieve maximal sensitivity. To properly account for this fact, Eq. 4.4 needs to be integrated over the bandwidth $\Delta\nu$. For a rectangular bandpass with a central frequency ν_0 the integration yields:

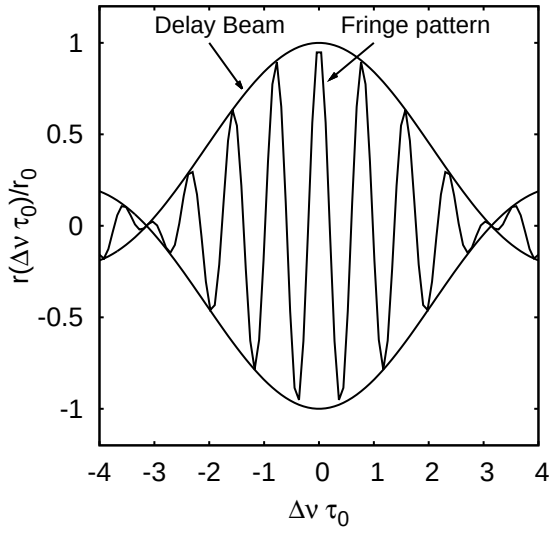

Fig. 4.2: Output of the correlator scaled by its maximum value r_0 when $\Delta\nu\tau_0 = 0$. The larger the chosen bandwidth the narrower the delay beam will be.

$$\begin{aligned} r =& A_0|V| \int_{\Delta\nu} \cos\left(2\pi\nu\tau_0 - \phi_v\right) d\nu \\ =& A_0|V|\Delta\nu\,\mathrm{sinc}(\Delta\nu\tau_0)\,\cos\left(2\pi\nu_0\tau_0 - \phi_v\right)\,. \end{aligned} \tag{4.6}$$

Due to the finite bandwidth and the geometric time delay a dampening term called the delay beam appears. For $\Delta\nu\tau_0 > 1$ the signal will be attenuated considerably (Figure 4.2) if not accounted for. Therefore, to counteract this effect the geometric delay at the phase tracking centre is being compensated for by introducing an instrumental delay τ_i just before correlation. In the ideal case $\tau_0 - \tau_i \ll 1$ such that $r \approx A_0|V|\Delta\nu\,\cos(\phi_\nu)$. Typically, the phase tracking centre and the pointing centre of the individual antennas coincide since this is where the response of each antenna is maximal. However, the instrumental delay can also be used to steer the beam of the interferometer throughout the FOV of the array such that

$$r = A_0|V|\Delta\nu\cos(\delta_{\nu_0} - \phi_\nu) \tag{4.7}$$

where the phase term $\delta_{\nu_0} = 2\pi\nu_0(\tau_0 - \tau_i)$ describes the location relative to which positions of sources within the FOV are measured.

The ultimate goal of measuring $|V|$ and ϕ_ν is to recover the intensity distribution of the source on the plane of the sky as it enters the visibility function in Eq. 4.5. In order to so, one defines the uvw-coordinate system which relates the coordinates

of the antennas with those of the celestial objects (Figure 4.3). In that scheme, the source vector **s** is given by the direction cosines

$$\boldsymbol{s} = (\cos\alpha, \cos\beta, \cos\gamma) = (l,\, m,\, \sqrt{1-l^2-m^2})\,, \tag{4.8}$$

while the baseline vector $\boldsymbol{b}$ has components $(u,\, v,\, w)$ and is measured in wavelength $\lambda = c/\nu$:

$$b = \lambda(u,\, v,\, w)\,. \tag{4.9}$$

With this definition of coordinates the visibility function can be rewritten to read

$$\begin{aligned} V\,(u,\, v) &= \int_{-\infty}^{\infty}\int_{-\infty}^{\infty} A_r(l,m) I(l,m) e^{(-2\pi i[ul+vm+w(\sqrt{1-l^2-m^2}-1)])} \frac{dldm}{\sqrt{1-l^2-m^2}} \\ &\approx \int_{-\infty}^{\infty} I(l,m) e^{-2\pi i(ul+vm)} dldm\,, \end{aligned} \tag{4.10}$$

where in the final step it is assumed that the correlation is performed at, or at least close to, the pointing centre such that $A_r(0,0) \approx 1$. Furthermore, the sources observed in interferometric observations are located at small angular distances from the phase tracking centre such that $|l|,\, |m| \ll 1$. Hence, the visibility function as derived in Eq. 4.10 is simply the Fourier transform of the intensity distribution of the source.

In order to reconstruct $I(l,m)$, the visibility function needs to be sampled at as many points in the uv-plain as possible. This is achieved by several means: i) the inclusion of a large number of antennas at varying distances from one-another to increase the number of individual baselines[3]; ii) observing at a large bandwidth which is sampled at a large number of individual frequencies (channels) and, hence, mimicking different baselines (Eq. 4.9); and iii) observe for long periods of time and employ what is known as Earth rotation synthesis. The latter takes advantage of the fact that the relative position vector of the antennas – the baseline **b** – to the source direction changes constantly during Earth rotation. Therefore, each integration time t_i yields a new sample of the visibility function and, hence, the intensity distribution $I(l,m)$.

The recovery of $I(l,m)$ is performed through Fourier inversion and deconvolution in a process called imaging. Since the visibility function is sampled discretely at

[3]The total number of baselines formed by an array of N antennas is given by $N(N-1)/2$.

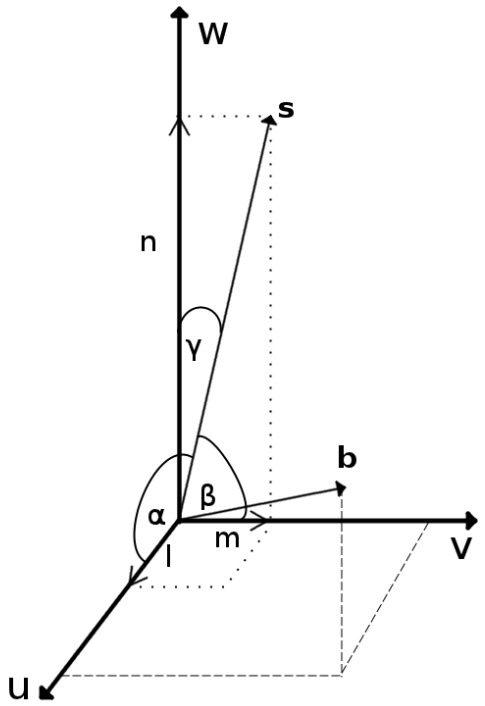

Fig. 4.3: Coordinate system used to relate the location of radio telescopes on Earth (baseline **b**) with those of celestial objects (in direction of **s**). The u- and v-axes point towards East and North, respectively, while w points towards the phase tracking centre $\hat{\mathbf{s}}_0$.

individual integration times t_i and frequency channels ν_i equation 4.10 becomes a sum over the 2n visibilities[4] which after inversion reads

$$I^D(l_s, m_s) = K \cdot \sum_{k=0}^{2n} V(u,v) \cdot S(u,v) \cdot e^{2\pi i(u_k l_s + v_k m_s)} \,. \tag{4.11}$$

Here, $K = (2n+1)^{-1}$ is a normalization factor. The superscript D in the above equation indicates that at this stage the intensity distribution is a convolution of the real intensity distribution with the point spread function of the array – the so called *dirty beam*

$$B(l_s, m_s) = \sum_{k=0}^{2n} S(u,v) e^{2\pi i(u_k l_s + v_k m_s)} \,, \tag{4.12}$$

where

$$S(u,v) = \sum_{k=0}^{2n} W_k \delta^2(u - u_k, v - v_k) \tag{4.13}$$

[4]The intensity distribution of a celestial object is a real quantity and, hence, the visibility function is hermitian yielding two measurements at once: $V(u,v) = V^*(-u,-v)$.

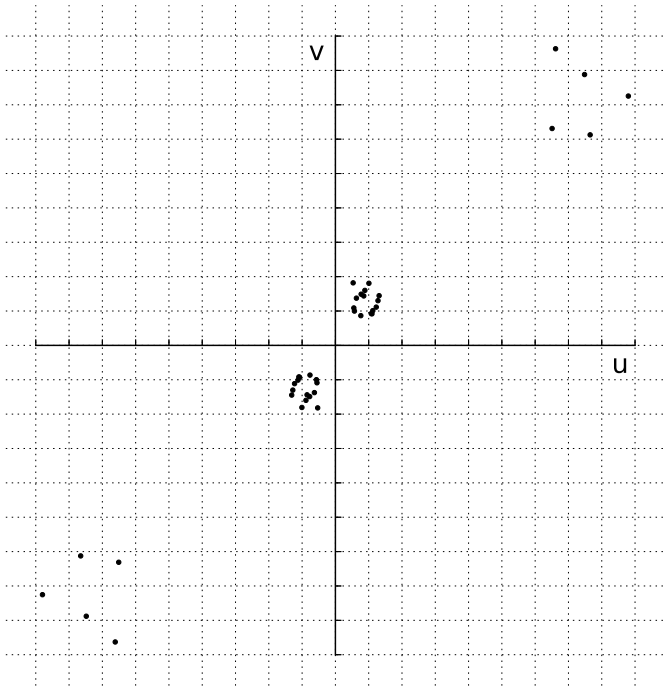

Fig. 4.4: Sketch of individual measurements of visibilities in the uv-plane - the data points in the third quadrant are the complex conjugates of the measurements in the first quadrant. Short baselines are closer to the origin and typically also more numerous than the long baselines. Therefore, weighting schemes either putting the same weight to each individual measurement or to each grid cell influence the beam shape and sensitivity to achieve the highest resolution or highest sensitivity, respectively.

is the weighted (weights W_k) sampling function discretizing $V(u, v)$. Hence, to reconstruct the real intensity distribution the *dirty image* (Eq. 4.11) and the *dirty beam* need to be deconvolved. This is typically done following the CLEAN algorithm (Högbom, 1974) and variants thereof.

In Eq. 4.13 the weights W_k can be chosen to emphasize certain visibilities more than others influencing the shape of the interferometer beam. In case visibilities representing shorter baselines have the highest weights, the weighting scheme is called natural weighting while emphasis on longer baselines is achieved through uniform weighting. Since a typical VLBI-array consists of more short than long baselines, the weighting schemes are achieved by either assigning the same weight to each point in the *uv*-plane (natural, focus on sensitivity) or the same weight to each grid-cell in the *uv*-plane (uniform, focus on high angular resolution, Figure 4.4) . At this point it is important to note that the longer the smallest baseline of

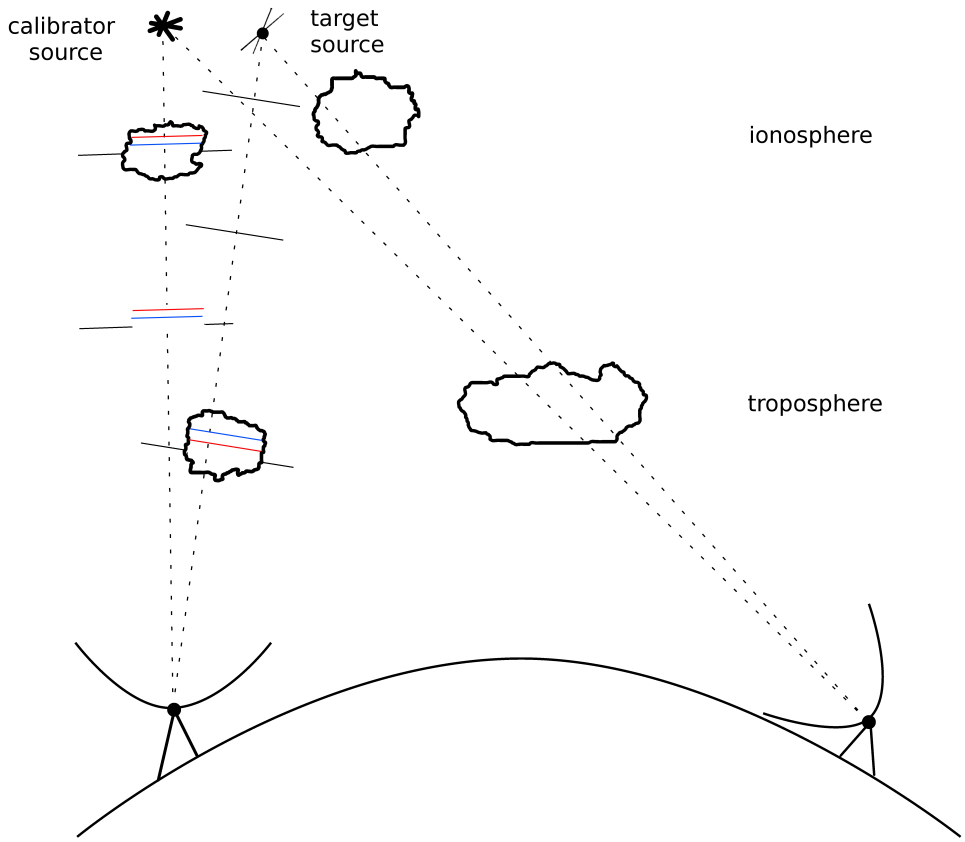

Fig. 4.5: Lines of sight crossing different parts of the atmosphere towards calibrator source and target for two different telescopes. For the left telescope the dispersive ($\propto \nu^{-1}$) and the non-dispersive ($\propto \nu$) phase delay of the ionosphere and the troposphere, respectively, are indicated (ν_1(blue) $> \nu_2$(red)).

an interferometer is, the smaller is the angular scale at which the array is sensitive to emission. This is to say that extended emission of sources – where extended means larger than the full-width-half-maxium (FWHM, $\theta = 1.22\frac{\lambda}{D_{\mathrm{min}}}$) of the shortest baseline of length D_{min} – is simply resolved out.

4.2 Calibration of interferometric data

Since this thesis deals mainly with the accurate measurement of positions of pulsars, the focus of the calibration procedure is set on phase calibration. Of course, the amplitudes of the visibilities and, hence, the information on the flux density is also calibrated but it is of minor interest for the position measurements. The reader is referred to, e.g., Fomalont & Perley (1999) for a discussion on amplitude calibration.

As described in the previous section, the data from radio interferometric obser-

vations are correlated at a specific location in the FOV given by the introduced instrumental time delay τ_i. In the ideal case, τ_i is chosen to compensate for the geometric time delay τ_0 such that the fringe phase ϕ_ν is equal to zero at the phase tracking centre for all individual frequency channels ν_i at all integration times t_i. In reality, however, the geometric model for the computation of τ_0 and, hence, τ_i, is of finite accuracy resulting in a residual phase error. For VLBI observations, factors like, e.g., different receiver backends, time offsets between the individual telescopes, and Doppler shifts introduced by the dissimilar velocity of each telescope relative to the source add to the complexity of synchronizing the time of arrival of a wave front at each telescope. All these technical issues can, however, be predicted to a sufficient degree of accuracy.

Entirely unpredictable and hence more importantly, the ionosphere and the troposphere of Earth introduce a dispersive ($\propto \nu^{-1}$) and a non-dispersive ($\propto \nu$) phase error, respectively (e.g. Chatterjee et al., 2004). This is especially true for VLBI observations since – as opposed to smaller, connect radio interferometers like the Westerbork Telescope or the Jansky Very Large Array – each antenna of the array looks through very different parts of the constantly changing atmosphere (Figure 4.5). As a result, fringe phase offsets $\Delta\phi_\nu(t)$, fringe rates $d\phi_\nu/dt$, and phase slopes $d\phi_\nu/d\nu$ affect the correlated data leading, in the worst case, to complete decorrelation. These phase errors can be modelled and accounted for provided the phase tracking centre coincides with the position of a strong point source. For this source, $\phi_\nu = d\phi_\nu/dt = d\phi_\nu/d\nu = 0$ for all telescope pairs by definition (Eq. 4.5) and any offsets can be compensated for[5]. This calibration step is commonly referred to as *fringe fitting*. Eventually, positions of sources within the FOV of the array will be measured relative to the position of this source. This type of calibration is referred to as in-beam calibration because the calibrator source lies within the beam observing the target source. Due to the limited number of suitable calibrator sources it is very rare, though, that the target object and the calibrator lie within the same beam.

Typically, the source of interest is either rather faint, its position is not accurately known and, hence, might be located far from the phase tracking centre, or it is not a point source at all. In the latter case, the source might exhibit structure which, if forced to resemble a point source by the method described above, will introduce phase errors and substructure to otherwise point sources within the FOV. Therefore, radio interferometric observations always include the observations of at least one nearby – within a few degrees – calibrator (point) source with an accurately known

[5]except for a $2n\pi$-ambiguity

position and morphology.[6] The data is then calibrated using a technique called phase referencing: Observations are performed in such a way that the antennas nod back and forth between calibrator and target source every few minutes to maintain phase connection. After correlation the phases of all antennas are referenced to one antenna of the array, hence synchronizing the time of arrival of individual wave fronts. The phase solutions found in this step are then applied to the data of the target source. The last step cannot, however, account for differences in the atmosphere along the slightly different lines of sight to calibrator and target (Figure 4.5) resulting in residual phase errors. To keep such errors small it is essential for the calibrator source to be as close to the target source as possible.

Regardless of how close the calibrator source is, however, some residual delays caused by the differential atmosphere remain, influencing the accuracy of position measurements. The only way to take care of this effect is to have a strong compact source which is, ideally, also of extragalactic origin within the beam observing the target source. Once the calibration solutions from the phase referencing source have been applied, further refinement of the phase solution can be obtained in a process known as self-calibration. For that, a first model of the source is constructed by, e.g., imaging. The observed visibilities V_{ij}^{obs} of any pair of antennas (i, j) are then compared with the theoretical ones, V_{ij}^{mod}, for this model. The true visibilities V_{ij}^{true} are distorted by the complex gains $G_j = |G_j|e^{i\phi_j}$ of the individual telescopes such that

$$V_{ij}^{obs} = G_i G_j^* V_{ij}^{true} \,. \tag{4.14}$$

Inserting Eq. 4.5 yields

$$|V_{ij}^{obs}|e^{i\phi_{ij}^{obs}} = |G_i||G_j||V_{ij}|e^{i(\phi_i - \phi_j + \phi_{ij}^{true})} \,. \tag{4.15}$$

If the product of the observed visibilities as given above obtained from the three baselines of any three telescopes (i, j, k) of an interferometric array is considered, comparison of the phase terms in Eq. 4.15 yields the so-called closure phase $\phi_{ijk}^{closure}$

$$\phi_{ijk}^{closure} = \phi_{ij}^{obs} + \phi_{jk}^{obs} + \phi_{ki}^{obs} = \phi_{ij}^{true} + \phi_{jk}^{true} + \phi_{ki}^{true} \,. \tag{4.16}$$

In this expression, the closure phase is independent of the antenna based gains. Therefore, given the known setup of the array and the previously obtained model, the true visibilities can be predicted. Any offsets between the closure phase given by

[6] A list of suitable calibrator can, e.g., be found at `http://www.vlba.nrao.edu/astro/calib/`.

the observed visibilities and those as predicted by the model must then be related to the antenna based gains. The latter can then be adjusted until the observations match the model.

The above calibration steps are typically performed using software packages such as the *Common Astronomy Software Application* (CASA[7]) or the *Astronomical Image Processing System* (AIPS[8]). For global VLBI observations, as are discussed in this thesis, mostly only the latter package, AIPS, is being used because unlike CASA it contains routines to perform fringe fitting. In AIPS, all calibration solutions are stored in so-called tables that contain the computed modifications to amplitudes and phases. The solutions from individual calibration steps are typically stored in the SN-tables, all of which are eventually combined in a CL-table. The latter, along with the BP-table calibrating the bandpass response of the individual telescopes, is applied to the uncalibrated data before imaging and subsequent analysis.

4.3 Pulsar astrometry with VLBI

As already mentioned in section 2.3 radio interferometric observations, in particular with VLBI, are the only means to obtain estimates of the parallax π and proper motion $\mu = (\mu_\alpha, \mu_\delta)$ of radio pulsars independent of intrinsic pulsar parameters such as the pulse period and its derivative. At the same time, VLBI pulsar position measurements and, hence, measurements of μ and π, are complementary to measurements obtained from pulsar timing. As such, they are excellent means to link the VLBI reference frame (see below) to that of pulsar timing which is given by the Solar System ephemeris (cf. section 2.3).

The principle behind the measurement of both μ and π is a very simple one: the position of the source in right ascension α and declination δ is determined at multiple times t and the resulting changes are then modelled with five[9] parameters only

$$\begin{aligned} \alpha(t) &= \alpha_0 + \pi(t) + \mu_\alpha \cdot t \\ \delta(t) &= \delta_0 + \pi(t) + \mu_\delta \cdot t\,. \end{aligned} \tag{4.17}$$

[7] `http://casa.nrao.edu/`
[8] `http://www.aips.nrao.edu/index.shtml`
[9] Further parameters, like a curvature term due to the motion in a wide binary orbit or about a central mass, might also be requried (e.g. Deller et al., 2013).

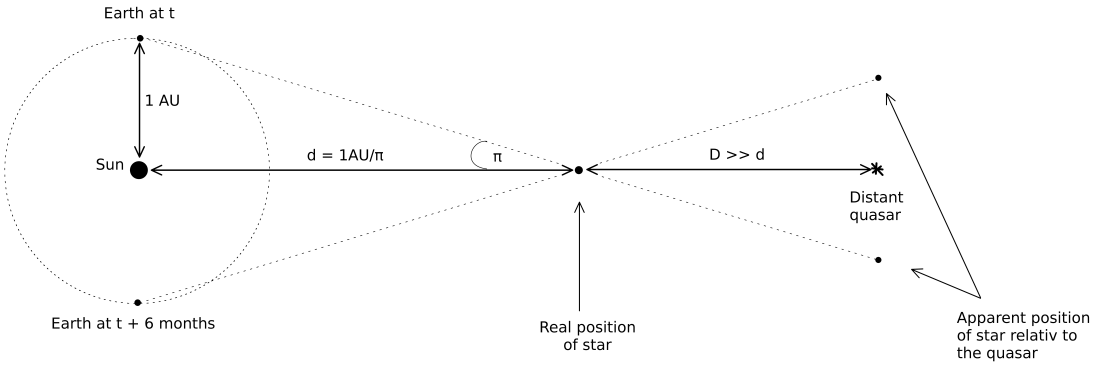

Fig. 4.6: Sketch of the geometric set-up of parallax measurements. The star under consideration appears to be moving relative to the fixed position of a distant background source, typically a quasar. In units of parsec the distance is given as $\frac{d}{[\mathrm{kpc}]} = \frac{[\mathrm{mas}]}{\pi}$.

Here, the vector (α_0, δ_0) is a reference position that is of little further interest. The time dependence of π is of sinusoidal nature due to the pure geometry of the system (Figure 4.6). The key to the determination of an accurate parallax and proper motion lies in the accuracy of the position measurements. Since π and μ are on the order of milliarcseconds (mas) and mas yr^{-1}, respectively, the positions need to be known with up to μas-accuracy.

In order to achieve such precision measurements, absolute positions of extragalactic calibrator sources need to be known with a small level of uncertainty since, eventually, absolute pulsar positions are measured relative to the reference frame spanned by these quasi stationary radio sources. This reference frame is referred to as the international celestial reference frame (ICRF) with its latest realization being ICRF2 (Ma et al., 2009). The average uncertainty of the 3414 compact radio sources comprising this catalogue is about 40 μas which is sufficient for standard pulsar observations. The dominating uncertainties in the position measurements are, therefore, those caused by the differential atmosphere towards calibrator and target as discussed in the previous section. For the most precise measurements, the inclusion of an in-beam calibrator as done in the observations discussed in chapters 5 and 6 is of vital importance.

Once the systematic uncertainties of the positions have been removed the only remaining errors are the formal errors. Assuming an elliptical Gaussian shape of the interferometer beam

$$B = (\theta_\alpha, \theta_\delta) = 1.22\lambda(\frac{1}{D^{max}_{E-W}}, \frac{1}{D^{max}_{N-S}}) \,, \tag{4.18}$$

where $(D^{max}_{E-W}, D^{max}_{N-S})$ are the longest baselines in East-West and North-South direction, respectively, the formal errors are given as

$$(\Delta\alpha, \Delta\delta) = \frac{1}{2 \cdot \mathrm{S/N}}(\theta_\alpha, \theta_\delta) \,. \tag{4.19}$$

Hence, for a given array observing at the central frequency ν_0 the uncertainties scale inversely with the signal-to-noise ratio S/N. One at first sight obvious option to boost the S/N for pulsars is to observe at low frequencies at which pulsars are much brighter due to their steep spectrum (section 2.1). This would, however, at the same time increase the thermal noise of the data and also decrease the overall resolution of the interferometer. E.g., the increase in the S/N when going from observations at L-band ($\lambda \approx 18\,\mathrm{cm}$) to observations at P-band ($\lambda \approx 92\,\mathrm{cm}$) would be a factor of four (assuming the canonical pulsar spectral index $\alpha = -1.8$, Maron et al. 2000) while the angular resolution would decrease by a factor of five. Therefore, pulsar VLBI observations are usually conducted at L- and C-band ($\lambda \approx 6\,\mathrm{cm}$) as an optimal compromise between angular resolution and S/N. One nescessity to increase the S/N is, thus, to keep the noise level at a minimum by either including large radio telescopes in the observations or by observing for long periods of time or both. A further option to increase the S/N is given by ability of modern software correlators[10] to perform pulsar gating/ binning during the correlation.

Since a typical pulsar is only observable for about 5% of its pulse period (e.g. Lorimer & Kramer, 2005), 95% of the data from a standard correlation contain only noise. This can be avoided by introducing a gating of the data separating 'On' and 'Off' times and, eventually, only correlate the 'On' data. The increase in S/N ratio scales as $1/\sqrt{r}$ where r is the ratio of pulse width ('On' time) to pulse period known as the pulsar duty cycle. For this correlation mode to operate properly the exact knowledge of the pulse arrival times is necessary. Therefore, simultaneous single dish pulsar observations towards the beginning and the end of the VLBI experiment are conducted, an ephemeris is derived and the resulting 'polycos' – a polynomial description of the pulse arrival times obtained with software such as TEMPO[11] – are supplied to the correlator. A further improvement of the S/N, especially for pulsars with a pulse profile significantly different from a Gaussian profile, is possible by pul-

[10] Such as DiFX (Deller et al., 2007) of SFXC (Keimpema 2014, in prep.)
[11] `http://tempo.sourceforge.net/`

sar binning. Instead of a simple binary gate, the 'On'-phase is split into several bins which are then weighted individually by the pulse strength in each bin. Compared to a binary gate, the S/N can be improved by up to 21% using this method for a complex pulse profile (Deller, 2009).

Once the data has been optimised, the results for π and μ from fitting Eq. 4.17 to the data yield the distance d (Figure 4.6) and the transverse velocity $V_\perp$ of the pulsar. The astronomical applications of such measurements are versatile: In combination with the dispersion measure (section 2.3) the distance alone yields the electron column density n_e along the line of sight to the pulsar. Combining the results for n_e for a large number of pulsars along many lines of sight at different d helps to constrain the electron density model of the Galaxy. This is important because the typically used model (NE2001, Cordes & Lazio, 2003) has been shown to be off by a factor of a few for individual pulsars (e.g. Brisken et al., 2003; Deller et al., 2009). This, in turn, yields a large degree of uncertainty for the distance of the bulk of the pulsar population for which the dispersion measure is the only indicator of the distance.

In conjunction with the distance, the angular proper motion is a measure for the transverse velocity of a pulsar. The transverse velocity distribution of pulsars has revealed that these compact object have large space velocities on the order of a few hundred $\mathrm{km\,s^{-1}}$ (up to $> 1000\,\mathrm{km\,s^{-1}}$, Chatterjee et al., 2005) regardless of fitting a two-component (Cordes & Chernoff, 1998; Arzoumanian et al., 2002) or one-component model (Hobbs et al., 2005) to the data. This velocity is much higher than that of ordinary stars ($v \sim 10\,\mathrm{km\,s^{-1}}$) including the pulsar progenitor O- and B-type stars. Hence, the space velocity gives an insight into pulsar formation scenarios since these must be able to provide some kind of a kick to accelerate the compact object during or shortly after formation (for a review on supernova kick mechanisms see Lai, 2004). Apart from adding to the statistical accuracy of the pulsar velocity distribution, the precise data from VLBI observations also allow to trace pulsars through the Galactic potential back to a possible birth location. Consequently, previous associations (e.g. Hoogerwerf et al., 2001) and possible binary companions (e.g. Vlemmings et al., 2004) can be inferred (see also chapter 7 of this thesis). At the same time, tracing pulsars back to their birth location allows conclusions about the kinematic age as opposed to the characteristic age (section 2.2) and, hence, constrains pulsar spin down models. Additionally, for pulsars and also for other type of compact objects located inside a GC the transverse velocity is an indicator for (i) the kinematics inside the GC and, hence, probes the gravitational

potential of the cluster; and (ii) a (non-) association of sources with the GC. An example of such an experiment using the pulsars in the GC M15 is discussed in chapter 6.

Finally, as discussed in section 2.3, the parameters contributing to the orbital period decay of a close binary system are covariant with the proper motion of a pulsar. Accordingly, VLBI proper motion measurements yield improvements in the estimates of relativistic parameters by helping to disentangle the individual timing model components.

4.4 Pulsar timing with VLBI

The principle observables of standard VLBI observations are the position and the flux density of a source. The latter is only accurate for compact, unresolved sources. In case the source of interest is strong enough and the observations are conducted with a large bandwidth it might be possible to also obtain spectral information by measuring the flux density in the individual subbands (IFs). Furthermore, provided a single observing run spans a sufficiently large time range, even short-term variability (∼a few hours) of a target (caused by, e.g., a binary, accretion peaks, scintillation) might be observable. However, the sensitivity and especially the time resolution ($\delta t \sim 1\,\mathrm{s}$) of typical VLBI data is by no means sufficient to, e.g., resolve individual pulses of a pulsar. Within the scope of this thesis, a new correlation algorithm was developed and tested in close collaboration with the Joint Institute for VLBI in Europe (JIVE). Instead of forming standard cross correlations of the raw voltages from the individual telescopes as described in section 4.1, this new correlation strategy coherently adds the signals of each telescope, thus mimicking a telescope with an effective area equal to the sum of that of all individual telescopes while keeping the full time resolution ($\delta t \sim 100\,\mu\mathrm{s}$). The advantage of this observing mode is that while delivering the full angular resolution of the interferometer and also a higher sensitivity than any individual telescope of the array, the output data has a temporal resolution comparable to that of typical pulsar timing observations. Therefore, observing pulsars with this *phased-array* mode yields both accurate astrometry and a TOA. Details about the implementation of this correlation mode and the first test results will be discussed in chapter 8.

References

Arzoumanian, Z., Chernoff, D. F., & Cordes, J. M. 2002, ApJ, 568, 289

Brisken, W. F., Thorsett, S. E., Golden, A., & Goss, W. M. 2003, ApJL, 593, L89
Chatterjee, S., Cordes, J. M., Vlemmings, W. H. T., et al. 2004, ApJ, 604, 339
Chatterjee, S., Vlemmings, W. H. T., Brisken, W. F., et al. 2005, ApJL, 630, L61
Cordes, J. M. & Chernoff, D. F. 1998, ApJ, 505, 315
Cordes, J. M. & Lazio, T. J. W. 2003, ArXiv Astrophysics e-prints
Deller, A. T. 2009, PhD thesis, PhD Thesis, 2009
Deller, A. T., Boyles, J., Lorimer, D. R., et al. 2013, ApJ, 770, 145
Deller, A. T., Tingay, S. J., Bailes, M., & Reynolds, J. E. 2009, ApJ, 701, 1243
Deller, A. T., Tingay, S. J., Bailes, M., & West, C. 2007, PASP, 119, 318
Fomalont, E. B. & Perley, R. A. 1999, in Astronomical Society of the Pacific Conference Series, Vol. 180, Synthesis Imaging in Radio Astronomy II, ed. G. B. Taylor, C. L. Carilli, & R. A. Perley, 79
Hobbs, G., Lorimer, D. R., Lyne, A. G., & Kramer, M. 2005, MNRAS, 360, 974
Högbom, J. A. 1974, A&AS, 15, 417
Hoogerwerf, R., de Bruijne, J. H. J., & de Zeeuw, P. T. 2001, A&A, 365, 49
Kardashev, N. S., Khartov, V. V., Abramov, V. V., et al. 2013, Astronomy Reports, 57, 153
Lai, D. 2004, in Cosmic explosions in three dimensions, ed. P. Höflich, P. Kumar, & J. C. Wheeler, 276
Lorimer, D. R. & Kramer, M. 2005, Cambridge University Press
Ma, C., Arias, E. F., Bianco, G., et al. 2009, IERS Technical Note, 35, 1
Maron, O., Kijak, J., Kramer, M., & Wielebinski, R. 2000, A&AS, 147, 195
Thompson, A. R. 1999, in Astronomical Society of the Pacific Conference Series, Vol. 180, Synthesis Imaging in Radio Astronomy II, ed. G. B. Taylor, C. L. Carilli, & R. A. Perley, 11
Verbiest, J. P. W., Bailes, M., van Straten, W., et al. 2008, ApJ, 679, 675
Vlemmings, W. H. T., Cordes, J. M., & Chatterjee, S. 2004, ApJ, 610, 402

5 No Evidence for an intermediate mass black hole in M15

Franz Kirsten and Wouter Vlemmings, 2012, A&A, 542, A44

Abstract Intermediate mass black holes (IMBHs) with expected masses $M_\bullet \approx 10^4$ $M_\odot$ are thought to bridge the gap between stellar mass black holes ($M_\bullet \approx 3 - 100$ $M_\odot$) and supermassive black holes found at the centre of galaxies ($M_\bullet > 10^6$ $M_\odot$). Until today, no IMBH has been confirmed observationally. The most promising objects to host an IMBH as their central mass are globular clusters. Here, we present high sensitivity multi-epoch 1.6 GHz very long baseline interferometry observations of the globular cluster M15 that has been suggested to host an IMBH. Assuming the IMBH to be accreting matter from its surrounding we expect to detect it as a point source moving with the global motion of the cluster. However, we do not detect any such object within a radius of 6000 AU of the cluster centre in any of the five observations spread over more than one year. This rules out any variability of the putative IMBH on the time scale of one to two months. To get the most stringent upper limit for the flux density of the putative IMBH we concatenate the data of all five epochs. In this data we measure a 3σ upper flux limit of 10 μJy for a central source. We employ the fundamental plane of black hole activity to estimate the mass of the central IMBH candidate. Based on previous X-ray observations of M15 our measurements indicate a 3σ upper mass limit of ≈ 500 $M_\odot$.

5.1 Introduction

Super-massive black holes (SMBHs) with masses $M_\bullet \approx 10^{6-9}$ solar masses ($M_\odot$) are known to exist at the centre of galaxies (Kormendy & Richstone, 1995). At the same time, observations of high-mass X-ray binaries led to the conclusion that stellar-mass black holes with $M_\bullet \approx 100$ $M_\odot$ must form as well (McClintock & Remillard, 2006; Belczynski et al., 2010; Özel et al., 2010). The existence of black holes (BHs) bridging the gap between these two extremes in mass, the so-called intermediate mass black

holes (IMBHs, $M_\bullet \approx 10^4\ M_\odot$), is still under debate.

One possible candidate for IMBHs are ultraluminous X-ray sources (ULX, Colbert & Mushotzky 1999) appearing to accrete matter at super-eddington rates. The interpretation of ULX–properties as being characteristic for IMBHs, however, is still in discussion (e.g. Berghea et al. 2008, Zampieri & Roberts 2009). Nevertheless, the recent discovery of the hyper-luminous X-ray source ESO 243-49 HLX-1 by Farrell et al. (2009) adds evidence that ULXs might host IMBHs.

Based on the black hole mass–stellar velocity dispersion relation ($M_\bullet - \sigma$) established for galaxies (Ferrarese & Merritt, 2000; Gebhardt et al., 2000), an object like an IMBH can be expected to reside at the core of globular clusters (GCs). Even though recent work by Vesperini et al. (2010) shows that an IMBH can be formed in a GC environment, no conclusive observational evidence for the existence of IMBHs has been found to date.

Apart from, e.g, the globular clusters ω Cen (van der Marel & Anderson, 2010), G1 in M31 (Gebhardt et al., 2002; Ulvestad et al., 2007), and 47 Tuc (Lu & Kong, 2011), M15 has been one of the most promising GC–candidates to host an IMBH for a long time. Stellar surface density profiles of M15 reveal a steady increase towards the center of the cluster indicating a state of advanced core-collapse (Djorgovski & King, 1986). To explain the central brightness peak Newell et al. (1976) suggested an 800 $M_\odot$black hole to reside at the core of the cluster. The increase of the stellar velocity dispersion towards the centre of M15 as measured by, e.g, Gerssen et al. (2003), supports the notion of a high central mass concentration in the cluster. In fact, dynamical models based on line-of-sight velocities and proper motions infer a mass of 3400 $M_\odot$ within the central 1 arcsecond (= 0.05 pc at the distance of 10.3 ± 0.4 kpc, van den Bosch et al. 2006). The nature of this mass concentration is unknown. Gerssen et al. (2003) invoke the existence of an IMBH with a mass of $M_\bullet = 1700^{+2700}_{-1700}\ M_\odot$ to explain their observations. Similarly to Illingworth & King (1977), Baumgardt et al. (2003) and McNamara et al. (2003) challenge this interpretation, based on N-body simulations excluding an IMBH. Instead, these authors claim that the observational data can be explained equally well by assuming a collection of neutron stars to exist at the core of M15. The latest simulations of that kind require a total of 1600 neutron stars to fit the velocity-dispersion profile mentioned above (Murphy et al., 2011).

Complementary to the indirect (non-)evidence using kinematic studies based on optical observations, X-ray and radio observations aim at directly detecting such an object. The fundamental plane of black hole activity (FP) as determined for active galactic nuclei (AGN) (Merloni et al., 2003; Falcke et al., 2004), relates black-

hole mass, X-ray and radio luminosity. Now, assuming the same physical processes powering AGN–emission to also be characteristic for IMBHs, Maccarone (2004) predict a black hole mass of 400 $M_\odot$ for the IMBH in M15. Their result is based on an estimate of the cluster's total mass, $M_{\rm GC}$, from its absolute V-magnitude, $M_{\rm V}$, and on a model by Miller & Hamilton 2002 stating that $M_\bullet \approx 10^{-3} M_{\rm GC}$. Bash et al. (2008), on the other hand, perform a survey of M15 at 8.6 GHz using the Very Large Array that reaches a noise level of 8.5 μJy/ Beam. Using the FP they predict a flux density of $10^3 - 10^5$ μJy for a putative IMBH with a spectral index $\alpha = -0.7$. They detect no central source at a 3σ upper flux limit of 25 μJy. Similary, Cseh et al. (2010) tried to detect an IMBH at the center of the globular cluster NGC 6388. The 3σ noise level (81 μJy) of their observations with the Australia Telescope Compact Array allowed the authors to constrain the mass of the possible IMBH to be lower than ≈ 1500 $M_\odot$.

In this paper we discuss multi-epoch observations of M15 almost three times as sensitive as those of Bash et al. (2008). The high angular resolution of our data allows us to disentangle any possible background sources from objects belonging to the cluster. Furthermore, the long time line spanning 15 months allows us to, in principle, detect the proper motion of a possible central radio source moving with the global motion of the cluster expected to be on the order of -1.0 ± 0.4 and -3.6 ± 0.8 mas/yr in right ascension (RA) and declination (Dec), respectively (Jacoby et al., 2006).

5.2 Observations

We observed M15 five times in a global VLBI campaign that was spread over a time period of more than one year. The observations included in this analysis were conducted on 11 November 2009, 7 March 2010, 5 June 2010, 2 November 2010, and 27 February 2011. The array we employed consisted of eight European VLBI Network (EVN) antennas (Jodrell Bank, Onsala, Westerbork, Effelsberg, Noto, Medicina, Toruń, Arecibo) and the Greenbank Telescope (GBT). We observed at a central frequency of 1.6 GHz and the data was recorded at 1024 Mbps. Accounting for the different receiver systems at the individual telescopes our total bandwidth amounts to 230 MHz on average. The correlation was done at the EVN-MkIV correlator (Schilizzi et al., 2001) at the *Joint Institute for VLBI in Europe* (JIVE).

The longest baselines in east-west (north-south) direction extending over 7500 (2000) km allow for a resolution of 2.2×6.3 mas. The largest dishes of the array (Arecibo, Effelsberg, and the GBT) ensure a maximum sensitivity of approximately 4 μJy/ Beam.

The observing schedule lasted six hours in total, 3.6 hr of which were spent on the target cluster M15. The quasar J2139+1423 (located $\approx 3.17^\circ$ to the north-east of the pointing center) served as phase calibrator and the blazar 3C454.3 was used for bandpass calibration. Arecibo-data is available for 75 (50) min in epochs 1 and 5 (epoch 3). Unfortunately, epochs 2 and 4 lack any Arecibo data which is why the sensitivity and astrometric precision of these two datasets is lower by about a factor of two.

Aiming to detect compact radio sources close to the core of M15 we map out the entire central region within $2'$ in only one pointing. For this project, however, only the very central region (the central $16''$) correlated at RA = $21^{\rm h}29^{\rm s}58\overset{\rm s}{.}3120$, Dec = $12^\circ10'02\overset{''}{.}679$ (J2000 equinox) is of interest. The entire dataset will be described in a forthcoming paper.

5.3 Data reduction

After correlation, all data is reduced, calibrated and imaged using the NRAO *Astronomical Image Processing System* (AIPS[1]). A priory calibration tables including system temperature and gain curve corrections as well as a flag table containing information about band edges and off-source times are provided by the EVN pipeline[2]. We apply these to the dataset as given. Parallactic angle corrections are determined with the AIPS task CLCOR and first ionospheric corrections are computed running TECOR with the total electron content (TEC) maps published by the *Center for Orbit Determination in Europe*[3]. Even though these maps are quite crude in angular resolution (about $5^\circ \times 2.5^\circ$) they have shown to be of use reducing the scatter in phase delay by a factor of 2-5 (Walker & Chatterjee, 1999). Next, we identify and flag radio frequency interference (RFI) for all antennas and sub bands.

The bandpass calibration is done running BPASS on the data for 3C454.3 and yields phase and amplitude gain factors for all 8×128 (512, epoch 1) channels for all antennas. We align phases in between IFs by performing a manual fringe correction running FRING on 3C454.3 on a sub-interval of about 30 s of observation.

At this point, we combine all correction tables obtained so far and apply it to the data of the phase calibrator. We fringe fit this dataset including data over the entire time range. We solve for phase delays and phase rates simultaneously using solution intervals of 1.5 min.

The fringe solutions in conjunction with all calibration solutions found earlier are

[1] `http://www.aips.nrao.edu/`
[2] `http://www.evlbi.org/pipeline/user_expts.html`
[3] `ftp://ftp.unibe.ch/aiub/CODE/`

then applied to the M15 data. In order to eliminate any residual phase delays and amplitude errors caused by the atmosphere and the ionosphere we take advantage of the strong unclassified source S1 (Johnston et al., 1991) located about 94″ to the west of the cluster centre and use it for in-beam calibration. To speed up the self-calibration process we average the visibilities both in the time- and frequency domain to 2 s integration time and 64 channels per IF.

Finally, we image the self-calibrated data running IMAGR employing natural weighting to ensure maximal sensitivity. In order to account for possible inaccuracies in the assumed cluster centre we produce an image that has an angular size of roughly $16'' \times 16''$ ($= 0.8 \times 0.8$ pc).

5.4 Analysis and results

In all five epochs we first produce a noise map of the image by smoothing it with a kernel that has a size of 1024×1024 pixels. Based on this rms map, the AIPS source detection algorithm SAD then searches for objects down to a signal-to-noise ratio of 3. The coordinates of the possible sources detected in this fashion in all five observation epochs are then cross-correlated. Cross-correlation is performed allowing for a maximal positional shift of 15 mas in between epochs. This corresponds to roughly four times the maximal beam width in right ascension. No match can be found relating all five data sets.

Finally, we also inspect the images manually. Figure 5.1 displays contour plots of the dirty images of the central region of M15 for all five epochs. All tiles are centred on the cluster core as published by Goldsbury et al. (2010) at coordinates RA = $21^{\mathrm{h}}29^{\mathrm{s}}58\overset{\mathrm{s}}{.}330$, Dec = $12^{\circ}10'01\overset{''}{.}200$ (accurate to within 0.2″). We do not detect a significant signal in any of the epochs. Accounting for the different sensitivity limits varying between 4.3 μJy/ Beam in epoch 3 and 11.5 μJy/ Beam in epoch 4, we can put upper 3σ limits between 13 and 35 μJy/ Beam on the flux density of a possible central object. Figure 5.1 also displays a dirty image of the data concatenated over all five epochs. The rms of this deconvolved image is 3.3 μJy/ Beam which translates to a 3σ upper flux limit of 10 μJy/ Beam.

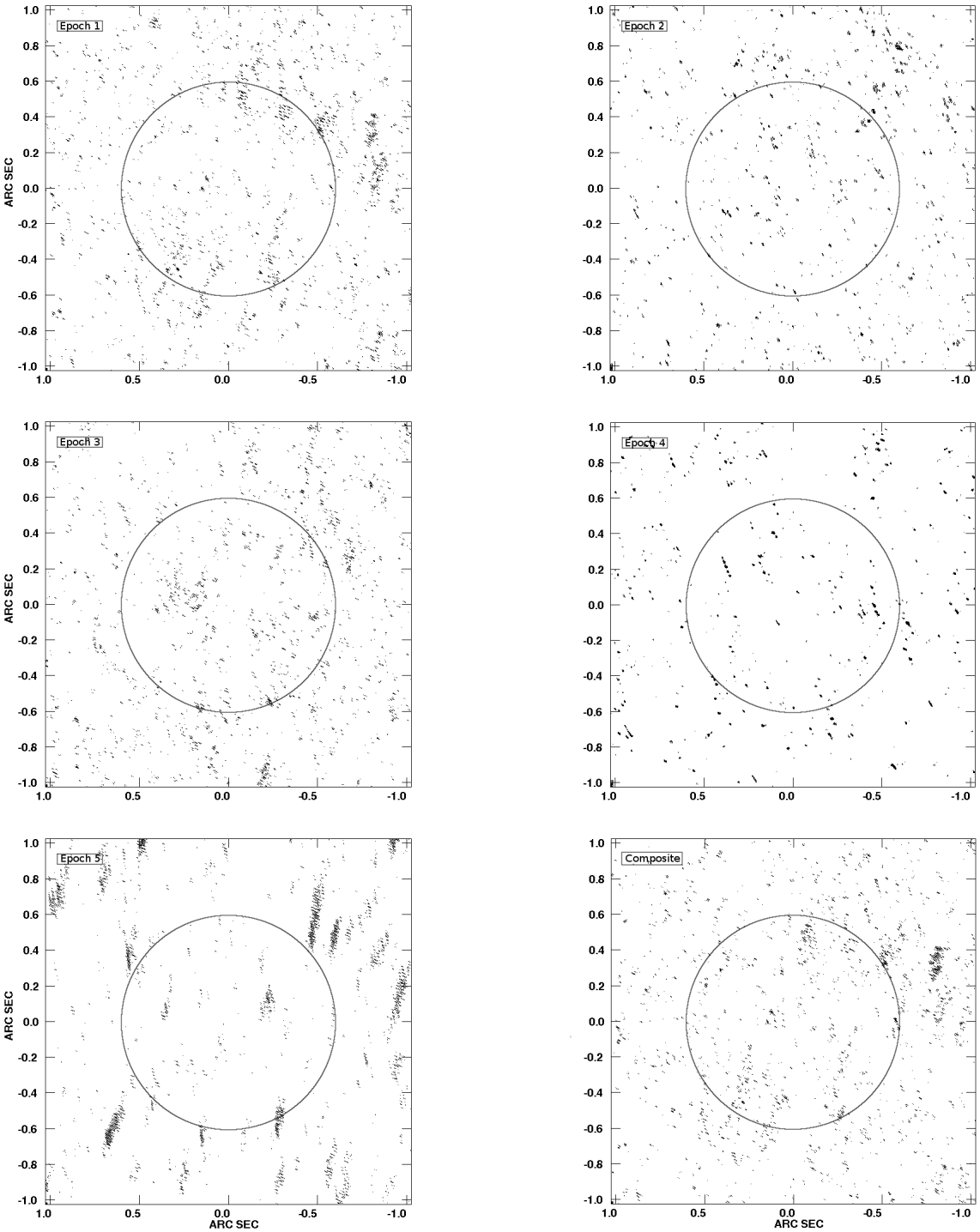

Fig. 5.1: Contour plots of all five individual observations and the composite image combining the data of all epochs. The tiles are centred on the assumed core of M15 at coordinates RA = $21^{\mathrm{h}}29^{\mathrm{s}}58\overset{\mathrm{s}}{.}330$, Dec = $12°10'01\overset{''}{.}200$. The circle indicates the 3σ error of the position of the core as determined by Goldsbury et al. (2010). Adopting a distance of 10.3 kpc to M15, each tile has a physical dimension of about $(20000\ \mathrm{AU})^2$. Contours are $(-5, -3, 3, 5)$ times the rms in each individual epoch (4.7, 8.9, 4.3, 11.5, 5.8 μJy). The noise level of the composite image is 3.3 μJy

5.5 Discussion

5.5.1 Radio flux limits and variability

The five individual epochs have rather different sensitivity limits that correspond to a 3σ upper flux density limit of 14.1, 26.7, 12.9, 34.5, 17.4 μJy/ Beam for epochs 1 to 5. We did not detect a central source in any of the observations that were conducted at regular intervals of about three months spanning a time range of 15 months. Provided the IMBH-candiate is of transient nature that is in its 'on'–state for longer than one or two months, the probability to have missed it in all five observations is negligible. Therefore, we rule out any variability of the central object on these time scales. Accordingly, we can assume a steady state emission model in which case the noise level of the concatenated data yields the most stringent 3σ upper flux limit of ≈ 10 μJy. This flux limit is a factor of 2.5 lower than that from Bash et al. (2008) and we will adopt it throughout the following analysis.

5.5.2 Mass limits from X-ray observations

Similarly to the first versions of the FP from Merloni et al. (2003) and Falcke et al. (2004), the FP derived by Körding et al. (2006) uses a sample including both X-ray binaries (XRBs) and AGN. Thus, both versions span several orders of magnitude in BH mass and should also be applicable for the intermediate mass range of IMBHs. The relation found by Körding et al. (2006) for XRBs and low-luminosity radiatively inefficient AGN has the lowest intrinsic scatter $\sigma_{\rm int} = 0.12$ dex (≈30 percent) and we will use it in the following. In terms of black hole mass $M_\bullet$, radio luminosity L_R, and X-ray luminosity L_X their FP-relation reads

$$\log M_\bullet = 1.55 \log L_R - 0.98 \log L_X - 9.95 \ .$$

M15 is known to host two strong X-ray sources, AC211 (Giacconi et al., 1974; Clark et al., 1975) and M15 X2 (White & Angelini, 2001), close to the core of the cluster. Both have been classified as low mass XRBs. The strong X-ray emission of these two objects makes it difficult to detect the expectedly faint emission of a central IMBH. Nevertheless, Ho et al. (2003) put an upper limit of $L_X = 5.6 \times 10^{32}$ erg/s on the X-ray luminosity of the putative IMBH. Hannikainen et al. (2005) manage to detect a faint source ($L_X = 3.3 \times 10^{32}$ erg/s) close to core of M15 which they attribute to a dwarf nova. In their paper, Hannikainen et al. (2005) report a flux detection limit of 2×10^{-15} erg/s/cm (0.5-2 keV) which translates to an X-ray luminosity of 2.54×10^{31} erg/s at the distance of M15. Converting our measured radio flux to a 5

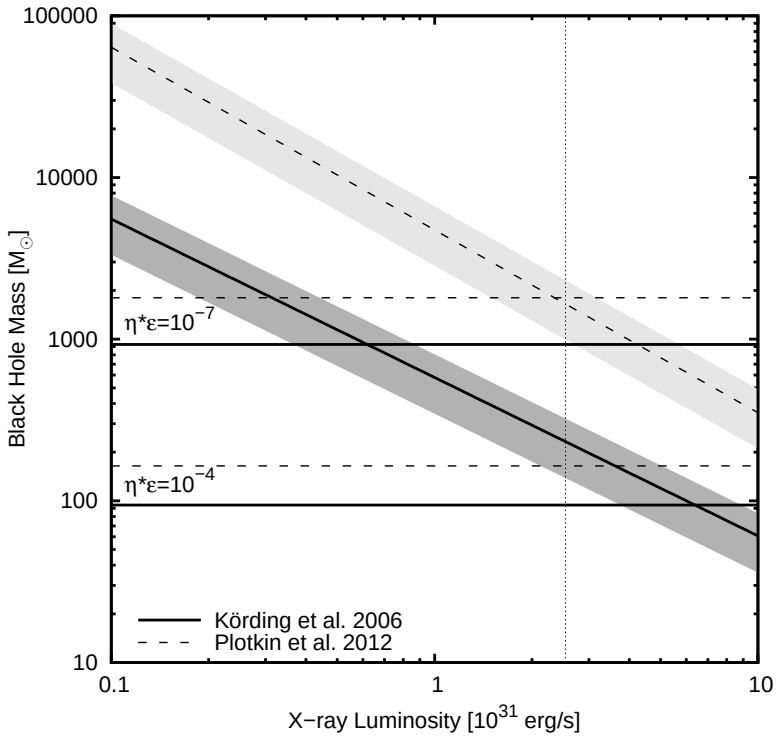

Fig. 5.2: Black hole mass as a function of X-ray luminosity for our measured radio luminosity ($L_R = 6.34 \times 10^{27}$ erg/s) as predicted by the FP from Körding et al. (2006) (solid lines) and Plotkin et al. (2012) (dashed lines). The gray shaded areas indicate the 1σ uncertainties of the relations. The horizontal lines mark the predicted masses for different assumptions on the radiative efficiency η and the accretion efficiency ϵ. The vertical dotted line marks the upper limit for the X-ray luminosity from Hannikainen et al. (2005).

GHz radio luminosity $L_R \leq 6.34 \times 10^{27}$ erg/s (assuming a flat radio spectrum) and inserting it together with the upper limit for the X-ray luminosity from Hannikainen et al. (2005) the FP yields a mass limit of $232 \pm 93\ M_\odot$. This translates to a very conservative 3σ upper mass limit of 511 $M_\odot$ for the putative IMBH. Our observations thus decreased the upper mass limit by a factor of four compared to that indicated by earlier observations by Bash et al. (2008).

5.5.3 Mass limits from accretion models

The lack of a central X-ray source in M15 is expected because the accretion process is most likely radiatively inefficient (Ho et al., 2003). To constrain the mass of the IMBH–candidate we estimate the X-ray luminosity based on the (unknown) accretion rate $\dot{M}$:

$$L_X = \eta\epsilon\, c^2 \dot{M} \quad ,$$

where η and ϵ are the radiation efficiency and the accretion efficiency, respectively. The accretion process of radiatively inefficient black hole binaries (e.g. Esin et al. 1997) as well as those of quiescent SMBHs (e.g. Yuan et al. 2003) is well described by advection-dominated accretion flow models (ADAF, Narayan & Yi 1994). Such BHs undergo quasi-spherical accretion and, thus, following Maccarone (2004) we further assume that mass accretion of the putative IMBH in M15 can be described by the Bondi-Hoyle-Lyttleton (BHL) formalism (Hoyle & Lyttleton, 1941; Bondi & Hoyle, 1944; Ho et al., 2003)

$$\dot{M}_{\rm BHL} = 3.2 \times 10^{17} \left(\frac{M_\bullet}{2000\ {\rm M}_\odot}\right)^2 \left(\frac{n}{0.2\ {\rm cm}^{-3}}\right) \left(\frac{T}{10^4 {\rm K}}\right)^{-1.5} {\rm g\ s}^{-1}\ .$$

Here, n and T are the gas density and temperature in the GC, respectively. We adopt $n = 0.2$ cm^{-3} from Freire et al. (2001) and use a typical GC gas temperature of $T = 10^4$ K. Inserting the above equations into the FP, and solving for $M_\bullet$ yields

$$2.96\ {\rm log}M_\bullet = 1.55\ {\rm log}L_R - 0.98\ {\rm log}(\eta * \epsilon) - 41.17\ .$$

Mass estimates from this relation depend crucially on the choice of η and ϵ. Observations of the IMBH–candiate in G1 in M31 suggest that the radiative efficiency $\eta < 0.01$ for this source (Ulvestad et al., 2007). This is consistent with the aforementioned ADAF models that are only valid for $\eta \ll 0.1$ (Narayan & McClintock, 2008). In order to cover as large a parameter space as possible we choose $\eta = 0.1$ as conservative upper limit for the radiative efficiency. As lower limit we take the estimate of Ho et al. (2003) who state that η can be as low as 10^{-4} for the IMBH candidate in M15. It is not clear at all at what fraction ϵ of the Bondi rate the central source is accreting. Typical values are in the range $\epsilon = [10^{-3}, 0.1]$ (Maccarone, 2004; Ulvestad et al., 2007; Cseh et al., 2010) which we adopt for our analysis. Consequently, we explore a parameter space covering $\eta * \epsilon = [0.01, 10^{-7}]$. Based on the upper X-ray luminosity as measured by Hannikainen et al. (2005) we can exclude values of $\eta * \epsilon \geq 10^{-3}$ because they would yield stronger X-ray emission than what is observed. The mass limit for a value of $\eta * \epsilon = 10^{-4}$ is indicated in Fig. 5.2 and would yield a black hole mass $M_\bullet = 94 \pm 37\ M_\odot$. For $\eta * \epsilon = 10^{-5}$ we find $M_\bullet = 202 \pm 80\ M_\odot$ which would indicate a source that is accreting at ten percent of the Bondi-rate with a radiative efficiency[4] $\eta = 10^{-4}$. The combination of both, very inefficient radiation ($\eta = 10^{-4}$) and inefficient accretion ($\epsilon = 10^{-3}$) is also indicated in Fig. 5.2 with the mass estimate of $M_\bullet = 927 \pm 371\ M_\odot$.

[4]Obviously, other combinations of (η, ϵ) would also be suitable but we give this one as a limiting case that has been discussed by other authors (e.g. Ho et al. 2003, Cseh et al. 2010).

5.5.4 Mass estimates from other FP–relations

Mass estimates computed here with the FP–relation from Körding et al. (2006) agree well within the errors with those estimates computed from the relations found by, e.g., Merloni et al. (2003) and Gültekin et al. (2009). We note, however, a significant offset towards higher masses when using the latest version of the FP published by Plotkin et al. (2012). Their relation reads

$$\log M_\bullet = 1.64 \log L_R - 1.13 \log L_X - 6.89 \ .$$

In Fig. 5.2 the predicted BH mass from this relation for our measured radio flux density is indicated by the dashed lines. With this relation the limit for the X-ray luminosity results in a BH mass $M_\bullet = 1654 \pm 661\ M_\odot$. However, this mass limit can only be explained by the least efficient accretion limit of $\eta * \epsilon = 10^{-7}$. All higher values of $\eta * \epsilon$ would yield an X-ray luminosity beyond the one observed and can be excluded within this FP–relation.

5.6 Conclusions

Using our multi-epoch high sensitivity observations of M15 we were able to put an upper limit of 10 μJy on the 1.6 GHz radio flux density of a central source in this globular cluster. Assuming that the central mass concentration is a black hole we employed the FP as derived by Körding et al. (2006) to put constraints on the mass of the source. The lack of a detection of an object in the X-ray observations coinciding with the assumed cluster center allowed us to use an upper limit for the X-ray luminosity of the putative IMBH which yields a black hole mass $M_\bullet = 232 \pm 93$ $M_\odot$. Such a mass estimate is in agreement with a source accreting matter from its surrounding at up to ten percent of the Bondi-rate with a radiative efficiency as low as 10^{-4} which is consistent with results for the IMBH–candidate in G1 in M31 (Ulvestad et al., 2007). Even the 3σ upper limit of $\approx 500\ M_\odot$, however, is still a factor of seven lower than that required to explain the dynamics of the cluster (van den Bosch et al., 2006). If we employ the FP from Plotkin et al. (2012) the 3σ upper mass limit is increased to $\approx 3600\ M_\odot$ which would agree with the required dynamical mass. However, such a mass can only be explained if the central object is accreting at 0.1 percent of the Bondi rate and if only 0.01 percent of radiation is escaping from the accretion region. Furthermore, this mass estimate disagrees by a factor of seven with results obtained from most other FP–relations and we adopt the mass limit of $M_\bullet = 232 \pm 93\ M_\odot$.

Therefore, we conclude that M15 most likely does not contain an IMBH but that its central region probably hosts a collection of dark remants such as neutron stars as proposed by, e.g., Baumgardt et al. (2003); McNamara et al. (2003), and Murphy et al. (2011) instead. The reason for not detecting these pulsars is most probably their expected low flux density of ≈ 2 μJy (Sun et al., 2002).
During the final stages of the refereeing process of this paper, Strader et al. (2012) published a mass estimate for the IMBH in M15 that is in good agreement with the estimate derived here.

References

Bash, F. N., Gebhardt, K., Goss, W. M., & Vanden Bout, P. A. 2008, AJ, 135, 182
Baumgardt, H., Hut, P., Makino, J., McMillan, S., & Portegies Zwart, S. 2003, ApJL, 582, L21
Belczynski, K., Bulik, T., Fryer, C. L., et al. 2010, ApJ, 714, 1217
Berghea, C. T., Weaver, K. A., Colbert, E. J. M., & Roberts, T. P. 2008, ApJ, 687, 471
Bondi, H. & Hoyle, F. 1944, MNRAS, 104, 273
Clark, G. W., Markert, T. H., & Li, F. K. 1975, ApJL, 199, L93
Colbert, E. J. M. & Mushotzky, R. F. 1999, ApJ, 519, 89
Cseh, D., Kaaret, P., Corbel, S., et al. 2010, MNRAS, 406, 1049
Djorgovski, S. & King, I. R. 1986, ApJL, 305, L61
Esin, A. A., McClintock, J. E., & Narayan, R. 1997, ApJ, 489, 865
Falcke, H., Körding, E., & Markoff, S. 2004, A&A, 414, 895
Farrell, S. A., Webb, N. A., Barret, D., Godet, O., & Rodrigues, J. M. 2009, Nature, 460, 73
Ferrarese, L. & Merritt, D. 2000, ApJL, 539, L9
Freire, P. C., Kramer, M., Lyne, A. G., et al. 2001, ApJL, 557, L105
Gebhardt, K., Bender, R., Bower, G., et al. 2000, ApJL, 539, L13
Gebhardt, K., Rich, R. M., & Ho, L. C. 2002, ApJL, 578, L41
Gerssen, J., van der Marel, R. P., Gebhardt, K., et al. 2003, AJ, 125, 376
Giacconi, R., Murray, S., Gursky, H., et al. 1974, ApJS, 27, 37
Goldsbury, R., Richer, H. B., Anderson, J., et al. 2010, AJ, 140, 1830
Gültekin, K., Cackett, E. M., Miller, J. M., et al. 2009, ApJ, 706, 404
Hannikainen, D. C., Charles, P. A., van Zyl, L., et al. 2005, MNRAS, 357, 325
Ho, L. C., Terashima, Y., & Okajima, T. 2003, ApJL, 587, L35
Hoyle, F. & Lyttleton, R. A. 1941, MNRAS, 101, 227
Illingworth, G. & King, I. R. 1977, ApJL, 218, L109
Jacoby, B. A., Cameron, P. B., Jenet, F. A., et al. 2006, ApJL, 644, L113
Johnston, H. M., Kulkarni, S. R., & Goss, W. M. 1991, ApJL, 382, L89
Körding, E., Falcke, H., & Corbel, S. 2006, A&A, 456, 439
Kormendy, J. & Richstone, D. 1995, ARAA, 33, 581
Lu, T.-N. & Kong, A. K. H. 2011, ApJL, 729, L25
Maccarone, T. J. 2004, MNRAS, 351, 1049
McClintock, J. E. & Remillard, R. A. 2006, Black hole binaries, Compact stellar X-ray sources, ed. Lewin, W. H. G. & van der Klis, M. (Cambridge University Press), 157–213
McNamara, B. J., Harrison, T. E., & Anderson, J. 2003, ApJ, 595, 187
Merloni, A., Heinz, S., & di Matteo, T. 2003, MNRAS, 345, 1057

Miller, M. C. & Hamilton, D. P. 2002, MNRAS, 330, 232
Murphy, B. W., Cohn, H. N., & Lugger, P. M. 2011, ApJ, 732, 67
Narayan, R. & McClintock, J. E. 2008, New A Rev., 51, 733
Narayan, R. & Yi, I. 1994, ApJL, 428, L13
Newell, B., Da Costa, G. S., & Norris, J. 1976, ApJL, 208, L55
Özel, F., Psaltis, D., Narayan, R., & McClintock, J. E. 2010, ApJ, 725, 1918
Plotkin, R. M., Markoff, S., Kelly, B. C., Körding, E., & Anderson, S. F. 2012, MNRAS, 419, 267
Schilizzi, R. T., Aldrich, W., Anderson, B., et al. 2001, Experimental Astronomy, 12, 49
Strader, J., Chomiuk, L., Maccarone, T., et al. 2012, ArXiv e-prints (arXiv:1203.6352)
Sun, X.-H., Han, J.-L., & Qiao, G.-J. 2002, ChJAA, 2, 133
Ulvestad, J. S., Greene, J. E., & Ho, L. C. 2007, ApJL, 661, L151
van den Bosch, R., de Zeeuw, T., Gebhardt, K., Noyola, E., & van de Ven, G. 2006, ApJ, 641, 852
van der Marel, R. P. & Anderson, J. 2010, ApJ, 710, 1063
Vesperini, E., McMillan, S. L. W., D'Ercole, A., & D'Antona, F. 2010, ApJL, 713, L41
Walker, R. C. & Chatterjee, S. 1999, VLBA Scientific Memo 23 (Socorro, NM: NRAO)
White, N. E. & Angelini, L. 2001, ApJL, 561, L101
Yuan, F., Quataert, E., & Narayan, R. 2003, ApJ, 598, 301
Zampieri, L. & Roberts, T. P. 2009, MNRAS, 400, 677

6 Precision astrometry of pulsars and other compact radio sources in the globular cluster M15

Franz Kirsten, Wouter Vlemmings, Paulo Freire, Michael Kramer, Helge Rottmann and Robert M. Campbell, 2014, A&A, 565, 43

Abstract The globular cluster (GC) M15 (NGC 7078) is host to at least eight pulsars and two low mass X-ray binaries (LMXBs) one of which is also visible in the radio regime. Here we present the results of a multi-epoch global very long baseline interferometry (VLBI) campaign aiming at i) measuring the proper motion of the known compact radio sources, ii) finding and classifying thus far undetected compact radio sources in the GC, and iii) detecting a signature of the putative intermediate mass black hole (IMBH) proposed to reside at the core of M15. We measure the sky motion in right ascension (μ_α) and declination (μ_δ) of the pulsars M15A and M15C and of the LMXB AC211 to be $(\mu_\alpha,\, \mu_\delta)_{\rm M15A} = (-0.54 \pm 0.14,\, -4.33 \pm 0.25)\,{\rm mas\,yr^{-1}}$, $(\mu_\alpha,\, \mu_\delta)_{\rm M15C} = (-0.75 \pm 0.09,\, -3.52 \pm 0.13)\,{\rm mas\,yr^{-1}}$, and $(\mu_\alpha,\, \mu_\delta)_{\rm AC211} = (-0.46 \pm 0.08,\, -4.31 \pm 0.20)\,{\rm mas\,yr^{-1}}$, respectively. Based on these measurements we estimate the global proper motion of M15 to be $(\mu_\alpha,\, \mu_\delta) = (-0.58 \pm 0.18,\, -4.05 \pm 0.34)\,{\rm mas\,yr^{-1}}$. We detect two previously known but unclassified compact sources within our field of view. Our observations indicate that one them is of extragalactic origin while the other one is a foreground source, quite likely an LMXB. The double neutron star system M15C became fainter during the observations, disappeared for one year and is now observable again—an effect possibly caused by geodetic precession. The LMXB AC211 shows a double lobed structure in one of the observations indicative of an outburst during this campaign. With the inclusion of the last two of a total of seven observations we confirm the upper mass limit for a putative IMBH to be $M_\bullet < 500\ M_\odot$.

6.1 Introduction

Pulsars, typically searched for and detected with single dish radio telescopes, are rapidly rotating, highly magnetized neutron stars (NSs). Their spin axis and magnetic field axis – along which relativistic charged particles are accelerated emitting cyclotron radiation – are misaligned giving rise to the pulsar phenomenon. Being very stable rotators, pulsars are used as accurate clocks to measure their intrinsic parameters such as rotation period P, spin down rate $\dot{P}$, and position. The fastest pulsars, the so-called millisecond pulsars (MSPs, $P < 30\,\mathrm{ms}$), are the most stable rotators allowing for very accurate tests of theories of gravity (e.g. Antoniadis et al., 2013; Freire et al., 2012). Roughly one half of all MSPs has been found in globular clusters[1] (GCs) where the frequency of stellar encounters is high, favoring the evolution of normal pulsars to MSPs through angular momentum and mass transfer in a binary system (e.g. Bhattacharya & van den Heuvel, 1991). In total, about 6% of the 2302 currently known pulsars (as listed on the ATNF webpage[2], Manchester et al., 2005) reside in GCs with Terzan 5 and 47 Tuc leading the field with 34 and 23 confirmed pulsars, respectively, all but one being MSPs. Despite their rotational stability, disentangling all parameters of GC pulsars through pulsar timing is sometimes difficult due to the presence of the gravitational field of the GC. In those cases, model independent measurements of intrinsic pulsar parameters such as parallax, π, and proper motion, μ, can improve the overall timing solution. The ideal way to measure π and μ purely based on geometry is through radio interferometric observations.

Here we report about multi-epoch global very long baseline interferometry (VLBI) observations of the core region (~ 4 arcmin) of the GC M15 (NGC 7078). This GC is one of the oldest (13.2 Gyr, McNamara et al. 2004) and most metal poor ([Fe/H]$= -2.40$, Sneden et al. 1997) GCs known to reside in the Galaxy. It is host to eight known pulsars (four of them being MSPs), one of which is in a binary system with another neutron star (PSR B2127+11C, Anderson et al. 1990, Anderson 1993). Four of the other seven pulsars are located in close proximity to the cluster core (within $< 4.5\,\mathrm{arcsec} = 0.2\,\mathrm{pc}$ at the distance $d = 10.3 \pm 0.4\,\mathrm{kpc}$, van den Bosch et al. 2006) making them ideal candidates to study cluster dynamics. In the same region, two low mass X-ray binaries (LMXBs, thought of as progenitors to MSPs, e.g. Tauris & van den Heuvel, 2006 and references therein) have been reported (Giacconi et al. 1974; Auriere et al. 1984; White & Angelini 2001). One

[1] For a compilation of all globular cluster pulsars see the webpage by Paulo Freire: http://www.naic.edu/~pfreire/GCpsr.html

[2] http://www.atnf.csiro.au/research/pulsar/psrcat/, accessed November 18 2013

of them, 4U 2129+12 (AC211), is also detectable as a compact source in the radio regime. This relatively high concentration of compact objects that have been or currently are in a binary system is already indicative of the high stellar density within the core region of M15. In fact, the observed central brightness peak and the stellar velocity dispersion profile gave rise to speculations that M15 could host an intermediate mass black hole (IMBH, e.g. Newell et al. 1976). The predicted IMBH mass $M_\bullet = 1700^{+2700}_{-1700}$ (Gerssen et al., 2003) has, however, been ruled out by Kirsten & Vlemmings (2012). Alternatively, a collection of ~ 1600 dark remnants such as stellar mass black holes, NSs, and white dwarfs in the central region of M15 could drive cluster dynamics (Baumgardt et al. 2003; McNamara et al. 2003; Murphy et al. 2011). Based on the 1.5 GHz radio luminosity and assuming a minimum pulsar luminosity of $2\,\mu$Jy, Sun et al. (2002) estimate that M15 could host up to ~ 300 pulsars beaming towards Earth.

In this project, we accurately measure the proper motion of all compact objects detectable within our field of view and monitor their variability. Apart from the eight pulsars and the LMXB AC211, two further compact radio sources were reported previously by Machin et al. (1990) and Knapp et al. (1996). Those authors could, however, put no tight constraints on those sources' (non-) association with the cluster. Furthermore, we look for previously undetected compact objects within the observed region that might turn out to be pulsars.

The double neutron star system M15C has shown a number of unusual glitches which need to be fitted with a number of parameters that are highly covariant with fits for the proper motion. In particular, the measurement of the orbital period decay caused by the emission of gravitational waves is influenced by an acceleration in the cluster potential and by a contribution due to a transverse motion ("Shklovskii effect", see Lorimer & Kramer, 2005). Thus determining the transverse motion of the pulsar will allow a better measurement of the line of sight acceleration of the system within the cluster potential. Once the proper motion is determined independently of any model, the covariances in the fits to the timing model can be removed, improving the measurement of all relativistic parameters.

M15A is very close to the core and has a negative period derivative, which implies it is accelerating at a fast rate in the cluster's potential. This acceleration rate has now been shown to vary with time (Jacoby et al., 2006). The detailed variation is of great interest to investigate the gravitational potential in the cluster center, but if we have only the timing it must be disentangled from the proper motion signal. Therefore, an independent estimate of the proper motion of the pulsar will allow a much less ambiguous interpretation of the variation of the acceleration of this pulsar.

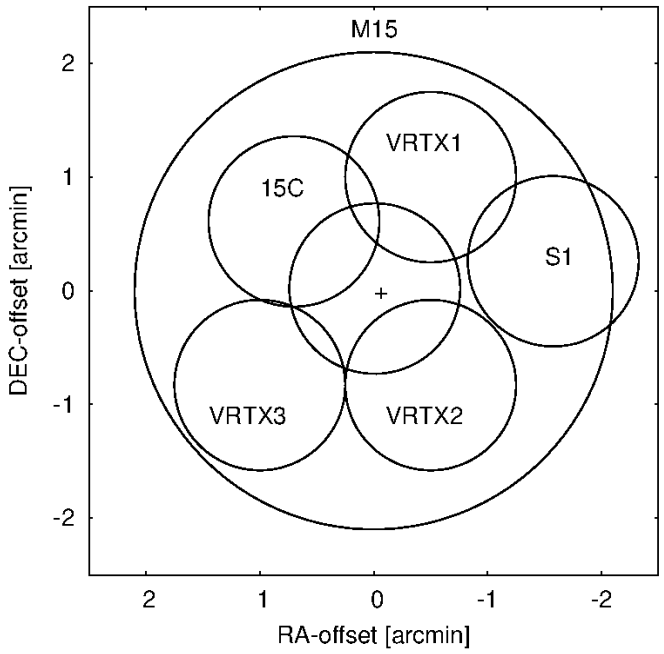

Fig. 6.1: The primary beam of the entire array (large circle, constrained by the Arecibo primary beam) and the position and FOV of the six correlation centers relative to the pointing center indicated by the cross at (0,0). The central circle with no label corresponds to the correlation center labeled AC211 in Table 6.2. The radius of the FOV is defined as to allow a maximal loss of 10% in the response of a point source caused by time and bandwidth smearing.

In the following we will first describe the data taking and data reduction process in section 6.2. The data analysis strategy and the results are the subject of section 6.3 while section 6.4 deals with the discussion of the implications of these results. The main findings of this project are briefly summarized in section 6.5.

6.2 Observations and data reduction

6.2.1 Observations

We observed M15 seven times at 1.6 GHz with a global VLBI array that included dishes of the European VLBI Network (EVN; Effelsberg, Jodrell Bank, Onsala, Noto, Toruń, Westerbork, Medicina) plus the Arecibo and the Green Bank Telescope (Table 6.1). The field of view (FOV) of about 2 arcmin (constrained by the Arecibo primary beam since only one dish of Westerbork was used) is large enough to cover all of the know compact sources in the cluster. The observing schedule encompassed six hours per epoch and was set up such that the target cluster M15 and the phase reference source, the quasar J2139+1423, located at $\sim$ 3.17 degrees towards the north-east of the pointing center, were observed in an alternating fashion: After

Table 6.1: Details of the observations

Epoch	Date	MJD	Array	rms [μJy beam^{-1}] dirty[(a)]	rms [μJy beam^{-1}] cleaned	beam size [mas x mas]
1	10 Nov 2009	55146	JbWbEfOnMcTrNtArGb	5.1	3.1	3.3 x 6.4
2	07 Mar 2010	55263	JbWbEfOnMcTrNtGb	8.5	5.4	2.3 x 30.9
3	05 Jun 2010	55352	JbWbEfOnMcTrNtArGb	6.7	4.6	3.0 x 6.6
4	02 Nov 2010	55503	JbWbEfOnMcTrGb	11.2	7.4	2.1 x 26.2
5	27 Feb 2011	55620	JbWbEfOnMcTrArGb	4.9	3.1	3.3 x 6.9
6	11 Jun 2011	55723	WbEfOnMcTrArGb	5.8	3.8	2.3 x 6.2
7	05 Nov 2011	55871	JbWbEfOnMcTrArGb	5.2	3.3	3.1 x 7.0

Notes. [(a)] Applying natural weights without any cleaning.

Table 6.2: Correlation Centres throughout M15

Name	Ra	Dec
M15 (epoch 1 only)	21:29:58.3500	12:10:01.500
AC211	21:29:58.3120	12:10:02.679
15C	21:30:01.2034	12:10:38.160
S1	21:29:51.9025	12:10:17.132
VRTX1	21:29:56.3050	12:11:01.500
VRTX2	21:29:56.3050	12:09:11.500
VRTX3	21:30:02.4410	12:09:11.500

each 3.5 minute scan of M15 we observed J2139+1423 for roughly 1.2 minutes. Altogether, the total integration time on M15 amounts to about 3.6 hours in each of the seven epochs, roughly 1.5 hours of which Arecibo was able to observe the GC. Due to technical failure no Arecibo data is available for epochs two and four.
All data were correlated at the Joint Institute for VLBI in Europe (JIVE). Epochs one to five were correlated on the EVN-MkIV correlator (Schilizzi et al., 2001) while epochs six and seven were correlated on the EVN software correlator at JIVE (SFXC[3], Keimpema 2014, in preparation). In the first epoch, the correlation centre is the same as the pointing center at RA = $21^{\mathrm{h}}29^{\mathrm{m}}58\overset{\mathrm{s}}{.}350$, Dec = $12°10'01\overset{''}{.}500$ (J2000). In order to avoid bandwidth and time smearing the first epoch was correlated at a spectral resolution of 512 channels per each of eight intermediate frequencies (IFs, bandwidth of 16 MHz each, dual polarisation) and at a temporal resolution of 0.25 sec. The size of the final data set (230 GB), however, made further data processing very slow. Consequently, subsequent epochs two to seven were still observed at the same pointing centre but correlated at six different positions centered on or close to sources detected in epoch 1 (Table 6.2). By using a much lower spectral (128 channels per IF) and temporal (integration time 0.5 sec) resolution, the size of each of the six data sets amounts to roughly 25 GB in each epoch. The FOV is ~ 0.75 arcmin (<10% smearing) for the individual centres which is large enough to cover most of the primary beam of Arecibo (Figure 6.1).

6.2.2 Data reduction and calibration

All data reduction and calibration steps are performed using the NRAO Astronomical Image Processing System (AIPS). The EVN pipeline[4] provides the a priori

[3]http://www.jive.nl/jivewiki/doku.php?id=sfxc
[4]http://www.evlbi.org/pipeline/user_expts.html

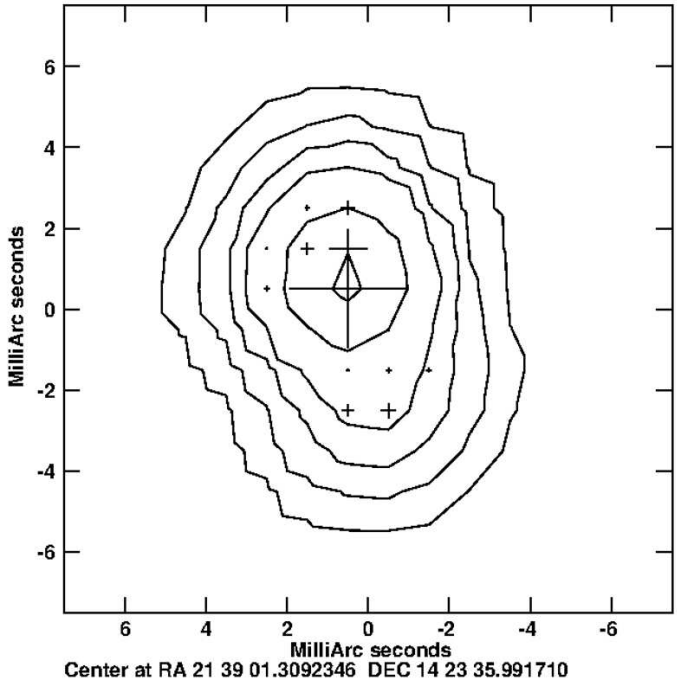

Fig. 6.2: Model of the phase calibrator used in the final calibration. For better illustration the CLEAN components used (marked by the crosses, the size of each cross indicates the relative associated flux density) were convolved with a circular beam of 2.6 mas FWHM (maximal resolution in right ascension). Contours are (10, 50, 150, 300, 900, 1800) times the rms of 0.46 mJy. Note the slightly extended structure in NE-SW direction.

system temperature and gain curve corrections as well as flags concerning off-source times and band edges. We apply these as given after which we correct the parallactic angle in CLCOR and also compute ionospheric corrections in TECOR with the help of total electron content maps as published by the Center for Orbit Determination in Europe[5].

In the next step we eliminate radio frequency interference (RFI). Due to the data volume we do not flag manually but instead use the AOFlagger (Offringa et al., 2010, 2012). This software package works with measurement sets which is why we first export the a priori calibrated data sets (target source and calibrator sources individually) to a fits file which is then read into the Common Astronomy Software Application package (CASA) to produce measurement sets. After successful automatic flagging we export each measurement set back to fits format in CASA during which all flags are applied to the data. The flagged data sets are then loaded back into AIPS. These steps are performed for each calibrator source and all correlation centers individually in each epoch. In cases where entire antennas, scans, or IFs were affected by RFI our flagging-strategy was insufficient to account for it. Therefore,

[5]ftp://ftp.unibe.ch/aiub/CODE/

we perform a further manual flagging step on the data averaged over all channels in each IF.

In a first calibration step we compute bandpass solutions, phase alignments and fringe rates independently for each epoch assuming a simple point source model for the phase calibrator. In epochs 3 and 7 the data of the bandpass calibrator source, the quasar 3C454.3, was affected by strong RFI resulting in a loss of considerable amounts of data. Therefore, for consistency reasons, we compute bandpass calibration tables from the phase calibrator source J2139+1423 using the entire time range in the individual epochs. For phase alignment between bands, we select a 30 sec time interval also from a scan of the phase calibrator. After fringe fitting the data with solution intervals of 1.5 min we also self-calibrate on J2139+1423. In self-calibration we solve for both amplitude and phase at solution intervals of 1.5 min. In each epoch we detect the phase calibrator at a signal to noise ratio (SNR) of 800–2200.

For the main calibration procedure, we produce a global phase calibrator model concatenating the calibrated data of J2139+1423 of all seven epochs. We use the clean components of the image as the global model for further calibration (Figure 6.2). We eventually rerun all of the calibration steps (except for self-calibration) on the phase calibrator but instead of assuming a simple point source model we apply our global model.

The angular size of the primary beam allows us to detect the strong unclassified source S1 (Machin et al., 1990; Johnston et al., 1991). This object lies ~ 1.5 arcmin to the west of the cluster core. We detect it at peak flux densities of 2–4 mJy beam^{-1}; at this strength it can serve ideally as in-beam calibrator eliminating residual phase errors caused by atmospheric differences in the lines of sight to phase calibrator and target cluster. S1 is most likely of extragalactic origin (see section 6.4.3) and, therefore, we select the image with the highest SNR (epoch 3) as model for further in-beam self-calibration. Thus the position of S1 is fixed to RA $= 21^{\mathrm{h}}29^{\mathrm{m}}51\overset{\mathrm{s}}{.}9034555$, Dec $= 12°10'17\overset{''}{.}13240$. Finally, we self-calibrate all epochs applying this model.

All calibration steps are performed on the data set named S1 in Table 6.2. Once all solution (SN) tables are computed they are combined into one final calibration (CL) table. Since the pointing center is identical for all six correlation centers, the calibration tables obtained for one sub-center can easily be applied to the other ones speeding up data processing significantly. This is true for all epochs except epoch 1. Due to the different observational setup and correlation strategy, bandpass calibration, phase alignment and fringe rate solutions are applied to the entire data. Before self-calibration on S1 we shift the data to the six different correlation centers

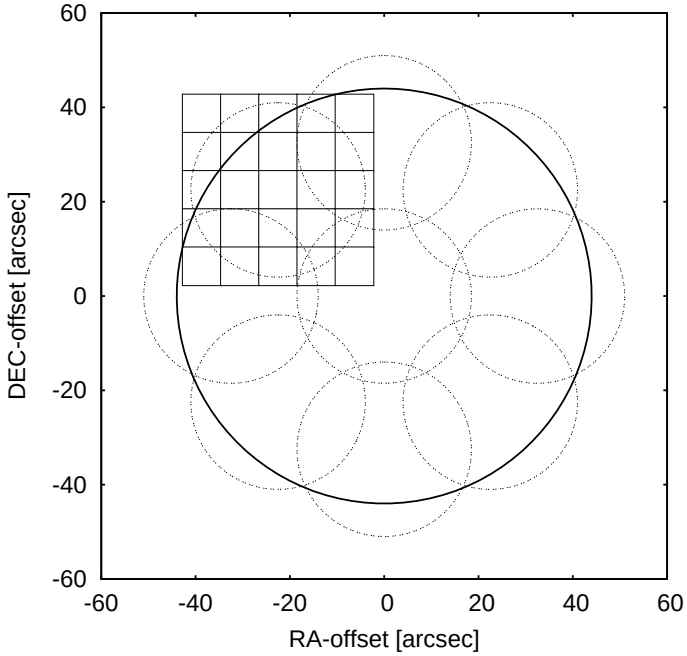

Fig. 6.3: Imaging strategy. The large solid circle indicates the FOV of one sub-center, the small dashed circles represent the relative position and the FOV of the shifted and averaged data sets. The grid of rectangles illustrates the size and relative position of each produced image. See text for details.

of the subsequent epochs. This step is done using the technique described in Morgan et al. (2011). Afterwards, we average the six data sets to the same spectral and temporal resolution as in epochs 2 to 7 and continue with self-calibration on S1.

6.2.3 Imaging

Once all calibration tables are applied the data of each correlation center is shifted to nine positions throughout the FOV of each correlation center using the AIPS task UVFIX. The separation in RA and DEC from the coordinates of each correlation center are 32.5 arcsec for the horizontal and vertical positions while it is 22.5 arcsec for the diagonal positions (Figure 6.3). This data is averaged to 64 channels per IF and 2 sec integration time (FOV$\sim$ 18 arcsec for $<$10% smearing) before imaging with natural weights. The images have a dimension of 8192×8192 pixels each at a resolution of 1 mas/pixel. To image one of the nine shifted and averaged data sets we produce 25 images whose central coordinates are separated by 8.1 arcsec in right ascension and declination. In total we required 25 images$\times$9 shifts$\times$6 correlation centers=1350 images in each of seven epochs to image the entire primary beam. For source detection we also compute noise maps for each image with the AIPS task RMSD. The entire imaging process described above was done in a parallelized script

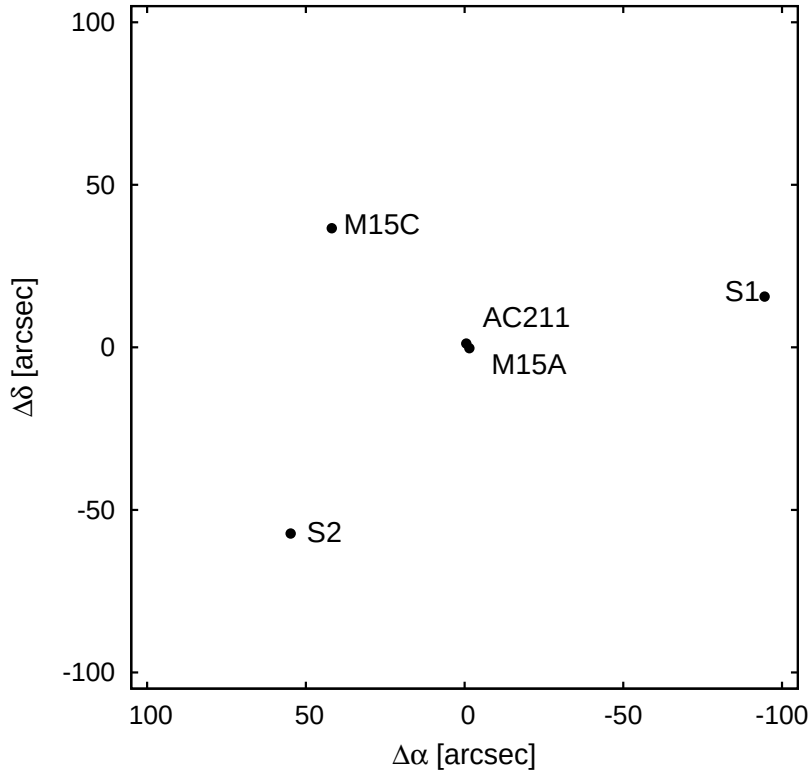

Fig. 6.4: Distribution of the detected sources relative to the pointing center.

written in ParselTongue (Kettenis et al., 2006).

6.3 Results

6.3.1 Detected sources

Based on the CLEANed image and its corresponding noise map the AIPS task SAD was used to search for sources down to an SNR > 4. In the following, we cross-correlate all potential candidates in between epochs allowing for a positional offset $\leq$25 mas. Only potential candidates found in at least three epochs were followed up for further analysis. All positions were extracted from a Gaussian fit to the brightness distribution of each source in the image plane using the AIPS task IMFIT. Figure 6.4 displays the distribution of the five detected sources: The two pulsars M15A (PSR B2127+11A) and M15C (PSR B2127+11C), the LMXB AC211 (4U 2129+12), and the two unclassified sources S1 and S2 (Knapp et al., 1996). Except for M15C we observe all objects in each of the seven epochs. The double neutron star system M15C was only observable in epochs 1, 3, and 7 for reasons discussed in section 6.4.5. We fit the measured positions of all detected sources for parallax

Table 6.3: Details of the astrometric fits for all detected sources. For the proper motion results and the goodness-of-fit, $\chi^2_{\rm red}$, the results for a fixed parallax $\pi = 0.1$ and for the fitted parallax, $\pi_{\rm fit}$, are listed. The positions listed are for the indicated MJDs (epochs with the best SNR). For S1 the positions were measured relative to the phase calibrator while the positions of the remaining sources were measured relative to S1.

	Ra (J2000)	Dec (J2000)	Epoch (MJD)	SNR	d [a] [arcsec] [pc]	$\pi_{\rm fit}$ [mas]	$\mu_\alpha^{\pi=0.1}$ $\mu_\alpha^{\pi_{\rm fit}}$ [mas yr^{-1}]	$\mu_\delta^{\pi=0.1}$ $\mu_\delta^{\pi_{\rm fit}}$ [mas yr^{-1}]	$\chi^{2,\,\pi=0.1}_{\rm red}$ $\chi^{2,\,\pi_{\rm fit}}_{\rm red}$
M15A	21:29:58.246512 (4)	12:10:01.2339 (1)	55146	24	1.2 (3) 0.06 (1)	−0.02 (10)	−0.54 (14) −0.56 (14)	−4.33 (25) −4.34 (25)	1.4 1.3
M15C	21:30:01.203493 (7)	12:10:38.1592 (2)	55146	15	56.0 (3) 2.79 (1)	0.22 (17)	−0.75 (9) −0.76 (10)	−3.52 (13) −3.53 (15)	0.7 0.9
AC211	21:29:58.312403 (4)	12:10:02.6740 (2)	55871	24	1.5 (3) 0.07 (1)	0.17 (7)	−0.46 (8) −0.49 (8)	−4.31 (20) −4.32 (20)	3.4 3.4
S1	21:29:51.9034555 (4)	12:10:17.13240 (1)	55352	287	95.5 (3) 4.77 (1)	0.04 (25)	+0.06 (28) +0.05 (30)	+0.53 (59) +0.53 (62)	2749 3034
S2	21:30:02.085700 (8)	12:09:04.2203 (2)	55871	17	79.2 (3) 3.95 (1)	0.45 (8)	−0.07 (13) −0.05 (8)	−1.26 (29) −1.27 (17)	2.9 1.0

Notes. [a] Distance (in arcsec and pc) from the assumed cluster center at RA = $21^{\rm h}29^{\rm s}58\overset{\rm s}{.}330\pm0\overset{\rm s}{.}013$, Dec = $12^\circ10'01\overset{''}{.}2\pm0\overset{''}{.}2$ (Goldsbury et al., 2010)

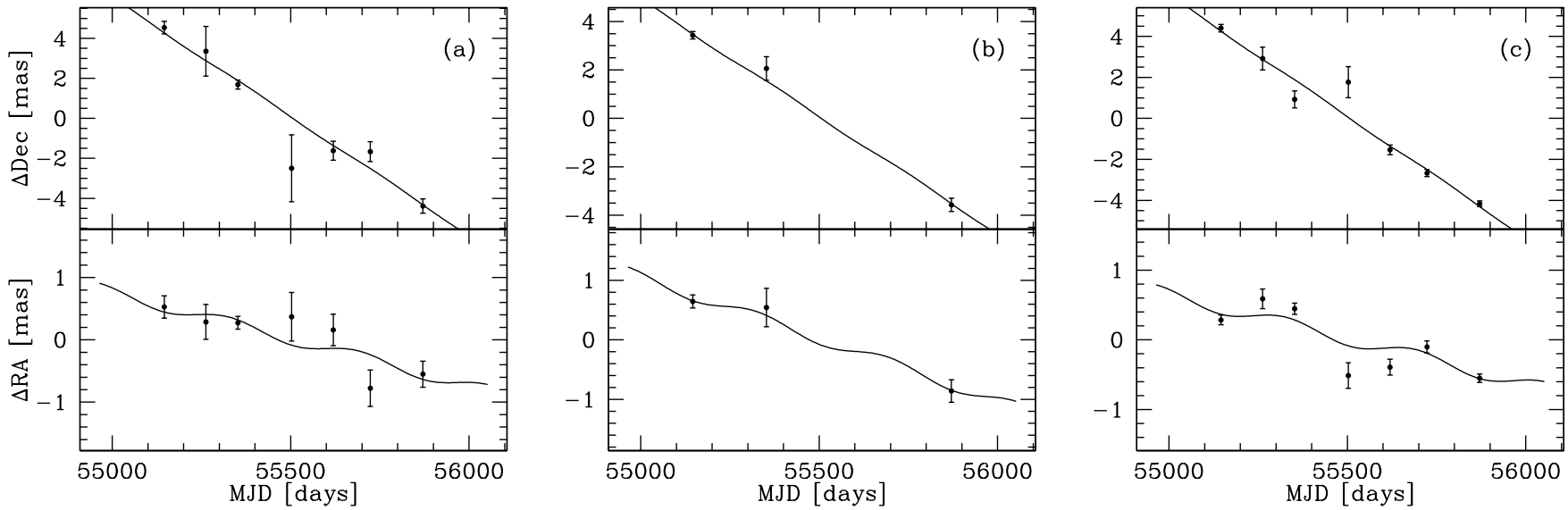

Fig. 6.5: Relative changes in positions relative to the in-beam calibrator S1 in Dec (top panels) and RA (bottom panels) for (a) pulsar M15A, (b) pulsar M15C, (c) the LMXB AC211. The solid line is a fit to position and proper motion keeping the parallax fixed at $\pi = 0.1$.

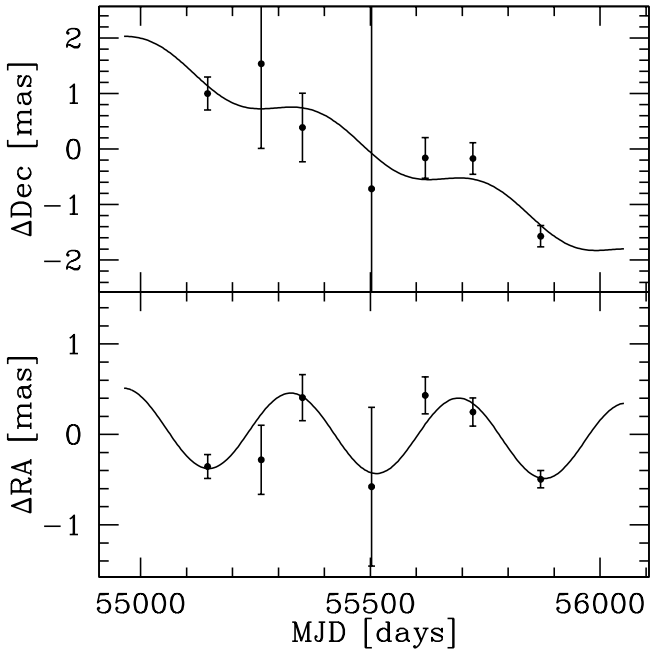

Fig. 6.6: The same as Figure 6.5 but for S2. Here we kept the parallax as free parameter.

and proper motion. The results for each object are summarized in Table 6.3.
The two pulsars and the LMXB are known to be members of M15 while the origins of S1 and S2 are a priori unclear. Based on the well known distance of M15 ($d = 10.3 \pm 0.4$ kpc, van den Bosch et al., 2006) we once fit for both the parallax and the proper motion and we also fit the data only for the proper motion keeping the parallax fixed at the expected value of $\pi = 0.1$ mas. In case of the three sources known to be cluster members (Figure 6.5) the fit quality achieved is very similar in both approaches. Moreover, the fitted parallax is in agreement with the expected one for the given distance within the uncertainties. The positional uncertainties are estimated by the formal error, beam size/(2*SNR), which is appropriate given the close proximity to the in-beam calibrator S1, relative to which the positions were measured. The proper motion results do not change significantly regardless of whether or not we fit for the parallax. Overall, the proper motions we measure for M15A and M15C agree with those obtained from pulsar timing by Jacoby et al. (2006).
We applied the same two fitting strategies in the case of S2 where the fit to the measured positions of the source (Figure 6.6) improves significantly when treating the parallax as free parameter (see Section 6.4.4).
The astrometric fits for S1 (Figure 6.7) are of very poor quality regardless of fitting strategy. This is indicative of unmodeled systematic errors, especially since the high flux density of the source results in very small formal errors ($\sim 10\,\mu$as in RA and

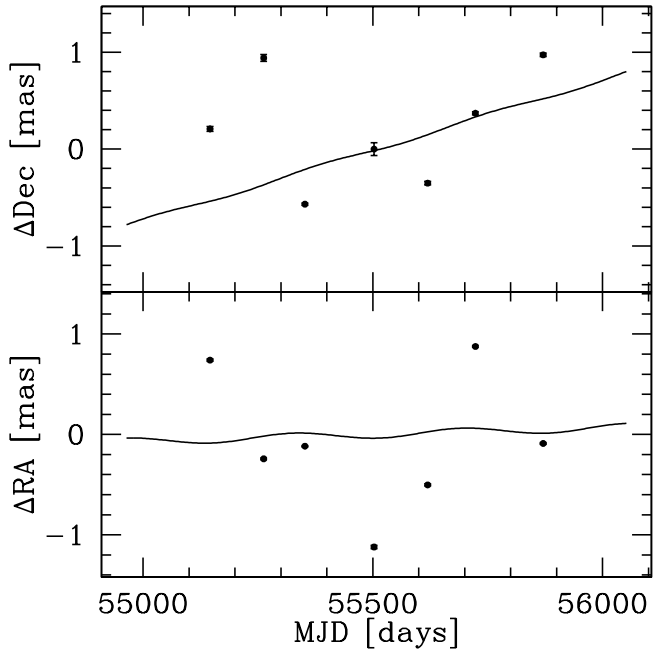

Fig. 6.7: The same as Figure 6.5 but for the in-beam calibrator S1. Here, the positions are measured relative to phase calibrator and the parallax is kept as free parameter in the fit. The error bars are estimated by the formal errors and are smaller than the data points. See text for details.

$\sim 40\,\mu$as in Dec). Given the relatively large angular separation ($\sim 3\overset{\circ}{.}17$) between S1 and the phase calibrator relative to which the position of S1 is measured, the real uncertainties may contain a correspondingly large contribution from unmodelled differential ionospheric phase perturbations along the lines of sight to the two sources (e.g. Chatterjee et al., 2009). To reflect these the formal errors stated above should be a factor of about 50 higher. This would also be in agreement with the trend in the correlation of position uncertainties and calibrator throw as predicted by Figure 3 in Chatterjee et al. (2004). The implications of the fitting results for S1 and S2 are discussed in Section 6.4.

6.3.2 Undetected sources

Of the eight known pulsars in M15 we do not detect six. Based on the published flux densities S_ν at $\nu = 400\,$MHz (Table 6.4) and our best sensitivity limits (rms$\sim 3.5\,\mu$Jy, Table 6.1) at $\nu = 1.6\,$GHz we can, however, derive a lower limit for the spectral index α of these sources ($S_\nu \propto \nu^{-\alpha}$). Taking the 4σ upper flux density limit of $S_{1600} \leq 14\,\mu$Jy/ Beam we find $\alpha \geq 1.4$ for all of the undetected pulsars. In the case of the detected pulsars B2127+11A and B2127+11C our results are in agreement with the canonical value $\alpha = 1.8 \pm 0.2$ (Maron et al., 2000) and also with the latest

Table 6.4: Pulsar flux densities and inferred spectral index.

	S_{400} [μJy]	S_{1600} [μJy]	α
B2127+11A	1700[a]	100	2.0
B2127+11B	1000[b]	<14	>3.0
B2127+11C	600[b]	50	1.8
B2127+11D	300[b]	<14	>2.2
B2127+11E	200[b]	<14	>1.9
B2127+11F	100[b]	<14	>1.4
B2127+11G	100[b]	<14	>1.4
B2127+11H	200[b]	<14	>1.9

Notes. [a] Wolszczan et al. (1989), [b] Anderson (1993)

analysis of the pulsar spectral index distribution suggesting $\alpha = 1.4 \pm 0.96$ (Bates et al., 2013). The unusually high value $\alpha \geq 3.0$ for B2127+11B lies even outside the broader distribution from Bates et al. (2013). Either the intrinsic spectral index of this pulsar is particularly steep or the cataloged flux density ν_{400} was affected by scintillation. Given the close proximity ($\approx 5.7''$) of B2127+11B to B2127+11A and the fact that we do not see any evidence for scintillation for B2127+11A we exclude that our observations were affected by scintillation.

6.4 Discussion

6.4.1 Implications of proper motion measurements on peculiar velocities of cluster members

From the measured proper motions of the sources known to be cluster members (M15A, M15C, AC211) we can estimate the transverse velocities of these objects relative to the cluster. Here, we estimate the global motion of the cluster in three ways: (i) we take the average in $\mu_\alpha^{\pi=0.1}$ and $\mu_\delta^{\pi=0.1}$ of all three sources; (ii) we take the proper motion of M15C because of its large angular distance from the cluster core expecting its motion to be least affected by the gravitational potential of the central mass concentration; (iii) we take the average of M15A and AC211 because of their proximity to the cluster core assuming their peculiar velocity has a radial component only. The results are summarized in Table 6.5.

Table 6.5: Global motion of M15 and implied peculiar transverse velocities of the detected cluster members. Case (i), (ii), and (iii) refer to the average of (i) all three cluster members; (ii) only M15C; (iii) only M15A and AC211 as proxy for the global cluster motion.

	μ_α [mas yr^{-1}]	μ_δ [mas yr^{-1}]	M15A [km s^{-1}]	AC211 [km s^{-1}]	M15C [km s^{-1}]
Cudworth & Hanson (1993)	-0.3 ± 1.0	-4.2 ± 1.0	12	9	38
Geffert et al. (1993)	-1.0 ± 1.4	-10.2 ± 1.4	279	280	316
Scholz et al. (1996)	-0.1 ± 0.4	$+0.2 \pm 0.3$	215	214	178
Odenkirchen et al. (1997)	-2.5 ± 1.5	-8.3 ± 1.5	209	212	241
Jacoby et al. (2006)	-1.0 ± 0.4	-3.6 ± 0.8	40	42	12
This work case (i)	-0.58 ± 0.18	-4.05 ± 0.34	13	13	26
This work case (ii)	-0.75 ± 0.09	-3.52 ± 0.13	39	39	0
This work case (iii)	-0.50 ± 0.16	-4.32 ± 0.32	1	1	39

Case (i) yields the most realistic and most conservative estimate for the global motion of the cluster. The inferred peculiar velocity of all three cluster members is well below the escape velocity of M15 ($v_{\rm esc} \approx 50\,{\rm km\,s^{-1}}$ at the position of M15A and AC211 and $v_{\rm esc} \approx 30\,{\rm km\,s^{-1}}$ at the position of M15C, Phinney, 1993). We note however, that the implied peculiar velocity of M15A and AC211 is lower compared to the one of M15C. Given the close proximity of M15A and AC211 to the cluster core we would expect the opposite. Since the given global motion is based on small number statistics this might only be accidental: The peculiar velocity of M15A and AC211 seem to be very similar and, therefore, shift the average cluster motion in their favor. Alternatively, the higher peculiar velocity of M15C might only be a projection effect. The period derivative of M15A is negative indicating that the pulsar is being accelerated in the direction of the line of sight (Wolszczan et al., 1989). The same could be true for AC211 resulting in a larger 3d-velocity of M15A and AC211 than that of M15C.

Cases (ii) and (iii) yield the limiting but opposite possible transverse velocities for all three cluster members. Case (ii) implies a transverse velocity $v_{\rm trans} \sim 39\,{\rm km\,s^{-1}}$ for both M15A and AC211 while M15C would only have a radial velocity component. Taking the uncertainties of the proper motion into account, M15A and AC211 have a relative transverse velocity of at most $v_{\rm trans}^{\rm rel} = 27\,{\rm km\,s^{-1}}$. Hence, the highest possible transverse velocity of any of the two sources $v_{\rm trans}^{\rm max} = 66\,{\rm km\,s^{-1}}$, significantly above $v_{\rm esc}$.

Case (iii) implies hardly any peculiar transverse motion of M15A and AC211 within the cluster. Given their projected distance from the core (0.06 pc and 0.07 pc for M15A and AC211, respectively) and assuming a central mass of $3400\,{\rm M_\odot}$ (van den Bosch et al., 2006) the negligible transverse velocity implies a radial velocity $v_r \sim 15\,{\rm km\,s^{-1}}$ if both sources are on a stable orbit around the cluster core. It is, however, very unlikely that both sources are on an orbit coinciding directly with the line of sight to M15. We conclude that case (i) is the best estimate for the global motion of M15.

Table 6.5 lists the previously published proper motion determinations for the globular cluster M15 as a whole. All were based on stellar proper-motion measurements, except that of Jacoby et al. (2006), which was based on pulsar timing. The values of Cudworth & Hanson (1993) and of Jacoby et al. (2006) agree with our results within the uncertainties. The implied peculiar transverse motions of M15A, M15C, and AC211 are also below $v_{\rm esc}$. In combination with our measurements, the remaining three published results would indicate velocities relative to the cluster of about $250\,{\rm km\,s^{-1}}$ for all three cluster members discussed here. Given the cluster escape

velocity we can exclude these results based on the assumption that all three compact objects are bound to M15.

6.4.2 Undetected pulsars in context of the pulsar luminosity function

The complementary cumulative frequency distribution function (CCFDF) of pulsar luminosities, $N(\geq L_\nu) = N_0 L_\nu^\beta$, is a measure for the expected number of pulsars N brighter than the pseudo luminosity $L_\nu = S_\nu d^2$ (Bagchi 2013, and references therein). The parameter N_0 denotes the number of observable pulsars above the limiting pseudo luminosity $L_{\nu,\mathrm{min}} = 1\,\mathrm{mJy\,kpc^2}$ and β describes the power law dependence. Here, we adopt the latest results for the pulsars in M15 of $(N_0,\, \beta) = (8^{+3}_{-2},\, -0.83 \pm 0.34)$ for $\nu = 1400\,\mathrm{MHz}$ from Bagchi & Lorimer (2011). Furthermore, we convert our upper flux density limit $S_{1600} = 14\,\mu\mathrm{Jy}$ to $L_{1400} = 1.9\,\mathrm{mJy\,kpc^2}$ (assuming $\alpha = 1.8$ and $d = 10.3\,\mathrm{kpc}$). Accordingly, we estimate the number of pulsars we should have observed to $N(\geq L_{1400}) = 5^{+3}_{-2}$ of which we only detect two. In comparison, Hessels et al. (2007) report a limiting pseudo luminosity $L_{1400} = 2.1\,\mathrm{mJy\,kpc^2}$ which allows them to detect five pulsars in the GC, well consistent with the CCFDF predicting $N(\geq L_{1400}) = 4^{+3}_{-2}$. Despite our observations being more sensitive, the difference in the number of detected pulsars can be explained by the fact that Hessels et al. (2007) performed pulse searches while our data is pure continuum.

6.4.3 Extragalactic origin of S1

A priori, it was unclear whether the source S1 is a member of M15, a Galactic back-/foreground source or whether it is of extragalactic origin. After initial imaging and self-calibration of S1 we perform the first astrometric analysis. Figure 6.7 shows the position of the source relative to the phase calibrator in each epoch. The measured positions scatter about a central position with an offset of ~ 1 mas (= 1 pixel in the image plane). A fit to parallax, π, and proper motion, $(\mu_\alpha,\, \mu_\delta)$, yields $\pi = 0.04 \pm 0.25\,\mathrm{mas}$, $(\mu_\alpha, \mu_\delta) = (0.05 \pm 0.30,\, 0.53 \pm 0.62)\,\mathrm{mas\,yr^{-1}}$. With parallax and proper motion measurements consistent with zero, an extragalactic origin for S1 is the most natural conclusion. Within the uncertainty of π, however, the hypothesis that S1 is related to the cluster cannot be excluded. Therefore, we check the alternate hypothesis that S1 is a cluster member by considering its proper motion relative to that of the GC. Using case (i) from Table 6.5 for the GC and adding the proper-motion uncertainties for the two objects in quadrature, this relative proper motion

evaluates to $(\mu_\alpha^{\rm rel}, \mu_\delta^{\rm rel}) = (0.63 \pm 0.35,\ 4.58 \pm 0.70)\,{\rm mas\,yr^{-1}}$, which in turn translates to a transverse velocity of S1 relative to the GC of $220^{+30}_{-32}\,{\rm km\,s^{-1}}$. This value is much larger than the escape velocity at its position ($24.1\,{\rm km\,s^{-1}} < v_{\rm esc} < 29.3\,{\rm km\,s^{-1}}$, Phinney, 1993) and rules out that S1 and M15 are related.

6.4.4 Galactic origin of S2

In Table 6.3 we list the results of both fitting strategies with and without parallax. If the parallax is kept fixed at $\pi = 0.1\,{\rm mas}$, suggesting S2 to be a member of M15, we measure a proper motion $(\mu_\alpha,\mu_\delta) = (-0.07 \pm 0.13, -1.26 \pm 0.29)\,{\rm mas\,yr^{-1}}$. These values are significantly different from the ones we measure for the cluster members. Adopting our case (i) scenario for the global motion of M15 (Table 6.5), the measured proper motion would translate to a peculiar transverse velocity $v_t^{\rm S2,pec} = 142^{+4}_{-3}\,{\rm km\,s^{-1}}$ at PA $= 10°$, opposite to the direction of motion of M15 (PA $= 188°$). At the angular distance of S2 to the cluster core (Figure 6.4, Table 6.3) this velocity would indicate that S2 is not bound to M15 ($24.1\,{\rm km\,s^{-1}} < v_{\rm esc} < 29.3\,{\rm km\,s^{-1}}$, Phinney, 1993). Hence, it seems unlikely that S2 is related to the cluster.

If we take the parallax as free parameter the results for the proper motion remain the same within the uncertainties but the fit quality increases by a factor of 3. The change in $\chi^2_{\rm red}$ can be quantified in an F-test (e.g. Bevington, 1969; Stuart & Ord, 1994). Given the observed F – the ratio between the reduced chi-squares resulting from the fits in which parallax was (i) fixed at 0.1 mas and (ii) treated as a fittable parameter, which here is 2.9 – and the different numbers of degrees of freedom, $\nu_1 = 10$ (fixing $\pi = 0.1$) and $\nu_2 = 9$ (fitting for π) we can compute the probability P_F of random data producing such an improvement in the value of reduced chi-square in the latter fit:

$$P_F(F;\,\nu_1,\,\nu_2) = \int_F^\infty P_f(f;\,\nu_1,\,\nu_2)\,{\rm df},$$

with

$$P_f(f;\,\nu_1,\,\nu_2) = \frac{\Gamma[\frac{\nu_1+\nu_2}{2}]}{\Gamma[\frac{\nu_1}{2}]\Gamma[\frac{\nu_2}{2}]} \cdot \left(\frac{\nu_1}{\nu_2}\right)^{\frac{\nu_1}{2}} \cdot \frac{f^{\frac{\nu_1-2}{2}}}{(1+f\frac{\nu_1}{\nu_2})^{\frac{\nu_1+\nu_2}{2}}}\,.$$

Evaluating $P_F(2.9;\,10,\,9)$ yields 0.062. Hence, we can reject the hypothesis of random data producing a ratio $F \geq 2.9$ at the 94% confidence level. Therefore, we conclude that the measured parallax $\pi = 0.45 \pm 0.08\,{\rm mas}$ is real. This value indicates that S2 is of Galactic origin and, furthermore, that it is a foreground source at a distance $d = 2.2^{+0.5}_{-0.3}\,{\rm kpc}$. After correcting for solar motion (with the relevant solar parameters taken from Schönrich, 2012) and also for differential galactic rotation

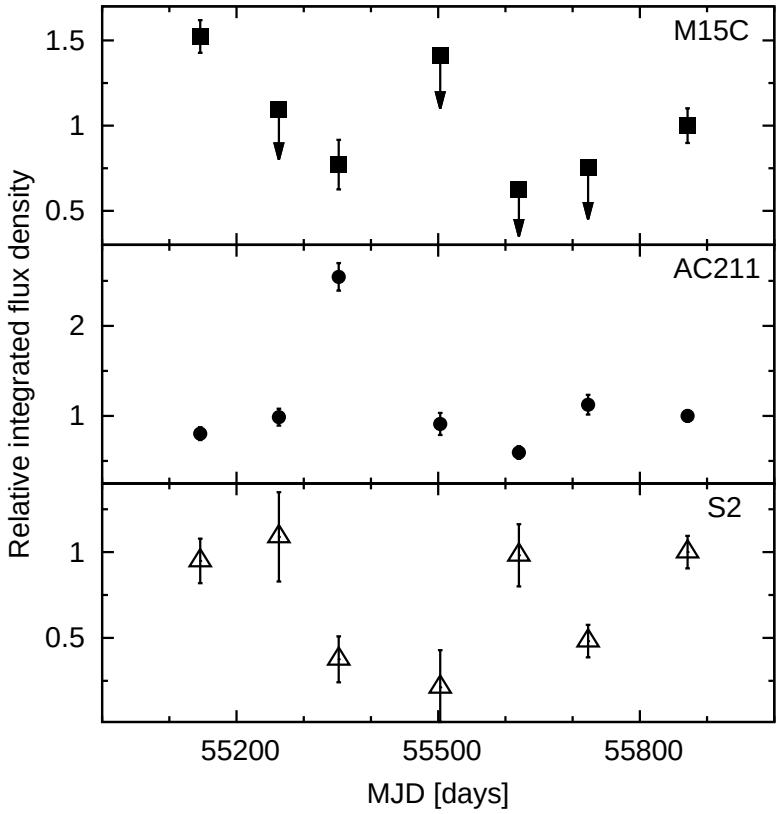

Fig. 6.8: Relative integrated flux density evolution of significantly variable sources normalized to the integrated flux density in epoch 7 ($32 \pm 3\,\mu$J, $224 \pm 14\,\mu$J, $214 \pm 20\mu$J for M15C, AC211, and S2, respectively). From top to bottom: M15C, AC211, S2. For the pulsar M15C only 4σ upper flux density limits are indicated for epochs 2, 4, 5, and 6. For AC211 in epoch 3 the flux is integrated over both components.

(with the Oort constants A and B as published by Feast & Whitelock, 1997) our measured proper motion $(\mu_\alpha, \mu_\delta) = (-0.05 \pm 0.08, -1.27 \pm 0.17)\,\mathrm{mas\,yr^{-1}}$ (Figure 6.6) implies a transverse velocity $v_t^{\mathrm{S2}} = 26^{+5}_{-4}\,\mathrm{km\,s^{-1}}$ with respect to the local standard of rest (LSR) at position angle PA $= -51°$(PA in equatorial coordinates). We discuss the nature of S2 in the following section.

6.4.5 Variability of sources

M15C

The proper motion results for the double neutron star system M15C are based on three observations only (epochs 1, 3, and 7, Figure 6.5(b)). The non-detection in epochs 2 and 4 is mostly due to the fact that those epochs were observed without the Arecibo dish which is essential to obtain the sensitivity required to detect this system. Apart from this fact, however, the measured flux density of M15C decreased between epochs 1 and 3 only to fade beyond detection as of epoch 5 (Figure 6.8).

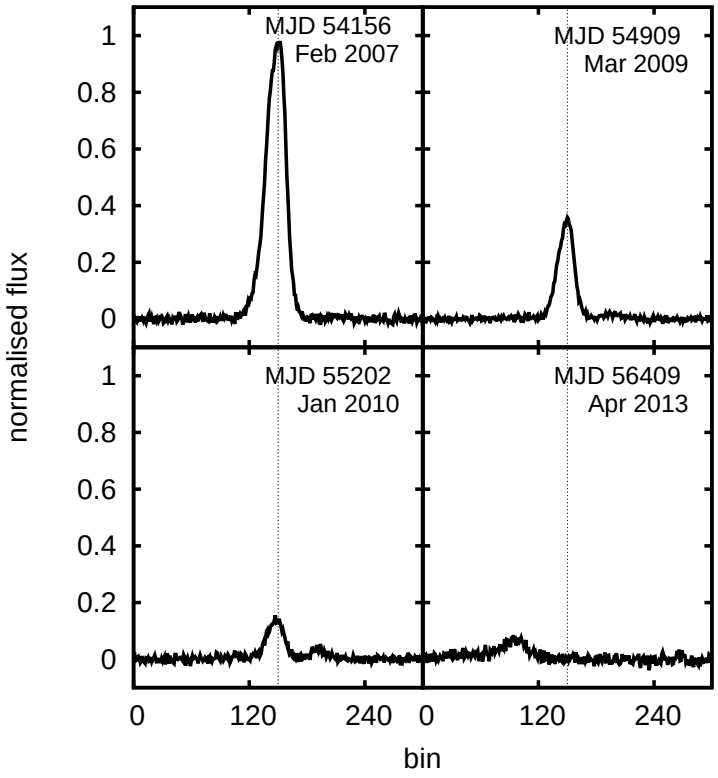

Fig. 6.9: Pulse profile evolution of M15C as observed at Arecibo. The pulsar slowly faded away over the course of about three years, probably due to geodetic precession. The horizontal dotted line indicates the central location of the peak as observed until January 2010. The shift in the location of the central peak in the bottom right panel is consistent with a 2.5% phase shift observed in the timing observations (only the relevant $\sim$ 10% of the pulse phase are shown here). This shift is indicative of an emission component different than the one observed up to 2010 that moved into our line of sight due to geodetic precession (Ridolfi et al. 2014, in preparation). There were no observations at Arecibo between MJD 55202 and MJD 56409.

In epoch 7 the pulsar was observable again. To confirm the reappearance of the source we performed single dish follow-up observations with the Arecibo telescope which had previously stopped monitoring the system due to its low flux density. Previously, regular timing observations had also revealed a steady decrease in peak flux density and also a change in pulse profile (Figure 6.9, Ridolfi et al. 2014, in preparation). Our follow-up observations (bottom right panel of Figure 6.9) confirm that the emission we detect in epoch 7 is related to M15C. They also reveal, however, a shift in pulse peak location that is consistent with a 2.5% phase shift observed in the timing observations (Ridolfi et al. 2014, in preparation). A possible explanation for this behavior is geodetic precession: due to orbit-spin coupling the axis of rotation of the one neutron star we see as a pulsar precesses, moving the emission region

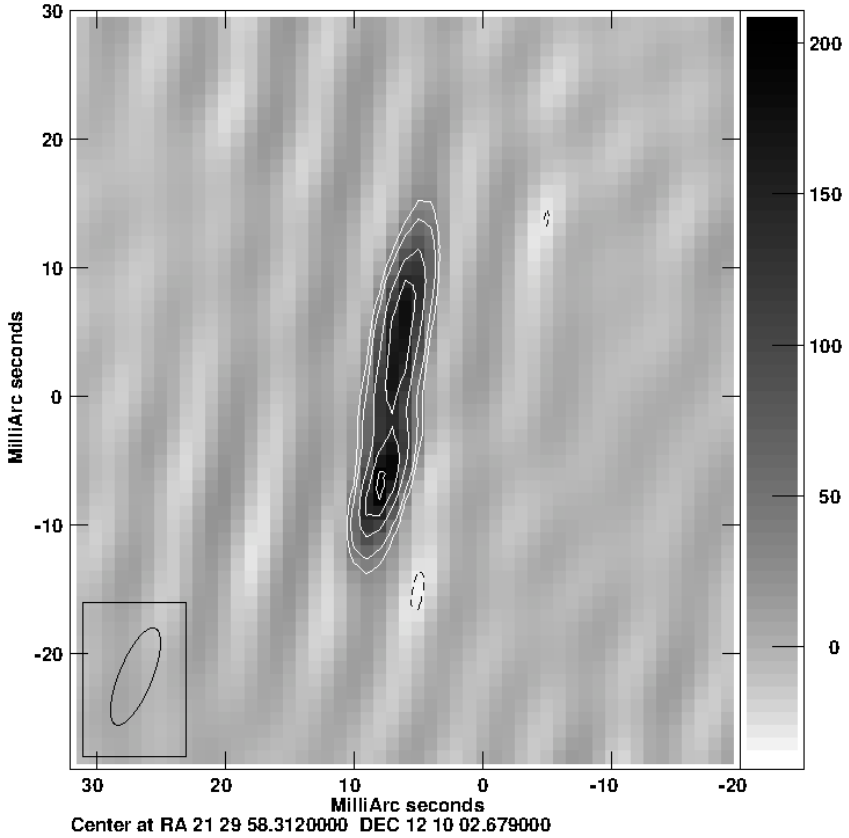

Fig. 6.10: Clean image of AC211 in epoch 3 (MJD 55352) exhibiting the double lobed structure. Contours are (-3, 3, 5, 10, 15, 20) times the noise level $rms = 9.5\,\mu$Jy/beam. The beam size and position angle are shown in the bottom left corner.

out of our line of sight. The same effect then moves a different component of the emission cone into our line of sight, which we detect at a slightly different phase.

AC211

The integrated flux density of AC211 varied slightly about an average value of $\sim 200\,\mu$Jy. This is true for all observations but epoch 3. In this observation at MJD 55352 we measure an integrated flux density $S_{int} = 570 \pm 34\,\mu$Jy (Figure 6.8). Moreover, in this epoch the source exhibits a double lobed structure extending from north to south (Figure 6.10). We exclude the possible explanation of this structure by a phase error for two reasons: (i) When imaged, the close-by pulsar M15A (located at about 1.7 arcsec to the south-west of AC211) is an unresolved point source also in epoch 3. Any phase errors causing the observed structure in AC211 should result in a similar structure also for M15A. (ii) We can reproduce the structure independent of the data reduction and calibration strategy.

Therefore, we conclude that the observed bipolar structure is real and might have been caused by an outburst that occurred at some time between epochs 2 and 3. The

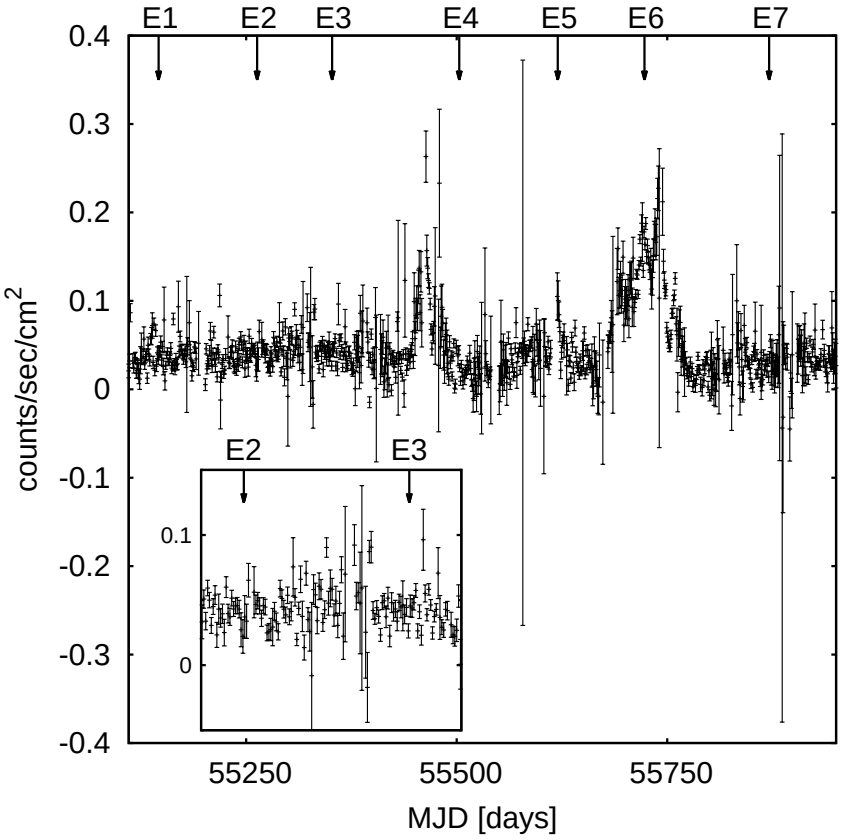

Fig. 6.11: X-ray lightcurve (2-20 keV) of M15 from the MAXI mission covering the time of this campaign. The inset is a blow-up of the timerange between epochs 2 and 3. Note the slight increase in count rate about 40 days prior to epoch 3.

X-ray data published by the *MAXI* mission[6] (Matsuoka et al., 2009) reveals X-ray variability of M15 during our observations that could be caused by the activity of AC211 (Figure 6.11).

At the distance of M15 the angular separation between the components corresponds to about 137 AU. The time span from epoch 2 to 3 is 110 days, the one from epoch 3 to 4 is 150 days. Assuming that the outburst occurred shortly after epoch 2 the transverse velocity v of the ejected material (ejected from an object in the middle of both components) would be roughly 0.6 AU per day corresponding to $v \approx 1000\,\mathrm{km/s}$. This velocity is very low compared to measured relativistic jet velocities of, e.g., the X-ray binaries SS433 ($v \sim 0.2$c, Stirling et al., 2002, and references therein) and GRS1915+105 ($v \sim 0.98$c, Fender et al., 1999, and references therein). Therefore, our measured velocity could well be real, especially if the outburst occurred at some time close to epoch 2. Turning the argument around, the outburst could have occurred only two days before our observations if we assume an ejection velocity of

[6]http://maxi.riken.jp

$v \sim 0.2$c.
In Fender et al. (1999) it also becomes clear that the radio flux density of individual components can decrease rapidly on the timescale of a few months. Hence, the time span of 150 days from epoch 3 to 4 is long enough for the ejected material to dissipate and become undetectable again.

S2
During the course of this campaign the measured flux density of S2 varied by a factor of six between ~ 40 and $\sim 230\,\mu$Jy (Figure 6.8). Knapp et al. (1996) report a flux density of $230 \pm 40\,\mu$Jy at 8.4 GHz and estimate a 5σ upper limit of $150\,\mu$Jy at 4.9 GHz from archival data of Machin et al. (1990). This is indicative of a compact flat spectrum source variable on the timescale of a few months, most likely an LMXB. To our knowledge, however, there are no known X-ray sources within ~ 1 arcmin to the coordinates of S2.

6.4.6 Constraints on the IMBH mass in M15

In chapter 5 we reported a 3σ upper mass limit for the putative IMBH in M15 of $M_\bullet \leq 500\,\mathrm{M}_\odot$. This work was based on the first five of the observations discussed here. In epochs 6 and 7 we also do not detect any significant emission within a radius of 0.6 arcsec (corresponding to a 3σ uncertainty) of the cluster core position at coordinates (J2000) RA $= 21^\mathrm{h}29^\mathrm{s}58\overset{\mathrm{s}}{.}330 \pm 0\overset{\mathrm{s}}{.}013$, Dec $= 12^\circ 10' 01\overset{''}{.}2 \pm 0\overset{''}{.}2$ (Goldsbury et al., 2010). If we concatenate the data of all seven epochs the resulting noise level improves only slightly compared to concatenating the first five epochs only (rms $\sim 3.3\,\mu$Jy/beam). Based on the fundamental plane of black hole activity (Merloni et al., 2003; Falcke et al., 2004; Körding et al., 2006)

$$\log M_\bullet = 1.55 \log L_R - 0.98 \log L_X - 9.95$$

which relates black hole mass, $M_\bullet$; radio luminosity, L_R; and X-ray luminosity, L_X. We therefore reconfirm the upper mass limit for the putative IMBH of $M_\bullet \leq 500\,\mathrm{M}_\odot$. Furthermore, our data excludes variability of any compact object residing at the center of M15 on the timescale of two months to two years.

6.5 Conclusions

We observed the massive globular cluster M15 in a multi-epoch global VLBI campaign in seven observations covering a time span of two years. In our observations

we clearly detect five compact radio sources, namely the pulsar M15A, the double neutron star system M15C, the LMXB AC211, and two unclassified sources S1 and S2. Except for M15C (which was only detected in epochs 1, 3, and 7), all sources were detected in all seven epochs. From our proper motion measurements (Table 6.3) and the variability of M15C, AC211, and S2 we conclude:

- The projected global proper motion of M15 is $(\mu_\alpha,\ \mu_\delta) = (-0.58\pm0.18,\ -4.05\pm 0.34)\,\mathrm{mas\,yr^{-1}}$,
- M15A and AC211 have a maximal transverse peculiar velocity $v_{trans}^{max} = 66\,\mathrm{km\,s^{-1}}$ within the cluster,
- In epoch 3, the morphology of the LMXB AC211 is not point like but shows a double lobed structure instead. It is quite likely that the source had an outburst shortly before the observations in epoch 3,
- M15C has a transverse velocity of at most $39\,\mathrm{km\,s^{-1}}$ moving towards the north in the cluster,
- The observed 2.5% phase shift in the pulse profile points to geodetic precession as a possible explanation for the disappearance and reappearance of M15C during the observations,
- S1 is of extragalactic origin, most probably a background quasar,
- S2 is a Galactic foreground source at a distance $d = 2.2^{+0.5}_{-0.3}\,\mathrm{kpc}$ moving at a transverse velocity $v_t^{\mathrm{S2}} = 26^{+5}_{-4}\,\mathrm{km\,s^{-1}}$ with respect to the LSR,
- The flux density of S2 is variable by a factor of a few on the time scale of a few months. The spectrum seems to be flat indicative of a LMXB. There is, however, no known X-ray source within about 1 arcmin of the radio position of the source.

The proper motions measured here will be important for the analysis of the timing data from M15A and M15C (Ridolfi et al., in preparation). Our model-independent measurement of the proper motion of the pulsar M15A will allow a much less ambiguous interpretation of the variation of the acceleration of this pulsar in the cluster potential. Equally, in the case of M15C, with timing only the glitch signal will be entangled with the proper motion signal. Our measurement of the proper motion will allow an unambiguous study of the rotational behavior of the pulsar.
Similar to the first five observations (chapter 5), in epochs 6 and 7 we do not detect any significant emission from a putative IMBH within the central 0.6 arcsec of the

core region of M15. Excluding any variability of a central object on the time scale of two months to two years, we reconfirm the 3σ upper limit for the proposed central IMBH mass of $M_\bullet = 500\,M_\odot$.

References

Anderson, S. B. 1993, PhD thesis, California Institute of Technology
Anderson, S. B., Gorham, P. W., Kulkarni, S. R., Prince, T. A., & Wolszczan, A. 1990, Nature, 346, 42
Antoniadis, J., Freire, P. C. C., Wex, N., et al. 2013, Science, 340, 448
Auriere, M., Le Fevre, O., & Terzan, A. 1984, A&A, 138, 415
Bagchi, M. 2013, International Journal of Modern Physics D, 22, 30021
Bagchi, M. & Lorimer, D. R. 2011, in American Institute of Physics Conference Series, Vol. 1357, American Institute of Physics Conference Series, ed. M. Burgay, N. D'Amico, P. Esposito, A. Pellizzoni, & A. Possenti, 173–176
Bates, S. D., Lorimer, D. R., & Verbiest, J. P. W. 2013, MNRAS, 431, 1352
Baumgardt, H., Hut, P., Makino, J., McMillan, S., & Portegies Zwart, S. 2003, ApJL, 582, L21
Bevington, P. R. 1969, Data reduction and error analysis for the physical sciences
Bhattacharya, D. & van den Heuvel, E. P. J. 1991, Physics Reports, 203, 1
Chatterjee, S., Brisken, W. F., Vlemmings, W. H. T., et al. 2009, ApJ, 698, 250
Chatterjee, S., Cordes, J. M., Vlemmings, W. H. T., et al. 2004, ApJ, 604, 339
Cudworth, K. M. & Hanson, R. B. 1993, AJ, 105, 168
Falcke, H., Körding, E., & Markoff, S. 2004, A&A, 414, 895
Feast, M. & Whitelock, P. 1997, MNRAS, 291, 683
Fender, R. P., Garrington, S. T., McKay, D. J., et al. 1999, MNRAS, 304, 865
Freire, P. C. C., Wex, N., Esposito-Farèse, G., et al. 2012, MNRAS, 423, 3328
Geffert, M., Colin, J., Le Campion, J.-F., & Odenkirchen, M. 1993, AJ, 106, 168
Gerssen, J., van der Marel, R. P., Gebhardt, K., et al. 2003, AJ, 125, 376
Giacconi, R., Murray, S., Gursky, H., et al. 1974, ApJS, 27, 37
Goldsbury, R., Richer, H. B., Anderson, J., et al. 2010, AJ, 140, 1830
Hessels, J. W. T., Ransom, S. M., Stairs, I. H., Kaspi, V. M., & Freire, P. C. C. 2007, ApJ, 670, 363
Jacoby, B. A., Cameron, P. B., Jenet, F. A., et al. 2006, ApJL, 644, L113
Johnston, H. M., Kulkarni, S. R., & Goss, W. M. 1991, ApJL, 382, L89
Kettenis, M., van Langevelde, H. J., Reynolds, C., & Cotton, B. 2006, in Astronomical Society of the Pacific Conference Series, Vol. 351, Astronomical Data Analysis Software and Systems XV, ed. C. Gabriel, C. Arviset, D. Ponz, & S. Enrique, 497
Kirsten, F. & Vlemmings, W. H. T. 2012, A&A, 542, A44
Knapp, G. R., Gunn, J. E., Bowers, P. F., & Vasquez Poritz, J. F. 1996, ApJ, 462, 231
Körding, E., Falcke, H., & Corbel, S. 2006, A&A, 456, 439
Lorimer, D. R. & Kramer, M. 2005, Cambridge University Press
Machin, G., Lehto, H. J., McHardy, I. M., Callanan, P. J., & Charles, P. A. 1990, MNRAS, 246, 237
Manchester, R. N., Hobbs, G. B., Teoh, A., & Hobbs, M. 2005, AJ, 129, 1993
Maron, O., Kijak, J., Kramer, M., & Wielebinski, R. 2000, A&AS, 147, 195
Matsuoka, M., Kawasaki, K., Ueno, S., et al. 2009, PASJ, 61, 999
McNamara, B. J., Harrison, T. E., & Anderson, J. 2003, ApJ, 595, 187
McNamara, B. J., Harrison, T. E., & Baumgardt, H. 2004, ApJ, 602, 264

Merloni, A., Heinz, S., & di Matteo, T. 2003, MNRAS, 345, 1057
Morgan, J. S., Mantovani, F., Deller, A. T., et al. 2011, A&A, 526, A140
Murphy, B. W., Cohn, H. N., & Lugger, P. M. 2011, ApJ, 732, 67
Newell, B., Da Costa, G. S., & Norris, J. 1976, ApJL, 208, L55
Odenkirchen, M., Brosche, P., Geffert, M., & Tucholke, H.-J. 1997, New Astronomy, 2, 477
Offringa, A. R., de Bruyn, A. G., Biehl, M., et al. 2010, MNRAS, 405, 155
Offringa, A. R., van de Gronde, J. J., & Roerdink, J. B. T. M. 2012, A&A, 539, A95
Phinney, E. S. 1993, in Astronomical Society of the Pacific Conference Series, Vol. 50, Structure and Dynamics of Globular Clusters, ed. S. G. Djorgovski & G. Meylan, 141
Schilizzi, R. T., Aldrich, W., Anderson, B., et al. 2001, Experimental Astronomy, 12, 49
Scholz, R.-D., Odenkirchen, M., Hirte, S., et al. 1996, MNRAS, 278, 251
Schönrich, R. 2012, MNRAS, 427, 274
Sneden, C., Kraft, R. P., Shetrone, M. D., et al. 1997, AJ, 114, 1964
Stirling, A. M., Jowett, F. H., Spencer, R. E., et al. 2002, MNRAS, 337, 657
Stuart, A. & Ord, J. K. 1994, Kendall's advanced theory of statistics. Vol.1: Distribution theory
Sun, X.-H., Han, J.-L., & Qiao, G.-J. 2002, ChJAA, 2, 133
Tauris, T. M. & van den Heuvel, E. P. J. 2006, Formation and evolution of compact stellar X-ray sources, ed. W. H. G. Lewin & M. van der Klis, 623–665
van den Bosch, R., de Zeeuw, T., Gebhardt, K., Noyola, E., & van de Ven, G. 2006, ApJ, 641, 852
White, N. E. & Angelini, L. 2001, ApJL, 561, L101
Wolszczan, A., Kulkarni, S. R., Middleditch, J., et al. 1989, Nature, 337, 531

7 Revisiting the birth locations of pulsars B1929+10, B2020+28, and B2021+51

Franz Kirsten, Wouter Vlemmings, Robert M. Campbell, Michael Kramer and Shami Chatterjee, to be submitted for publication in A&A

Abstract We present new proper motion and parallax measurements obtained with the European VLBI Network (EVN) at C-band for the three isolated pulsars B1929+10, B2020+28 and B2021+51. For B1929+10 we combine our data with earlier VLBI measurements and improve the accuracy of the astrometric parameters of this pulsar by a factor of five. In the case of the pulsars B2020+28 and B2021+51 our observations indicate that both stars are almost a factor of two closer to the Solar System than previously thought, placing them at a distance of $1.39^{+0.05}_{-0.06}$ and $1.25^{+0.14}_{-0.17}$ kpc, respectively. Using our new astrometry we simulate all three pulsars' orbits in the Galactic potential aiming to confirm or reject previously proposed birth locations. Our observations ultimately rule out a claimed binary origin of B1929+10 and the runaway-star ζ Ophiuchi in Upper Scorpius. A putative common binary origin of B2020+28 and B2021+51 in the Cygnus Superbubble is also very unlikely.

7.1 Introduction

Typical transverse velocities of isolated pulsars are on the order of several hundred $\mathrm{km\,s^{-1}}$ (Cordes & Chernoff, 1998; Arzoumanian et al., 2002; Hobbs et al., 2005) while those of their progenitor O- and B-stars are at most several tens of $\mathrm{km\,s^{-1}}$. In the standard neutron star formation scenario this discrepancy is explained via an asymmetry in the supernova (SN) explosion that imparts a kick on the forming central compact object accelerating it to the observed velocities (e.g. Scheck et al., 2006). Due to the short life time of SN-remnants ($< 10^5$ yr) and the typical characteristic age of young pulsars ($\tau_c \sim 10^{6-7}$ Myr), direct associations between SN-remnants and

pulsars are rare, making the observational confirmation of this formation scenario difficult. Measurements of accurate proper motions μ and parallaxes π of pulsars can, however, indicate the birth locations of pulsars. The combination of both μ and the distance $d = 1/\pi$ yields the physical transverse velocity, $V_\perp$, which, given an estimate of the radial velocity, V_r, allows the calculation of a trajectory tracing the pulsar back to its possible birth location. Hence, kinematic ages – as opposed to characteristic ages $\tau_c = P/2\dot{P}$ – of pulsars can be determined and conclusions about neutron star formation scenarios can be drawn.

One of the first to calculate pulsar orbits was Wright (1979), claiming that the pulsars B1929+10 (J1932+1059) and B1952+29 originate from a former binary system. More recently, Hoogerwerf et al. (2001) used the 3D–space velocity of high-velocity runaway stars and parallax and proper motion measurements of young nearby pulsars to simulate their trajectories back in time. Their simulations indicate that the runaway O-star ζ Ophiuchi (ζ Oph, HIP 81377) and the young pulsar B1929+10 are likely to have formed a binary system in Upper Scorpius (Scorpius-Centaurus association) until about 1 Myr ago. According to their analysis, the system was disrupted when the star that is now observed as pulsar B1929+10 went supernova. During that event both ζ Oph and the pulsar received a kick driving both away from Upper Scorpius. The parameter range for which such a scenario is possible is, however, rather small. Improved measurements of μ and π for B1929+10 obtained with the NRAO Very Long Baseline Array (VLBA) led to the conclusion that a common origin of the pulsar and ζ Oph is unlikely (Chatterjee et al., 2004). Adopting the measurements of Chatterjee et al. (2004) but increasing the reported uncertainties by factors between 10 and 30, Bobylev (2008) and also Tetzlaff et al. (2010) repeated the simulations of Hoogerwerf et al. (2001), re-postulating a binary origin of B1929+10 and ζ Oph in Upper Scorpius .

In a similar experiment, Vlemmings et al. (2004) identify the two pulsars B2020+28 and B2021+51 as candidates for a common origin scenario based on proper motion and parallax measurements obtained with the VLBA at 1.4 GHz (Brisken et al., 2002). The authors simulate the trajectories of both pulsars back in time and conclude that they are likely to originate from a binary system in the Cygnus Superbubble that was disrupted when the younger of both pulsars was born in a supernova. The measurements by Brisken et al. (2002) are, however, based on five observations covering a time span of roughly one year only.

Here, we present new measurements of μ and π for the three pulsars B1929+10, B2020+28, and B2021+51 obtained with the European VLBI Network (EVN) at an observing frequency of 5 GHz. This data extends the time baseline to more than

Table 7.1: Calibrator details for each pulsar.

Source	Pointing center Ra	Dec	Distance to Pulsar [deg]	Flux density [mJy beam^{-1}]
B1929+10	19:32:14.0160	10:59:32.868		50[(b)]
J1928+0848[(a)]	19:28:40.8555	08:48:48.413	2.35	160
J1934+1043	19:34:35.0256	10:43:40.366	0.63	50
B2020+28	20:22:37.0697	28:54:22.976		30[(b)]
J2020+2826[(a)]	20:20:45.8707	28:26:59.195	0.61	70
J2023+3153	20:23:19.0173	31:53:02.306	2.98	900
B2021+51	20:22:49.8596	51:54:50.400		80[(b)]
J2025+5028[(a)]	20:25:24.9725	50:28:39.536	1.49	110
J2023+5427	20:23:55.8440	54:27:35.829	2.55	500

Notes. [(a)]These are the calibrators referred to as primary calibrators in the text. [(b)]Pulsar fluxes obtained from pulsar gating.

ten years allowing for an unprecedented precision of μ and π for all three pulsars. We use this data to repeat the simulations of trajectories in order to shed new light on the proposed binary origin of B1929+10/ ζ Oph and B2020+28/ B2021+51.

7.2 Observations and data reduction

The observations described here were conducted with the full EVN under project code EV018 (A-D). We observed all three target pulsars at C-band (6cm) in left and right circular polarization. Each of the eight intermediate frequencies (IFs) have a bandwidth of 16MHz and are split into 32 individual channels. The data was correlated with an integration time of one second using the EVN software correlator (SFXC[1], Keimpema 2014, in preparation) at the Joint Institute for VLBI in Europe (JIVE). The scans of the individual pulsars were correlated employing a 2-bit pulsar gate where only the times when the pulsar is 'on' are used for correlation. In this way, the signal-to-noise ratio (S/N) of the pulsar detections can be increased by the factor $\sqrt{P/w} \sim 5$, where P and w are the pulse period and pulse width, respectively. Each pulsars' ephemeris required for determining the 'on'-times was determined using the software package TEMPO2[2] (Hobbs et al., 2006). Typical gate widths were on the order of $5 - 10\%$ of the pulse period.

In total we observed each pulsar four times between May 2010 and June 2011 at

[1]http://www.jive.nl/jivewiki/doku.php?id=sfxc
[2]`http://www.atnf.csiro.au/research/pulsar/tempo2/`

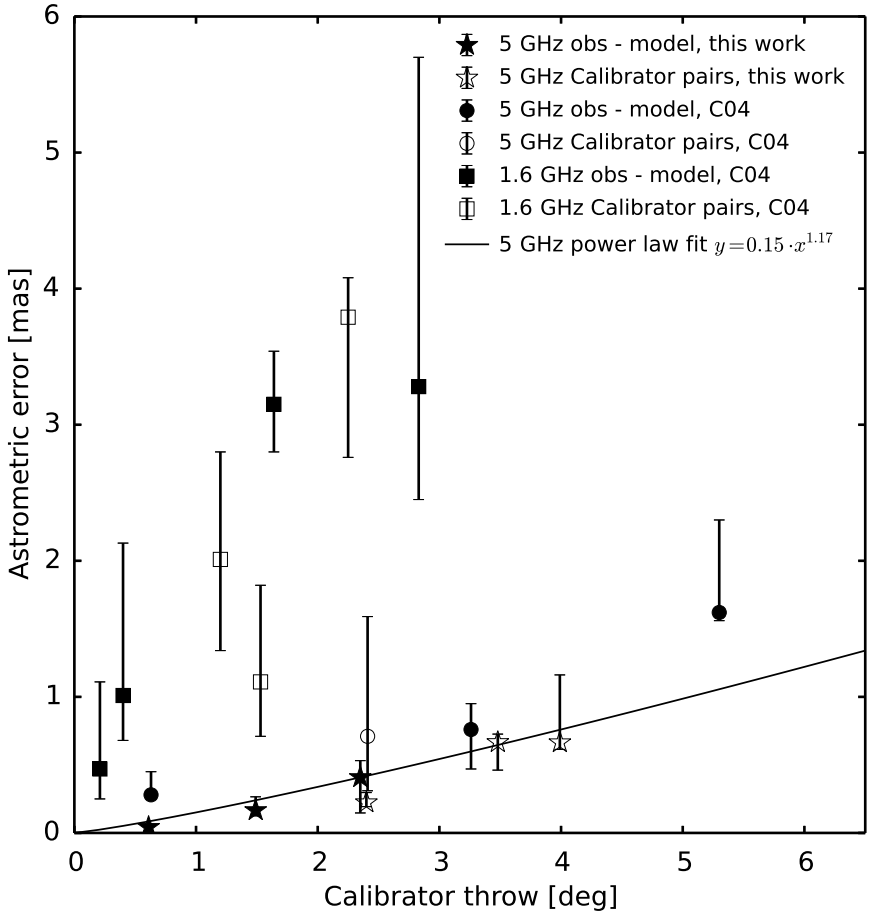

Fig. 7.1: Astrometric accuracy as a function of angular separation between phase calibrator source and target. This is a reproduction of Figure 3 in Chatterjee et al. (2004) (referred to as C04 here) where we added data from our observations (open and filled stars). Open symbols denote the median scatter about the average position of the primary phase calibrator obtained from calibrating its visibilities with solutions from the secondary calibrator. Filled symbols show the median scatter of the observed positions about the best fit model for proper motion and parallax. The 1.6 GHz data (squares) are from Chatterjee et al. (2001) and Vlemmings et al. (2003) while the previous 5 GHz data are from Chatterjee et al. (2004). The solid line is a weighted least squares power law fit ($y = a \cdot x^b$) to all 5 GHz data points where the parameters (a, b) = (0.15 ± 0.09, 1.17 ± 0.31). Clearly, the almost linear relationship between astrometric error and calibrator throw brakes down beyond an angular separation of more than about four degrees.

intervals of four to five months. Each observing run spans a time range of twelve hours spending roughly four hours on each pulsar and corresponding calibrators (Table 7.1). In each case the observations were scheduled such that the target pulsar and the primary calibrator were observed in an alternating fashion for 2.5 min and 1.5 min, respectively. After each second scan of the primary calibrator, the

secondary calibrator was observed (also for 1.5 min) before switching back to the pulsar. For bandpass calibration purposes we observed the quasars J1800+3848 and 3C454.3 two hours and eight hours after the start of the observations, respectively.

We performed a mostly automated data reduction and calibration procedure relying on the NRAO Astronomical Image Processing System (AIPS) and the scripting language ParselTongue (Kettenis et al., 2006). Removal of data affected by radio frequency interference (RFI) was performed running the RFI-mitigation software SERPent (Peck & Fenech, 2013) and some further manual flagging. We first apply the system temperature and gain curve corrections as determined by the EVN pipeline[3] and also correct for the the parallactic angle using the AIPS task CLCOR. Next we compute ionospheric corrections in TECOR with the help of total electron content maps as published by the Center for Orbit Determination in Europe[4]. In a first calibration run we solve for visibility rates, phases, and delays in FRING for all calibrator sources assuming a simple point source model. Following, we self-calibrate on each source improving the S/N by a factor of five to ten. For each calibrator we then concatenate the calibrated data from all four epochs. This dataset is imaged to produce a global model of each calibrator source. The dominating CLEAN components of each source model are then used as the input model parameters in a second FRING-run. In this way, any systematics affecting the position of the calibrator sources in between epochs were eliminated. For each of the three pulsars the calibration solutions of the primary calibrator were of much higher quality and, hence, were applied to the respective target pulsar (Table 7.1).

We use the calibration solutions from the secondary calibrator to add to the analysis of astrometric accuracy in dependence on angular separation between target and calibrator source ('calibrator throw') done by Chatterjee et al. (2004). Similarly to the earlier data, our observations imply an almost linear increase in astrometric accuracy with decreasing calibrator throw (Figure 7.1). We fit a power law, $y = a \cdot x^b$, to all data points obtained from 5 GHz observations which yields $(a,\, b) = (0.15 \pm 0.09,\, 1.17 \pm 0.31)$. This relation, however, seems to only hold for angular separations of up to four degrees between calibrator and target.

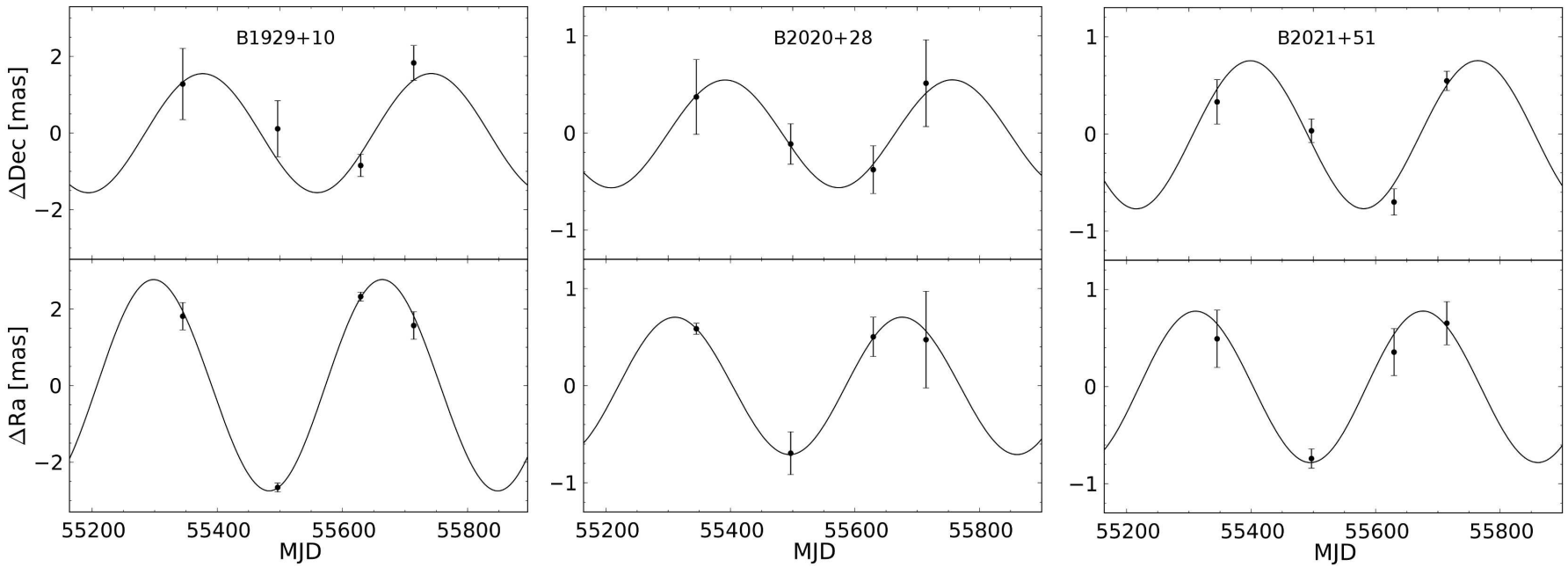

Fig. 7.2: Relative measured positions of B1929+10 (left), B2020+28 (middle), and B2021+51 (right) with the best fit proper motion removed. The solid line is the best fit parallax from our EVN C-band observations.

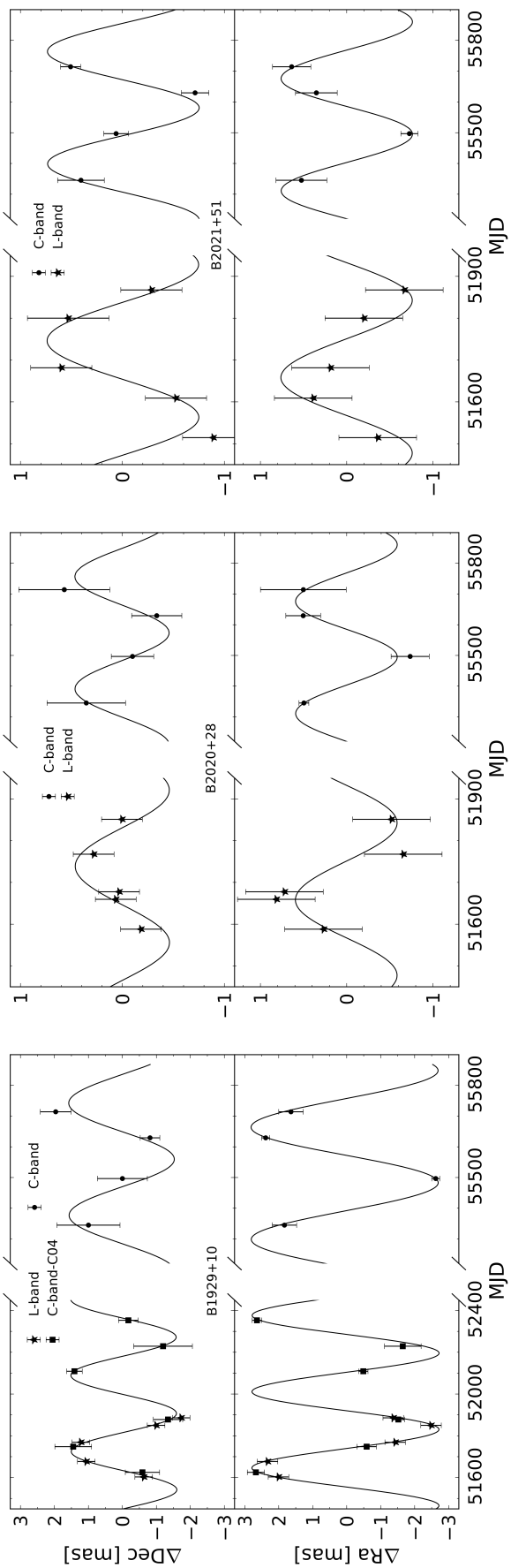

Fig. 7.3: Same as Figure 7.2 but for the fits performed using all available data. Solid dots show the most recent measurements at C-band, stars are the data from Brisken et al. (2002), and squares are the data from Chatterjee et al. (2004). For better illustration the time span without any observations is cut out.

Table 7.2: Measured positions at MJD 55630.

	Ra (J2000)	Dec (J2000)	S/N	beam size [mas×mas]
B1929+10	19:32:14.021289(1)	10:59:32.90137(5)	155	1.01×5.94
B2020+28	20:22:37.06758(1)	28:54:22.7563(2)	142	3.76×7.36
B2021+51	20:22:49.85890(1)	51:54:50.5005(1)	156	1.72×3.97

Notes. Numbers in brackets indicate the uncertainty in the last digit.

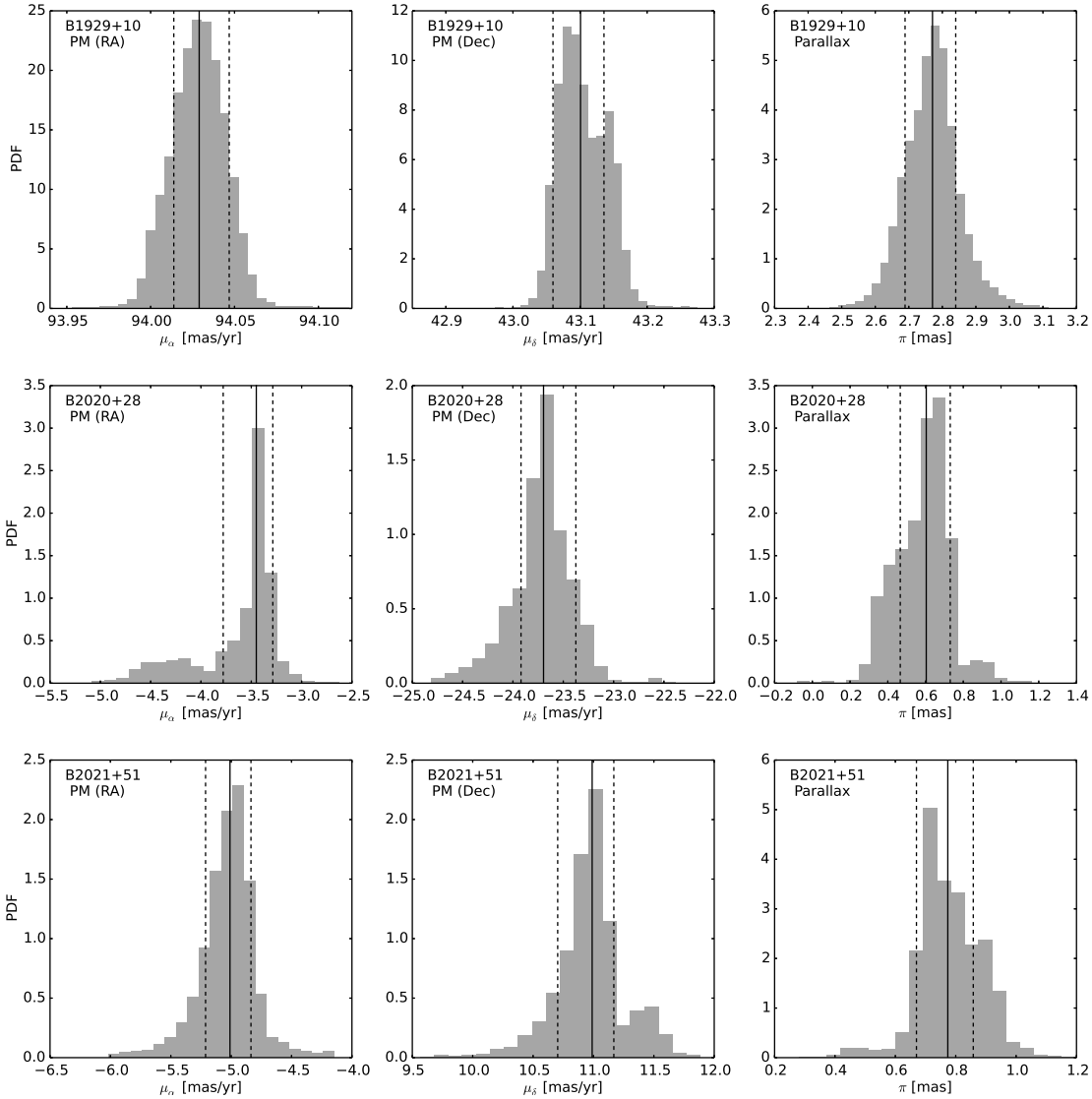

Fig. 7.4: Probability density functions of fitting results from bootstrapping all available data. From top to bottom: B1929+10, B2020+28, B2021+51. Columns are from left to right: proper motion in Ra, proper motion in Dec, parallax. The solid and the dashed vertical lines indicate the median and the most compact 68% confidence intervals as listed in Table 7.4, respectively.

Table 7.3: Previous proper motion and parallax estimates and derived values.

	μ_α [mas yr^{-1}]	μ_δ [mas yr^{-1}]	π [mas]	d [kpc]	$V_\perp$ [km s^{-1}]	References
B1929+10	99.0 ± 12.0	39.0 ± 8.0	4.00 ± 2.0	$0.24^{+0.09}_{-0.12}$	124^{+140}_{-52}	Hoogerwerf et al. (2001)
B1929+10	94.82 ± 0.26	43.04 ± 0.15	3.02 ± 0.09	$0.33^{+0.01}_{-0.01}$	162^{+6}_{-5}	L-band, Brisken et al. (2002)
B1929+10	94.09 ± 0.11	42.99 ± 0.16	2.77 ± 0.07	$0.361^{+0.009}_{-0.009}$	176^{+5}_{-5}	L-/C-band, Chatterjee et al. (2004)
B2020+28	-4.38 ± 0.53	-23.59 ± 0.26	0.37 ± 0.12	$2.70^{+0.64}_{-0.96}$	256^{+135}_{-62}	L-band, Brisken et al. (2002)
B2021+51	-5.23 ± 0.17	11.54 ± 0.28	0.50 ± 0.07	$2.00^{+0.23}_{-0.31}$	149^{+28}_{-22}	L-band, Brisken et al. (2002)

Table 7.4: Astrometric results and derived values from the estimation strategies.

	data sets(*)	number of data points	μ_α [mas yr^{-1}]	μ_δ [mas yr^{-1}]	π [mas]	$\chi^2_{\rm red}$	d [kpc]	$V_\perp$ [km s^{-1}]
B1929+10	C$^{(f)}$	4	94.11 ± 0.52	43.64 ± 1.06	2.79 ± 0.14	1.34	$0.358^{+0.017}_{-0.019}$	175^{+11}_{-10}
	C$_C$, C$^{(f)}$	10	94.04 ± 0.12	43.39 ± 0.23	2.79 ± 0.08	1.03	$0.358^{+0.010}_{-0.010}$	175^{+5}_{-5}
	L, C$^{(f)}$	9	94.20 ± 0.20	42.93 ± 0.26	2.78 ± 0.05	0.51	$0.360^{+0.006}_{-0.006}$	175^{+4}_{-3}
	L, C$_C$, C$^{(f)}$	15	94.06 ± 0.09	43.24 ± 0.17	2.78 ± 0.06	0.77	$0.360^{+0.007}_{-0.008}$	176^{+4}_{-5}
	C$_C$, C$^{(b)}$	10	$94.07^{+0.14}_{-0.20}$	$43.41^{+0.10}_{-0.12}$	$2.76^{+0.10}_{-0.14}$		$0.362^{+0.019}_{-0.012}$	177^{+7}_{-7}
	L, C$^{(b)}$	9	$94.23^{+0.14}_{-0.24}$	$42.95^{+0.23}_{-0.26}$	$2.79^{+0.07}_{-0.12}$		$0.362^{+0.019}_{-0.012}$	175^{+8}_{-5}
	L, C$_C$, C$^{(b)}$	15	$94.03^{+0.02}_{-0.02}$	$43.10^{+0.03}_{-0.04}$	$2.77^{+0.07}_{-0.08}$		$0.361^{+0.011}_{-0.009}$	176^{+6}_{-4}
B2020+28	C$^{(f)}$	4	-3.34 ± 0.05	-23.65 ± 0.11	0.72 ± 0.03	0.05	$1.39^{+0.05}_{-0.06}$	134^{+6}_{-6}
	L, C$^{(f)}$	9	-3.46 ± 0.17	-23.73 ± 0.21	0.61 ± 0.08	0.53	$1.63^{+0.18}_{-0.23}$	158^{+25}_{-20}
	L, C$^{(b)}$	9	$-3.45^{+0.16}_{-0.33}$	$-23.70^{+0.32}_{-0.22}$	$0.60^{+0.13}_{-0.14}$		$1.66^{+0.50}_{-0.29}$	160^{+50}_{-30}
B2021+51	C$^{(f)}$	4	-5.08 ± 0.42	10.84 ± 0.25	0.80 ± 0.11	1.54	$1.25^{+0.14}_{-0.17}$	87^{+15}_{-12}
	L, C$^{(f)}$	9	-5.03 ± 0.27	10.96 ± 0.17	0.78 ± 0.07	0.90	$1.28^{+0.10}_{-0.12}$	90^{+11}_{-9}
	L, C$^{(b)}$	9	$-5.01^{+0.17}_{-0.20}$	$10.99^{+0.18}_{-0.29}$	$0.77^{+0.08}_{-0.10}$		$1.30^{+0.19}_{-0.13}$	91^{+16}_{-12}

Notes. (*) C refers to the measurements obtained in this campaign, C$_C$ denotes the data set from Chatterjee et al. (2004), and L indicates that the measurements from Brisken et al. (2002) were included in the analysis.(f)Results derived from a least-squares fit of the measured data. (b)Median values and 68% confidence interval from fitting bootstrapped realizations of the data.

7.3 Estimates for astrometric parameters of B1929+10, B2020+28, and B2021+51

We measure the position of the pulsars in each epoch by fitting a 2D-Gaussian to the brightness distribution in the image plane using the AIPS task IMFIT. Due to the high S/N (~ 150) and small beam size ($\theta \sim 3 \times 5\,\mathrm{mas}$) the formal errors are very small ($\theta/(2 * \mathrm{S/N}) \sim 6 \times 30\,\mu\mathrm{as}$), certainly underestimating the real positional uncertainties. In addition to these random errors, residual systematic errors caused by, e.g. the calibrator throw (Figure 7.1), need to be taken into account. A good estimate for these systematic errors is the deconvolved size θ_d of the pulsar, which is zero for a true point source. Following the scheme in Chatterjee et al. (2001) we estimate the systematic uncertainties using the quantity $\theta_\mathrm{d}/\sqrt{(N_\mathrm{ant}-1) * t_\mathrm{obs}/t_\mathrm{iono}}$, where $N_\mathrm{ant} = 11$ is the typical number of antennas involved, $t_\mathrm{obs} = 110\,\mathrm{min}$ is the total amount of time spent on each pulsar, and $t_\mathrm{iono} = 6\,\mathrm{min}$ is the empirically determined atmospheric coherence time at C-band. For the total positional uncertainty we add both the formal and the systematic errors in quadrature. Table 7.2 lists the measured positions of all three pulsars in the third epoch at MJD 55630.

To estimate each pulsar's proper motion and parallax we perform a weighted least-squares-fit to the measured positions. Here, we measure both parameters in three ways: we consider our position measurements only (Figure 7.2), we combine our data with that of the publications listed in Table 7.3 (Figure 7.3), and we employ a bootstrapping technique. For the latter, as many position measurements as are available for a given pulsar are sampled randomly. These positions are then fitted and the results are stored. This procedure is repeated 10^5 times yielding distributions as shown in Figure 7.4. During the fitting procedure we allow for absolute positional offsets between the different data sets (typically on the order of several mas). Such offsets are expected for several reasons: i) the data were obtained at times that are up to ten years apart during which improvements to the correlator models and Earth position parameters introduce offsets; ii) the data were taken with different instruments (VLBA and EVN) that use different hardware/software correlators; iii) the observations were conducted at different frequencies; and iv) the different campaigns used different calibrator sources. The estimates for μ and π from the individual fits, the different combinations of data sets and also from the bootstrapping method (we state the most compact 68% confidence interval), along

[3] http://www.evlbi.org/pipeline/user_expts.html
[4] ftp://ftp.unibe.ch/aiub/CODE/

with the implied pulsar distances and transverse velocities are summarized in Table 7.4. The latter are corrected for Solar motion and differential galactic rotation and refer to the local standard of rest (LSR). Regardless of estimation strategy and combination of available data, all measured values agree within one sigma.

For pulsar B1929+10 our results confirm the measurements of Chatterjee et al. (2004) and in combination with the earlier data we reduce the uncertainties by a factor of about five. For pulsars B2020+28 and B2021+51 our observations indicate that they are about 1.1 and 0.7 kpc, respectively, closer to the Solar System than what was implied by the measurements of Brisken et al. (2002) alone (Table 7.3). Considering this discrepancy of a factor of about 2 we suspect that the uncertainties on the position measurements for B2020+28 and B2021+51 as reported by the authors were underestimated. Accordingly, we will not include this data in the further analysis. Thus, in the following, for B1929+10 we adopt the astrometric parameters obtained from bootstrapping all available data, while for B2020+28 and B2021+51 we use the parameters as measured with our new C-band data alone. Hence, below, the analysis is based on the following proper motion and parallax measurements: $(\mu_\alpha,\, \mu_\delta,\, \pi) = (94.03^{+0.02}_{-0.02}\,\mathrm{mas\,yr^{-1}},\, 43.10^{+0.03}_{-0.04}\,\mathrm{mas\,yr^{-1}},\, 2.77^{+0.07}_{-0.08}\,\mathrm{mas})$ for B1929+10, $(\mu_\alpha,\ \mu_\delta,\ \pi) = (-3.34 \pm 0.05\,\mathrm{mas\,yr^{-1}},\ -23.65 \pm 0.11\,\mathrm{mas\,yr^{-1}},\ 0.72 \pm 0.03\,\mathrm{mas})$ for B2020+28, and $(\mu_\alpha,\ \mu_\delta,\ \pi) = (-5.08 \pm 0.42\,\mathrm{mas\,yr^{-1}},\ 10.84 \pm 0.25\,\mathrm{mas\,yr^{-1}},\ 0.80 \pm 0.11\,\mathrm{mas})$ for B2021+51.

7.4 Simulations of pulsar orbits

In order to shed new light on possible common origins of B1929+10/ ζ Oph and B2020+28/ B2021+51 we use the pulsar astrometric parameters described above and trace their orbits back in time through the Galactic potential. For the runaway-star ζ Oph we use the latest proper motion and parallax measurements $(\mu_\alpha,\, \mu_\delta) = (15.26 \pm 0.26,\, 24.79 \pm 0.22)\,\mathrm{mas\,yr^{-1}}$, $\pi = 8.91 \pm 0.20\,\mathrm{mas}$ (van Leeuwen, 2007) and we adopt the value for the radial velocity $V_{\mathrm{rad}} = -9.0 \pm 5.5\,\mathrm{km\,s^{-1}}$ from Kharchenko et al. (2007). Our astrometric measurements yield information about the transverse motion of the pulsars but they do not contain any information about the radial velocity. In order to have an estimate of the full 3D-velocity vector we simulate the radial component from our measured transverse components and the space velocity distribution of young pulsars as empirically derived by Hobbs et al. (2005). To account for the uncertainties of the measured parameters μ_α, μ_δ, π, and also the unknown radial velocity we assume that all parameters are distributed normally (where the half-width of the Gaussian is given by the larger absolute value of the

upper and lower errors of the bootstrapping results) and perform 3 million Monte Carlo simulations. The obtained velocity vectors are corrected for the Solar motion with respect to the LSR, for differential Galactic rotation and also for the velocity of the LSR. The Galactic potential we use in our simulations is the one that was described in full detail in Vlemmings et al. (2004), the main parameters of which we summarize here in brief. The pulsar orbits are traced back through a Stäckel potential consisting of a thin disk, a thick disk, and a halo component whose axis ratios $\epsilon = 75.0$, 1.5, and 1.02. We keep the relative contributions of thin and thick disk and of the halo at $k = 0.13$, 0.01, and 1.0, respectively. The Solar parameters we use, $(R_\odot, U, V, W) = (8.27\,\mathrm{kpc}, -13.84\,\mathrm{km\,s^{-1}}, 12.24\,\mathrm{km\,s^{-1}}, 6.1\,\mathrm{km\,s^{-1}})$, are adopted from Schönrich (2012) . Each object's trajectory is sampled at time intervals of 10^3 yr using a fourth-order Runge-Kutta numerical integration method. For each time step the distances between the two objects under consideration are computed within the Galactic reference frame and only the simulation input parameters of trajectories that result in a minimum distance of less than 10 pc are recorded. In addition to the separation between the individual objects, we also compute their distances to the Sun (B2020+28/ B2021+51) and to the Upper Scorpius region (B1929+10/ ζ Oph). To compute the latter we trace the trajectory of Upper Scorpius back in time using the astrometric values as listed in Table 2 of de Zeeuw et al. (1999).

For consistency checks we use the input parameters of Hoogerwerf et al. (2001) to compute the trajectories of B1929+10 and ζ Oph. In total, 37521 (= 1.2%, compared to 30822 (1.0%) in Hoogerwerf et al. (2001)) out of the 3 million sampled trajectories cross within 10 pc. The smallest separation we find is 0.19 pc (compared to 0.35 pc). While Hoogerwerf et al. (2001) report that in 4214 (0.14%) simulations both the pulsar and the runaway-star not only come closer than 10 pc but are also within less than 10 pc of Upper Scorpius, we find that 6816 (0.23%) of our simulations fulfill this requirement. The differences in the results are probably due to the different set-ups of the Galactic potentials. We do, however, reproduce the general trend found by Hoogerwerf et al. (2001). If we run the simulations using the same input parameters for B1929+10 as Hoogerwerf et al. (2001) but use the latest parameters for ζ Oph from van Leeuwen (2007), a total of 82840 (2.7%) simulated orbits cross within 10 pc, in only 8 of which both the pulsar and the star are less than 10 pc away from Upper Scorpius.

To test how much the updated Solar parameters and the different radial velocity

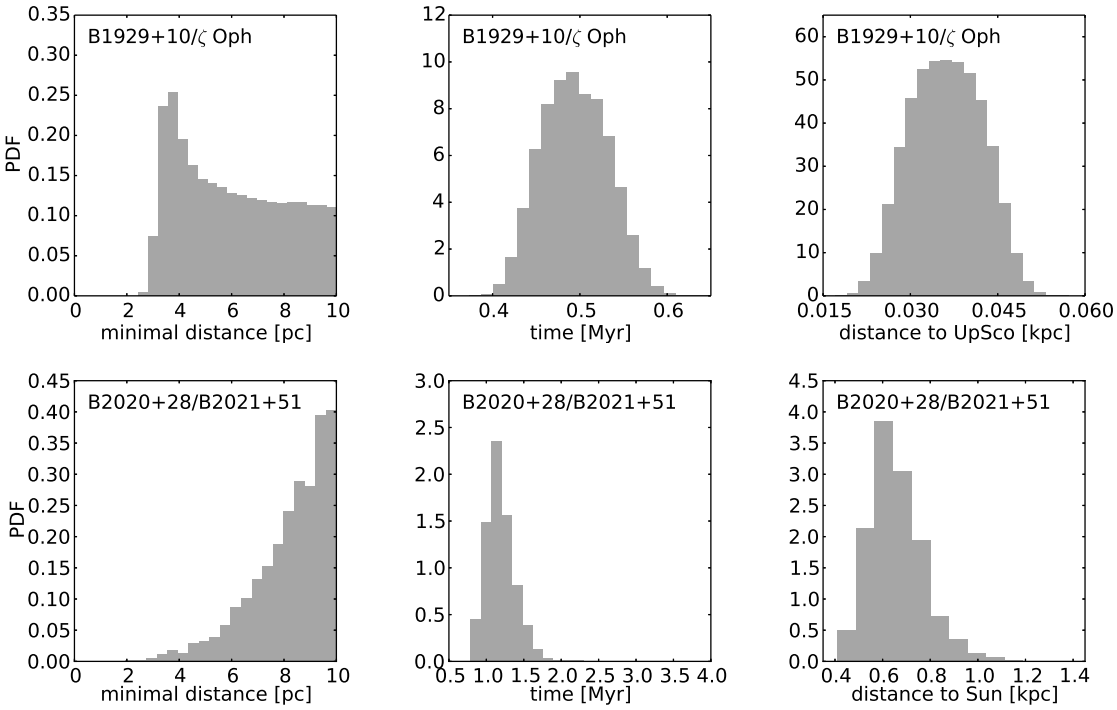

Fig. 7.5: Probability density functions of minimal distances (left column), time of minimal approach (middle column) and distance to Upper Scorpius and the Sun for B1929+10/ζ Oph (upper row) and B2020+28/B2021+51 (lower row), respectively. The stellar pair to which the figures apply is indicated in the top of each panel.

distributions[5] influence the computed trajectories, we also run the simulations for B2020+28/ B2021+51 using the input parameters for μ_α, μ_δ, and π from Vlemmings et al. (2004) (Table 7.3). In our simulations 0.14% of trajectories cross within 10 pc (minimal distance of 0.10 pc) reproducing the results of these earlier simulations well.

In the 3 million simulations that we run using our bootstrapping results for B1929+10 and the latest astrometric parameters for ζ Oph, 256855 (8.5%) orbits cross within 10 pc about 0.5 Myr ago (Figure 7.5). However, none of these orbits yield a minimum separation of less than 2.6 pc and neither the pulsar nor the runaway star approach the centre of Upper Scorpius to within less than 17 pc. The median radial velocity of B1929+10 required for it to approach ζ Oph within 10 pc is $570^{+57}_{-60}\,\mathrm{km\,s^{-1}}$ (Figure 7.6). For completeness we also test the hypothesis that B1929+10 once formed a binary system with the pulsar B1952+29 (Wright, 1979). For B1952+29 we run the simulations with $(\mu_\alpha,\ \mu_\delta,\ \pi) = (-30 \pm 6\,\mathrm{mas\,yr^{-1}},\ -34 \pm 8\,\mathrm{mas\,yr^{-1}},\ 1.4 \pm 1.0\,\mathrm{mas})$. Here, the proper motion is taken from Hobbs et al. (2004), while we translate the

[5] We use a one-component velocity distribution while Vlemmings et al. (2004) used a two-component one.

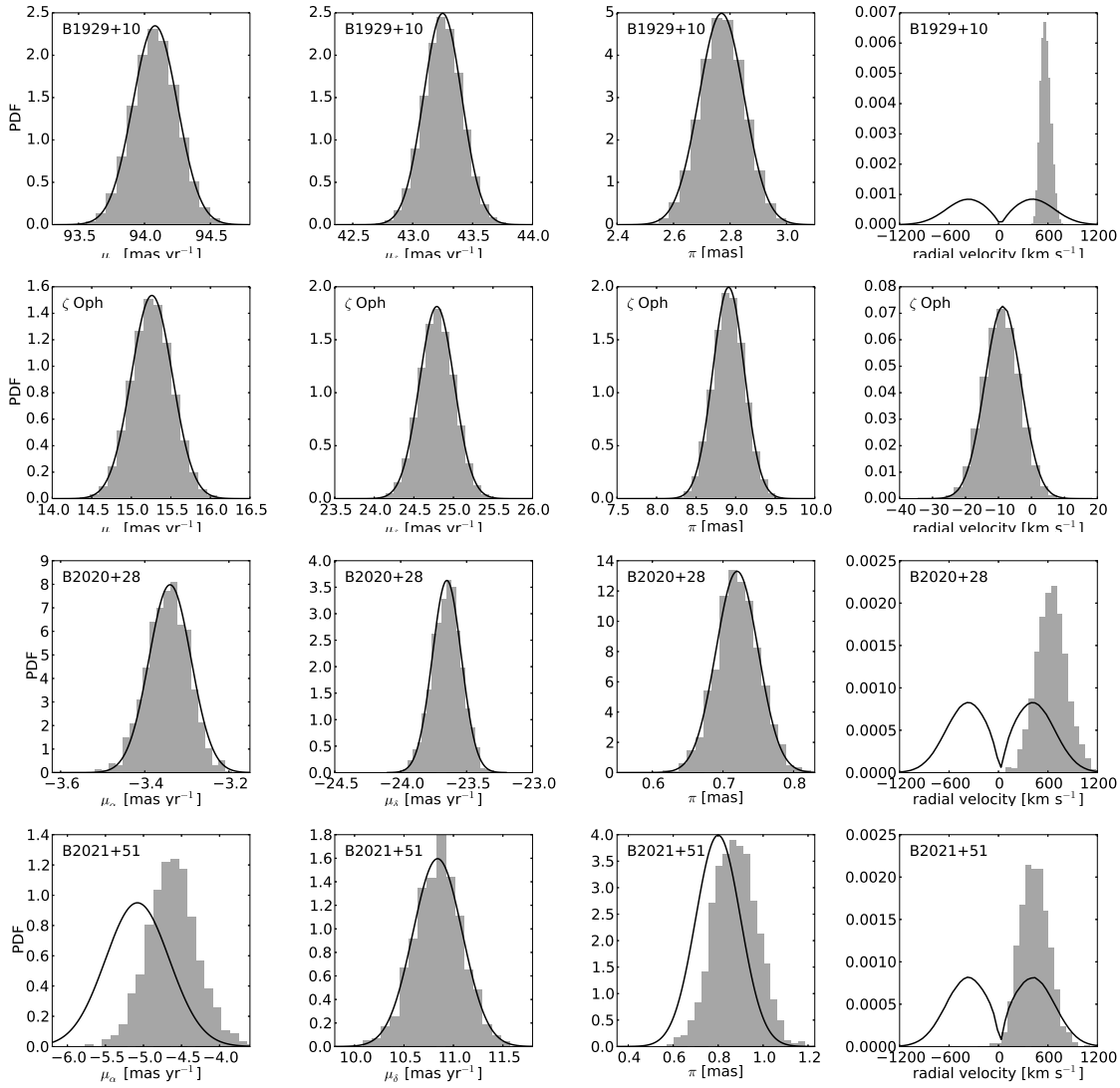

Fig. 7.6: Probability density function of astrometric parameters and required radial velocities that result in a minimum separation of less than 10 pc between B1929+10/ ζ Oph and B2020+28/ B2021+51. Objects from top to bottom are: B1929+10, ζ Oph, B2020+28, B2021+51. Columns from left to right show the results for μ_α, μ_δ, π, and $V_{\rm rad}$,respectively. For the measured parameters μ_α, μ_δ, and π, the solid lines indicate the input parameter distributions derived from assuming Gaussian errors. The solid line in the most right column indicates the input distribution for $V_{\rm rad}$ as derived from our measured transverse velocity and the empirically determined space velocity distribution derived by Hobbs et al. (2005).

distance $d = 0.7\,$kpc (based on the dispersion measure $DM = 7.932 \pm 0.007\,\mathrm{cm}^{-3}\,$pc and the Galactic electron density model from Cordes & Lazio 2003) from the ATNF Pulsar Catalogue[6] (Manchester et al., 2005) to a parallax. Lacking an official error estimate we assume an uncertainty of 1 mas. With these parameters none of the

[6]http://www.atnf.csiro.au/research/pulsar/psrcat/

simulated orbits cross within 10 pc. The same is true for simulations run with the same proper motion parameters but with the distance estimate $d = 0.42$ kpc which is based on the Galactic electron density model from Taylor & Cordes (1993).

For the putative pulsar pair B2020+28/B2021+51 our new measurements imply a minimum possible separation of 1.9 pc. Out of the 3 million trajectories, 1866 (0.06%) cross within 10 pc about $1.16^{+0.18}_{-0.17}$ Myr ago (Figure 7.5). The implied median radial velocities are 643^{+193}_{-168} and 433^{+154}_{-193} km s^{-1} for B2020+28 and B2021+51, respectively (Figure 7.6).

7.5 Discussion

7.5.1 The binary companion of B1929+10

Our new astrometric results for the pulsar B1929+10 confirm the measurements of earlier VLBI campaigns (Brisken et al., 2002; Chatterjee et al., 2004) and in combination with the previous position measurements we reduce the uncertainties of the proper motion parameters by a factor of five. Accordingly, for our adopted parallax $\pi = 2.77^{+0.07}_{-0.08}$ mas our values for the proper motion differ by more than 50σ from the parameter space that implies a common origin of B1929+10 and ζ Oph in Upper Scorpius in Hoogerwerf et al. (2001). Given the new astrometry for the pulsar and also the updated astrometric parameters for the runaway-star, the minimal possible separation of 2.6 pc between the two stars is too large to imply a common origin of both. Moreover, the closest approach of roughly 17 pc to Upper Scorpius of either of the two objects in all of the trajectories crossing within 10 pc makes this region very unlikely to be the place of common origin.

However, the fraction of simulated orbits that cross within 10 pc ($\sim 8.5\%$) is surprisingly high and implies that the orbits of both objects crossed within that distance about 0.5 Myr ago. The allowed range in radial velocities for them to pass close by, on the other hand, is very small and points to a very strong kick imparted on the pulsar at birth. Only a direct measurement of the pulsar radial velocity will further constrain the distance of closest approach of B1929+10 and ζ Oph.

Our data in combination with the updated astrometry for B1952+29 makes a binary origin of B1929+10 and B1952+29 highly implausible.

7.5.2 Common origin of B2020+28 and B2021+51

Vlemmings et al. (2004) used the astrometric parameters from Brisken et al. (2002) (Table 7.3) to infer a common origin of B2020+28 and B2021+51. Considering the 2D-motion in apparently opposite directions in Galactic coordinates (Figure 1 in Vlemmings et al. (2004)) and also the pulsars' very similar characteristic ages of 2.88 (B2020+28) and 2.75 Myr (B2021+51) such a conclusion seems likely. Nevertheless, our new parallax measurements not only place both pulsars at almost only half of the previous distance estimate, but in conjunction with our proper motion measurements a common origin is ruled out. Vlemmings et al. (2004) determined the percentage of orbits crossing within 10 pc for a known binary disrupted 1 Myr ago as a function of astrometric uncertainties (see their Figure 2). These models indicate that our improved errors should have yielded 1% of crossing orbit realization (within 10 pc) in the case of B2020+28 and B2021+51. However, in our simulations only 0.06% of trajectories cross within that distance and none of the orbits yield an approach of less than 1.9 pc. Even if we use the bootstrapping results with their larger errors from Table 7.4 only 0.08% of orbits cross within 10 pc. Furthermore, the orbits approaching each other within 10 pc do so at a median distance of $0.64^{+0.09}_{-0.11}$ kpc to the Solar System. Given the estimated extent of the Cygnus Superbubble of $0.7 - 2.5$ kpc (Vlemmings et al. (2004)), a common origin within this region is ruled out.

7.6 Conclusions

We have performed multi-epoch global VLBI observations of the pulsars B1929+10, B2020+28, and B2021+51 using the EVN at C-band. Our observations confirm previous proper motion and parallax estimates for the pulsar B1929+10, while they place the other two pulsars at almost only half of the previous distance estimate. In combination with the earlier data we measure the astrometric parameters of B1929+10 to be $(\mu_\alpha,\ \mu_\delta,\ \pi) = (94.03^{+0.02}_{-0.02}\,\mathrm{mas\,yr^{-1}},\ 43.10^{+0.03}_{-0.04}\,\mathrm{mas\,yr^{-1}},\ 2.77^{+0.07}_{-0.08}\,\mathrm{mas})$. Based on our C-band observations alone the proper motion and parallax for B2020+28 and B2021+51 are $(\mu_\alpha,\ \mu_\delta,\ \pi) = (-3.34 \pm 0.05\,\mathrm{mas\,yr^{-1}},\ -23.65 \pm 0.11\,\mathrm{mas\,yr^{-1}},\ 0.72 \pm 0.03\,\mathrm{mas})$ and $(\mu_\alpha,\ \mu_\delta,\ \pi) = (-5.08 \pm 0.42\,\mathrm{mas\,yr^{-1}},\ 10.84 \pm 0.25\,\mathrm{mas\,yr^{-1}},\ 0.80 \pm 0.11\,\mathrm{mas})$, respectively. Starting from their current positions, we use these parameters in conjunction with the pulsar space velocity distribution of Hobbs et al. (2005) to simulate the pulsars' orbits back in time through the Galactic potential. Despite earlier claims, our simulations make a common binary origin of the pulsar B1929+10 and the runaway star ζ Oph in Upper Scorpius

very unlikely. Similarly, we rule out a binary origin of the pulsars B2020+28 and B2021+51 in the Cygnus Superbubble.

References

Arzoumanian, Z., Chernoff, D. F., & Cordes, J. M. 2002, ApJ, 568, 289
Bobylev, V. V. 2008, Astronomy Letters, 34, 686
Brisken, W. F., Benson, J. M., Goss, W. M., & Thorsett, S. E. 2002, ApJ, 571, 906
Chatterjee, S., Cordes, J. M., Lazio, T. J. W., et al. 2001, ApJ, 550, 287
Chatterjee, S., Cordes, J. M., Vlemmings, W. H. T., et al. 2004, ApJ, 604, 339
Cordes, J. M. & Chernoff, D. F. 1998, ApJ, 505, 315
Cordes, J. M. & Lazio, T. J. W. 2003, ArXiv Astrophysics e-prints
de Zeeuw, P. T., Hoogerwerf, R., de Bruijne, J. H. J., Brown, A. G. A., & Blaauw, A. 1999, AJ, 117, 354
Hobbs, G., Lorimer, D. R., Lyne, A. G., & Kramer, M. 2005, MNRAS, 360, 974
Hobbs, G., Lyne, A. G., Kramer, M., Martin, C. E., & Jordan, C. 2004, MNRAS, 353, 1311
Hobbs, G. B., Edwards, R. T., & Manchester, R. N. 2006, MNRAS, 369, 655
Hoogerwerf, R., de Bruijne, J. H. J., & de Zeeuw, P. T. 2001, A&A, 365, 49
Kettenis, M., van Langevelde, H. J., Reynolds, C., & Cotton, B. 2006, in Astronomical Society of the Pacific Conference Series, Vol. 351, Astronomical Data Analysis Software and Systems XV, ed. C. Gabriel, C. Arviset, D. Ponz, & S. Enrique, 497
Kharchenko, N. V., Scholz, R.-D., Piskunov, A. E., Röser, S., & Schilbach, E. 2007, Astronomische Nachrichten, 328, 889
Manchester, R. N., Hobbs, G. B., Teoh, A., & Hobbs, M. 2005, AJ, 129, 1993
Peck, L. W. & Fenech, D. M. 2013, Astronomy and Computing, 2, 54
Scheck, L., Kifonidis, K., Janka, H.-T., & Müller, E. 2006, A&A, 457, 963
Schönrich, R. 2012, MNRAS, 427, 274
Taylor, J. H. & Cordes, J. M. 1993, ApJ, 411, 674
Tetzlaff, N., Neuhäuser, R., Hohle, M. M., & Maciejewski, G. 2010, MNRAS, 402, 2369
van Leeuwen, F. 2007, A&A, 474, 653
Vlemmings, W. H. T., Cordes, J. M., & Chatterjee, S. 2004, ApJ, 610, 402
Vlemmings, W. H. T., van Langevelde, H. J., Diamond, P. J., Habing, H. J., & Schilizzi, R. T. 2003, A&A, 407, 213
Wright, G. A. E. 1979, Nature, 277, 363

8 Phasing up global VLBI observations

Up to this point the observational technique of radio interferometry was applied in the classical way in order to perform astrometry. As part of this thesis the capabilities of the software correlator at JIVE (SFXC, Keimpema et al. 2014, in prep.) were extended to also be able to form the coherent sum of all antennas participating in global VLBI observations. With this mode of correlation, a single dish radio telescope having the collecting area of all participating telescopes together is mimicked. In this way, it provides the largest, most sensitive single dish radio telescope having full time resolution. It is this latter fact, the full time resolution, that paves the road for global VLBI to perform transient observations and, in particular, high sensitivity pulsar observations and pulsar searches. This new observing mode is entirely complementary to the Large European Array for Pulsars (LEAP[1], Ferdman et al. 2010; Kramer & Champion 2013), in which the five largest European radio telescopes are phased up. In the following, the idea and implementation of coherent summing of global VLBI observations will be introduced. The first test results and future plans will also be discussed in brief.

8.1 Implementation of coherent summing

The monochromatic signal of a point source recorded at telescope n is the real part of the complex number

$$V_n(t) = a_n \cdot e^{i\phi_n} \,, \tag{8.1}$$

where a_n is the amplitude related to the recorded voltage and $\phi_n = 2\pi\nu t$ is the phase term describing the sinusoidal nature of the signal (cf. Eq. 4.2). The power of the sum of signals recorded at two telescopes n and m arriving at slightly different times t and $t - \tau$ is given as

[1] `http://www.epta.eu.org/leap.html`

$$\begin{aligned} r(\tau) &= |V_n(t) + V_m(t-\tau)|^2 \\ &= |a_n e^{i\phi_n} + a_m e^{i\phi_m}|^2 \\ &= a_n^2 + a_m^2 + 2a_n a_m \cos(\phi_n - \phi_m) \\ &= a_n^2 + a_m^2 + 2a_n a_m \cos(\tau)\,. \end{aligned} \tag{8.2}$$

Thus, for an array consisting of N telescopes the power is

$$r(\tau_m) = \sum_{n=1}^{N} a_n^2 + 2 \sum_{n \neq m}^{N} a_n a_m \cos(\phi_n - \phi_m)\,. \tag{8.3}$$

Hence, the power output of the sum of signals is given as the sum of the auto-correlations

$$\langle V_n(t)\, V_n^*(t) \rangle = a_n^2$$

and the real part of the cross-correlations

$$Re\langle V_n(t)\, V_m^*(t) \rangle = a_n a_m \cos(\phi_n - \phi_m)\,.$$

Both the auto-correlations and the cross-correlations are the data products of standard VLBI correlation and can, in principle, simply be summed up. In order to be able to obtain the maximal power output and, thus, the coherent sum of the data of all telescopes, the signals need to be in phase, meaning that the cosine term in Eq. 8.3 needs to equal unity. Accordingly, it is essential to compute the time delays between the arrival times of a plane wave at the individual telescopes with high precision. For smaller, connected interferometers this mostly only requires an accurate geometric model and, hence, observations of this kind are routinely done at, e.g., the JVLA and the Westerbork Telescope. This phased-up data is used to include these interferometers as single stations in global VLBI experiments.

The phasing up of global VLBI observations, however, entails also knowledge about the delays caused by the dissimilar ionosphere and troposphere (cf. section 4.2) above each telescope. As the raw data from each station are first recorded on disks which are then shipped to a correlator facility[2] for correlation, no information about the differential atmospheric delays is available. Therefore, the phasing-up of an-

[2]Such as JIVE in Dwingeloo, The Netherlands, or the Max-Planck-Institut für Radioastronomie in Bonn, Germany

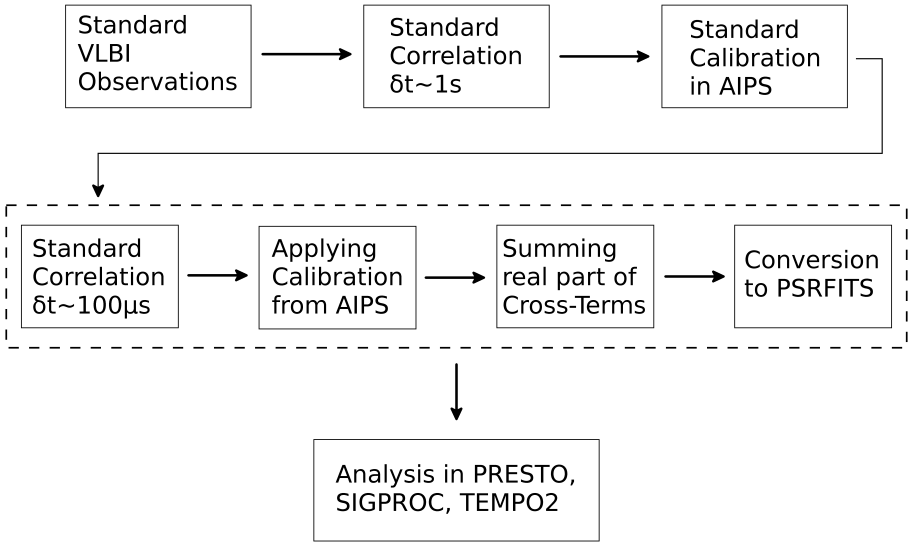

Fig. 8.1: Schematic overview of the steps involved to form the coherent sum of all antennas in a VLBI experiment that is correlated with SFXC. The dashed box indicates the newly developed part of the software.

tennas forming a global VLBI array is performed in a two-step correlation process (Figure 8.1): First, the data are correlated in the standard manner within SFCX, delivering visibilities as described in section 4.1. In the following, we will refer to this correlator output as the interferometer data. This data is then made available to the principle investigator (PI) who performs all the required calibration steps discussed in section 4.2. Thus, the observational set-up of phased-array global VLBI observations must include regular scans of a close-by phase calibrator (within a few degrees of the target) and also an extended scan of a bandpass calibrator. Once all calibration solutions have been obtained and are summarized in the standard AIPS CL- and BP-tables (cf. 4.2), those tables are sent back to JIVE. In the second correlation run, the standard auto- and cross-correlations are produced, however this time at a much higher temporal resolution $\delta t \sim 100\,\mu$s instead of the standard $\delta t \sim 1\,$s. Based on the calibration tables supplied by the PI, these correlator products are calibrated within SFXC, such that the cosine term in Eq. 8.3 is close to unity for all cross-correlations in all samples. Finally, the real parts of the cross-correlations of one integration time are summed. Below, we will refer to this data as the phased-array data. We disregard the auto-correlations from Eq. 8.3 because, unlike the cross-correlations, we expect them to be heavily affected by radio frequency interference (RFI). If required, however, the coherent sum of the auto-correlations can also be written to disk separately. In the future we will implement an antenna-based RFI-mitigation strategy within SFXC to include both the auto- and cross-correlations in the coherent sum. Additionally, we will also implement the

application of the standard AIPS flagging tables (FG-tables) that contain information on mostly baseline-based RFI. Since we tested the phased-array correlator on pulsar observations, we convert the phased-array output files to PSRFITS format (Hotan et al., 2004), thus enabling further data analysis in standard pulsar analysis software such as PRESTO[3], SIGPROC (Lorimer, 2011), and TEMPO (Hobbs et al., 2006).

In Eq. 8.2 the derivation was illustrated for a monochromatic point source. In reality, however, the expression needs to be integrated over the finite bandwidth of the observations similar to standard VLBI. As a result, the same dampening term as in Eq. 4.6 appears, limiting the sensitivity of the phased-array to sources that are close to the phase centre. In addition, similarly to standard VLBI where the field of view (FOV) of the interferometer is determined by the FOV of the largest participating antenna, the FOV in phased-array mode is determined by the longest baseline D. Hence, the FOV is limited by the pencil beam size of the interferometric array $\theta \propto \lambda/D$. Therefore, in order to detect a source of interest in the FOV of the interferometer with the phased array, the second correlation and subsequent coherent summing need to be performed at the precisely known position of a source. On the one hand, the positions for correlation are easy to determine for known sources since they can be measured directly in the image plane after Fourier inversion of the interferometric data (cf. section 4.1). While searching for pulsating objects, however, the correlation needs to be done at, ideally, $n = \Theta/\theta$ phase centres, where Θ denotes the FOV of the interferometer as determined by the largest radio telescope participating in the observations. Depending on the longest baseline and the size of the largest dish $n \sim 10^{6-8}$ if the entire FOV of the interferometer is to be probed at a separation of $\theta/2$ between phase centres. Thanks to the fringe pattern and the delay beam of the phased array (Figure 8.3), however, this number can be reduced by two to three orders of magnitude.

8.2 Performance

In typical VLBI experiments the raw data from the individual telescopes are no longer kept once they have been correlated successfully. For phased-array observations, however, this data needs to be stored until the calibration tables have been supplied and the data has been correlated a second time at the positions of all sources of interest within the FOV of the interferometer. For testing purposes we

[3] `http://www.cv.nrao.edu/~sransom/presto/`

Table 8.1: Performance test results on a three-minute scan of M15.

Number of phase centres	Number of channels	Integration time [μs]	Time factor [$t/180\,\mathrm{s}$][(a)]	Output size [GB]	PSRFITS size [GB]
1	32	256	2.63	1.5	0.165
		128	2.54	2.9	0.333
		64	2.62	5.8	0.669
	64	256	2.64	2.7	0.329
	128		2.74	5.3	0.657
	256		2.73	11	1.3
5	64	256	2.96	2.7	0.329
10			3.34		
20			4.02		
40			6.27		

Notes. [(a)] Ratio between the time taken for correlation and the time span of one observing scan (180 s).

thus kept the raw data from the individual telescopes of the seventh epoch of the global VLBI observations that were discussed in chapter 6.

The correlation was performed at Onsala Space Observatory on a cluster that consisted of five nodes with 2×8 CPUs each. The raw data from each of the seven participating telescopes (the data from the Medicina telescope turned out to be unusable) were spread over four individual disks (two stations per disk except for one station) in order to obtain the maximal data input rates for SFXC ($\sim 50\,\mathrm{MB\,s^{-1}}$ per input stream). The correlator output data was subsequently written to an independent four-disk raid system. Accounting for reading and writing processes the correlation was performed using a total of 62 CPUs. With this hardware set-up correlation was finished within roughly 2.6 times real observing time independent of the correlation parameters such as time and frequency resolution of the phased-up data (Table 8.1). The amount of output data increases with increasing resolution roughly linearly. The flexibility of SFXC also allows the correlation to be done at multiple phase centres simultaneously, the number of which is only limited by the memory of the system. In the multi-phase centre mode of SFXC, the data are correlated at one particular location specified by the user and the remaining phase centres are obtained by applying differential phase shifts to the correlated visibilities at that location. As can be seen in Table 8.1 the addition of phase centres does not decrease performance significantly which is of particular importance for the phased-array mode. Due to the pencil-beam-sized FOV of the phased-up array, the detection of a source whose location is not known with high accuracy will require

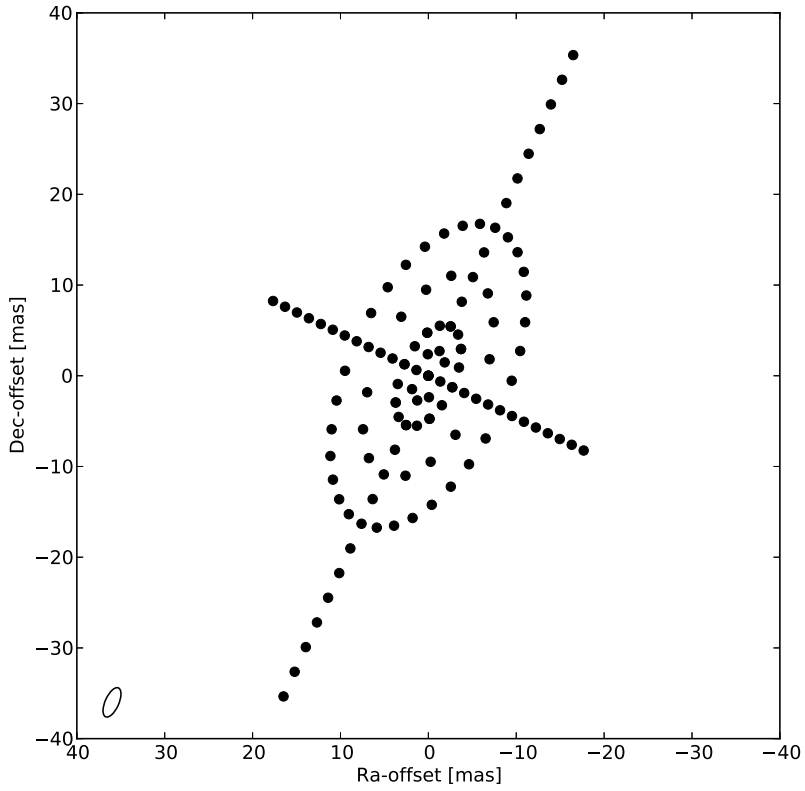

Fig. 8.2: Location of phase centres relative to the coordinates of the pulsar M15A. The small ellipse in the bottom left corner shows the size and position angle of the interferometer beam.

multiple correlator runs. With the multi-phase centre mode, however, a relatively large area can be covered during one correlator run. It needs to be noted, though, that for each correlation centre there will be a separate output file having a size as listed in Table 8.1. Similarly, each scan of the observations is correlated individually, hence also producing an output file of its own. Correlating an observation of 22 scans at 40 different locations thus produces about 2.4 TB of correlator output data, which after conversion to PSRFITS format is reduced by a factor of 8.

8.3 Mapping the beam shape

As discussed above the FOV of the phased-array is expected to be equivalent to the pencil beam size, hence the resolution, of the interferometer. In order to confirm this characteristic of the phased array we place correlation centres at regular distance intervals around the known position of the pulsar M15A and measure the obtained

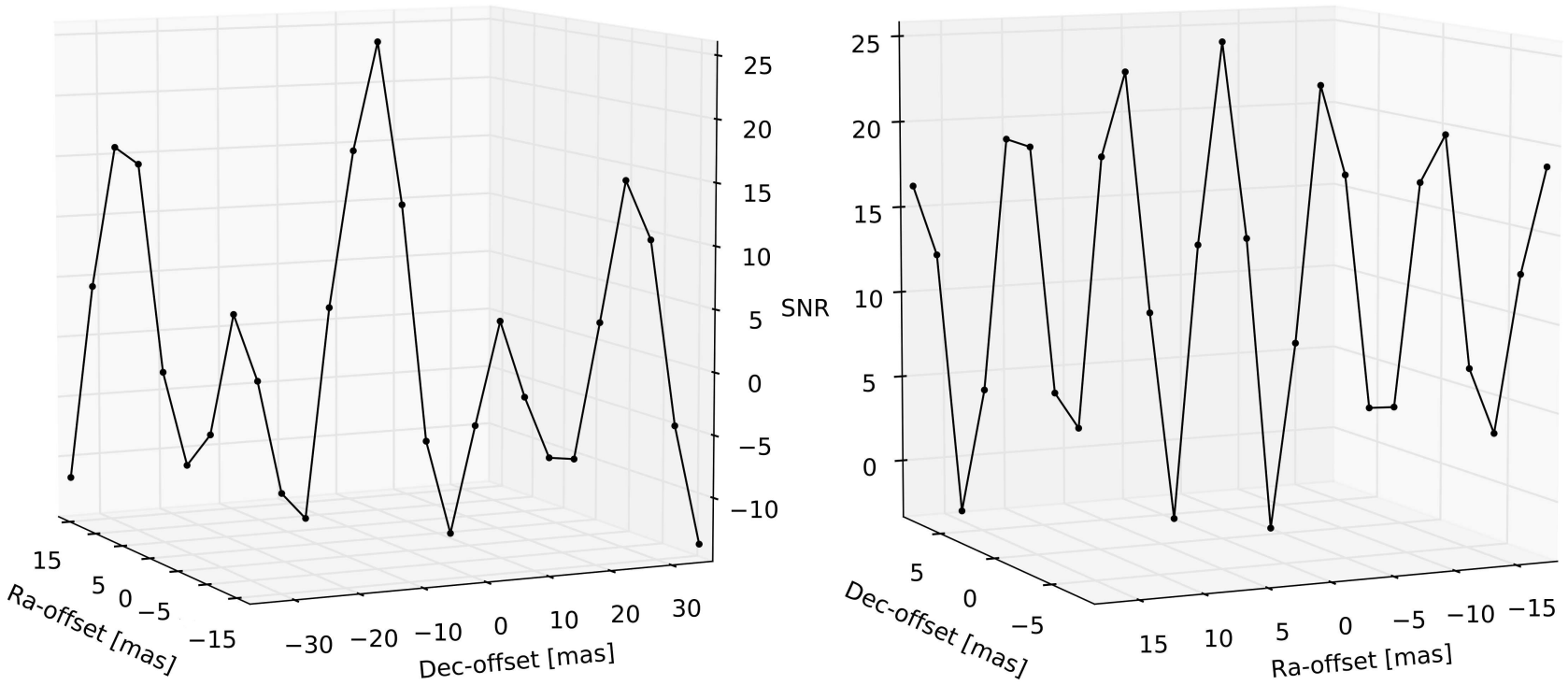

Fig. 8.3: S/N as a function of distance from the known position of M15A (located where the S/N is maximal). Data points (dots) are separated by half a beamwidth $\theta/2$. Left: View along the major axis of the interferometer beam; Right: along the minor axis. For better illustration the measurements are connected by a line .

signal-to-noise ratio (S/N). The distance intervals we chose are calculated such that they follow the elliptical shape of the interferometer beam, the size (3×7 mas) and position angle ($-25\,^\circ$) of which were determined in the image plane of the interferometric data. Along the major and minor axis of the elliptical beam we correlate the data at half the size of the interferometric beam, while off-axis phase centres are separated by two thirds of the beam size (Figure 8.2). In total we thus produce 116 correlated data sets (all of which can be correlated in one correlator run) that extend as far as 6.5 times the beam size out from the known location of the pulsar. These data sets consisting of 22 target scans each were folded with the know ephemeris of M15A and the S/N of the detections was determined from the obtained pulse profiles (cf. section 8.4). Figure 8.3 shows 3-dimensional plots along the minor and major axes of the S/N as a function of offset from the known position of M15A. As expected, half a beam size away from the central correlation centre the S/N drops to roughly half the value of that at the central location. Overall, the plots reflect the typical fringe pattern attenuated by the delay beam as already shown in Figure 4.2. The slight deviation from this pattern in the left plot of Figure 8.3 might be due to a non-ideal setting of the correlation centres along this axis.

In terms of pulsar searching campaigns, this beam shape reduces the amount of correlation centres required to map out the entire FOV of the interferometer significantly. Due to the off-axis sensitivity of the phased-up array, it suffices to place correlation centres at relative distances of ten to fifteen times the pencil beam size throughout the FOV of the interferometer. In order to avoid missing a source because of correlation at a zero (as opposed to a minimum where a source might appear in absorption and still be detectable) of the fringe pattern, a small number (~ 4) of correlation centres would need to be placed at a distance of half the pencil beam size along the major and minor axis of the interferometer beam.

8.4 First Results

The observed globular cluster M15 contains relatively bright normal pulsars and also fainter millisecond pulsars (MSPs). Furthermore, the LMXB AC211 hosts a neutron star that might be observable as a very faint pulsar and, as also discussed in section 6.4.4, there is an unclassified bright radio source within the FOV of the interferometer that might turn out to be a pulsar. Thus, this data set is ideal for first tests on known pulsars and also for searches of pulsed signals.

Table 8.2: Coordinates of correlation centres used in phased-array mode and details about pulsar parameters.

Source	Phase centre coordinates Ra	Dec	Period [ms]	Period derivative $[10^{-17}\,\mathrm{s\,s^{-1}}]$	DM $[\mathrm{cm\,pc^3}]$
M15A	21 : 29 : 58.2465883	12 : 10 : 01.2267	110.664704434(7)	−2.084(4)	67.204(5)
M15C	21 : 30 : 01.2034617	12 : 10 : 38.1501	30.529296148624(2)	0.498794(7)	67.1343(1)
AC211	21 : 29 : 58.3124032	12 : 10 : 02.6740			
S1	21 : 29 : 51.9034555	12 : 10 : 17.1324			
S2	21 : 30 : 02.0857009	12 : 09 : 04.2203			
M15B[(a)]	21 : 29 : 58.6310540	12 : 10 : 00.2608	56.133035528(3)	0.9531(9)	67.62(7)
M15D[(a)]	21 : 29 : 58.2701024	12 : 09 : 59.6950	4.802803743934(4)	−0.10679(2)	67.27(1)

Notes. [(a)]Since these sources were not detected in the continuum data (cf. section 6.3.2) their positions were taken from recent pulsar timing observation conducted between 2006 and 2009 (Ridolfi et al., private communication).

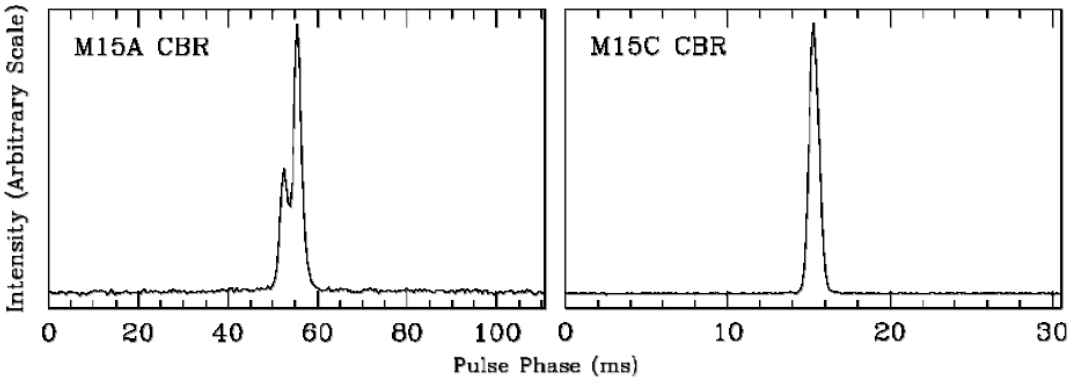

Fig. 8.4: Pulse profiles of M15A and M15C. Figures taken form Jacoby et al. (2006).

Following the steps explained in the previous section, the data were initially correlated and calibrated in the standard way. The coordinates of the phase centres for phased-array correlations were determined from a two-dimensional Gaussian fit to the brightness distribution of the detected sources in the image plane (Table 8.2). The calibration and the bandpass tables that were applied in the phased-array correlation mode were the ones computed following the description in section 6.2.2. Since the highest sensitivity of the array is obtained for observation scans in which the Arecibo telescope participates, we only consider the last two hours of the data set containing a total of 22 scans of the target cluster M15. This amounts to roughly 70 min of observational data.

We first test the algorithm on the two pulsars M15A and M15C that we clearly detect in our VLBI campaign and which also have a well known period, period derivative, and dispersion measure (Table 8.2). The two pulsars have very differing periods and pulse widths (Figure 8.4) which is why we correlate the data at a temporal resolution of 256 and 64 μs for M15A and M15C, respectively, hence sampling the individual pulses with about 40 and 32 data points. We use the software package PRESTO to dedisperse and fold the data converted to PSRFITS format using the parameters from Table 8.2. Figures 8.5 and 8.6 show the standard PRESTO plots summarizing the folding results such as the derived pulse profile and the optimized input parameters. For M15A it suffices to fold one target scan (~ 2.5 min of data) to detect the pulsar at S/N ~ 7, while for the much fainter pulsar M15C we require a minimum of five scans (~ 7.5 min) to detect the pulsar with S/N ~ 8. When we combine the entire 22 scans that Arecibo is observing the cluster we obtain S/N ~ 28 for M15A and S/N ~ 15 for M15C. Figure 8.7 shows the pulse profiles that we obtain by folding the entire 22 target scans with PRESTO. The profile of M15A seems to have less structure than the one presented in Figure 8.4 while the profile of M15C

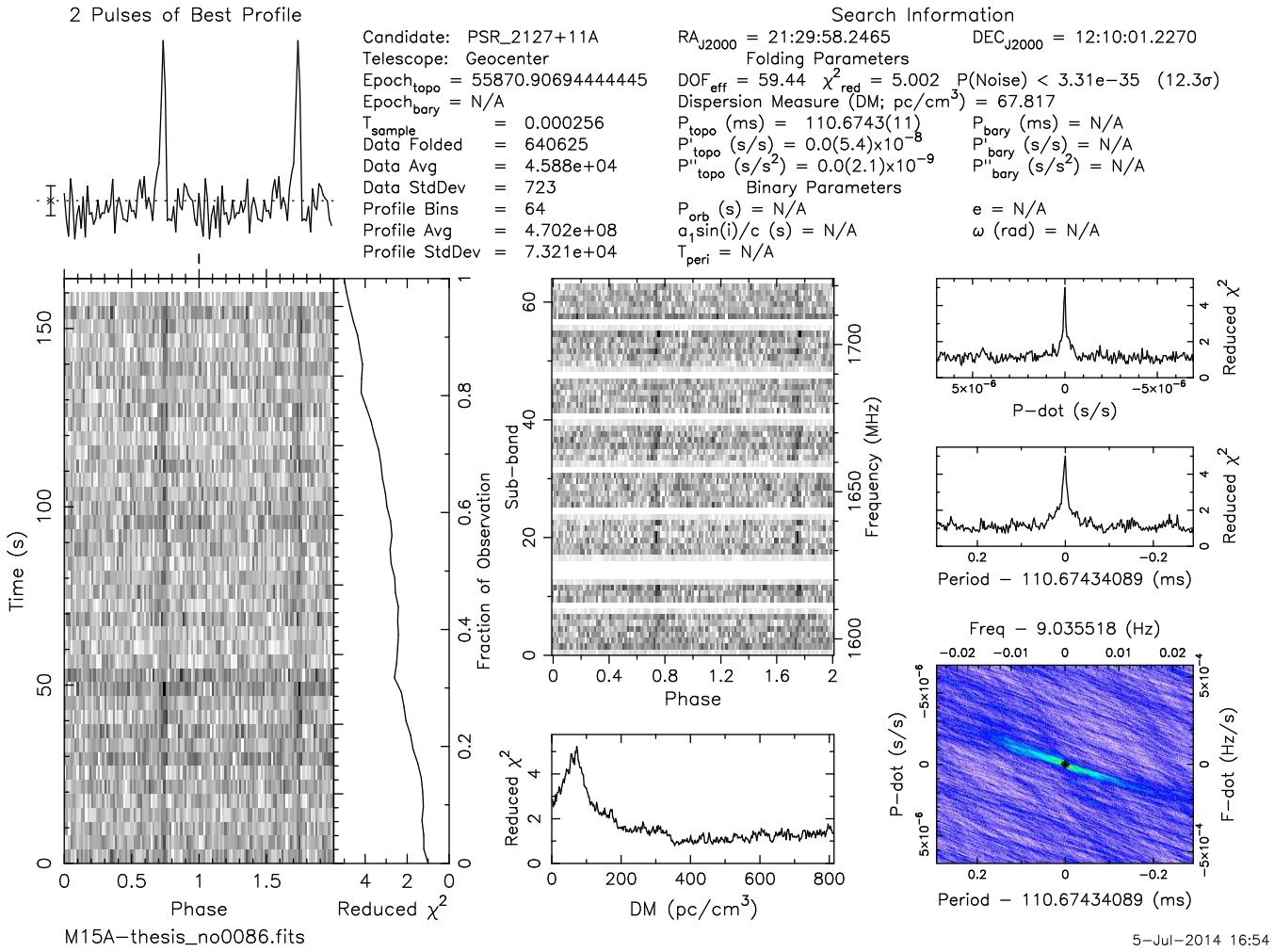

Fig. 8.5: PRESTO output plot for M15A. This plot was produced using the data from the phased-array mode. Individual plots are (from top to bottom, left to right): (1) Folded pulse profile, (2) pulse phase aligned in time, (3) dedispersed pulse signal, (4) χ^2- distribution for best fit DM, (5) χ^2- distribution for best fit period derivative $\dot{P}$, (6) χ^2- distribution for best fit period P, (7) combined χ^2- distribution for P and $\dot{P}$. The gaps in plot (3) are due to flagging of the bandpass edges of the individual IFs.

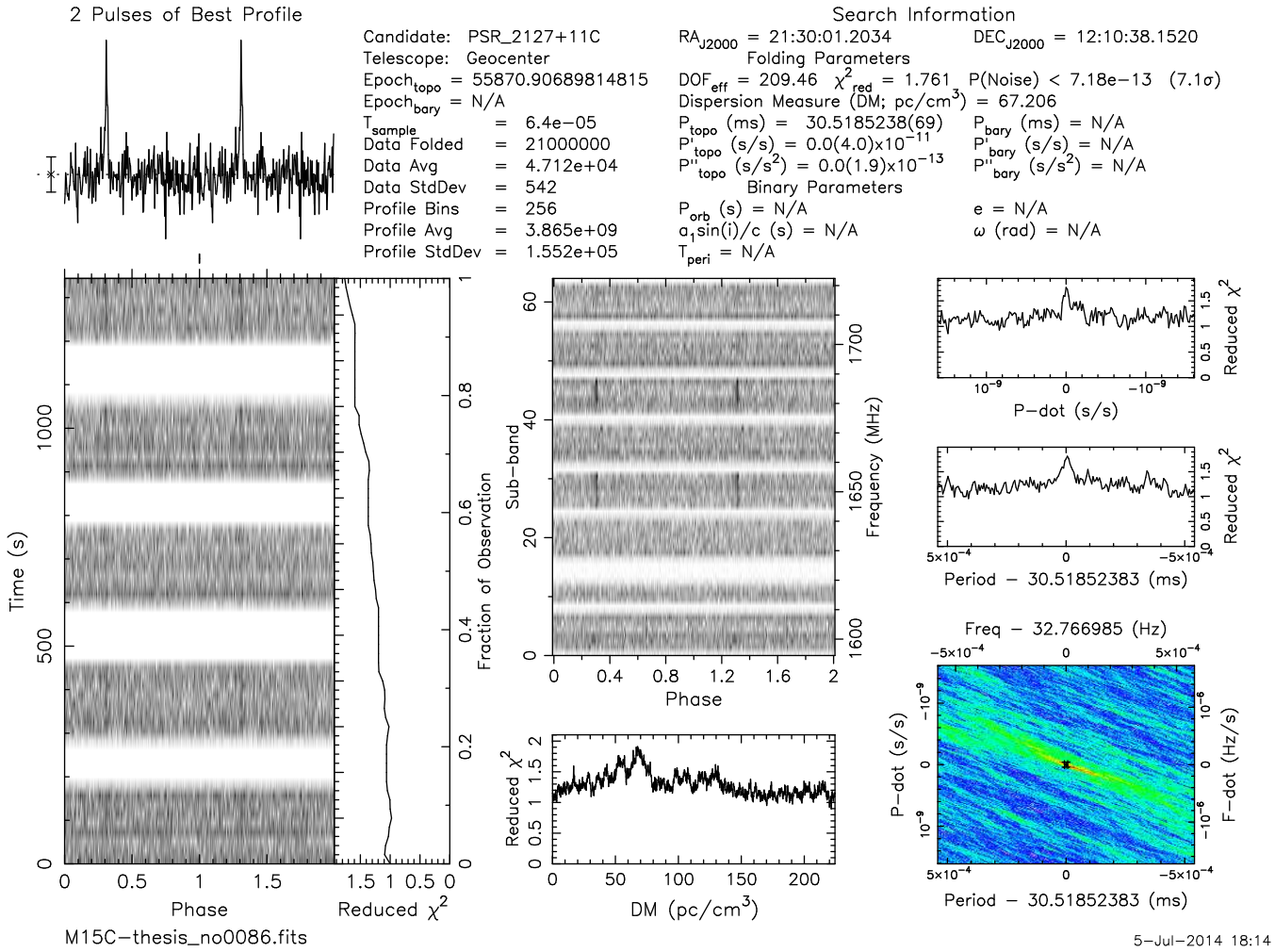

Fig. 8.6: Same as Figure 8.5 but for M15C. The gaps in plot (2) are due to scans of the phase calibrator source.

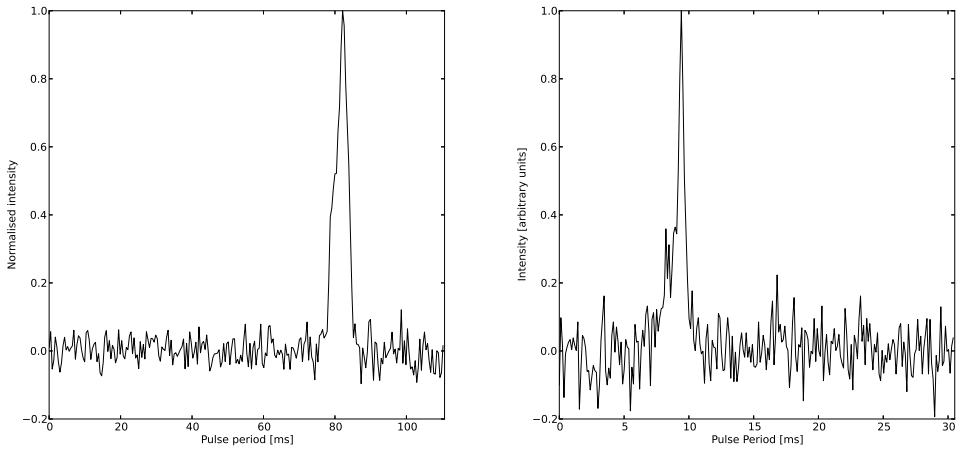

Fig. 8.7: Pulse profiles of M15A (left) and M15C (right) as obtained from folding ~ 70 min of data obtained with the phased-array mode.

seems to exhibit more structure than it does in the profile from Jacoby et al. (2006). The former cold be due to insufficient temporal resolution while the latter might either be only due to the noise background or it could be real and is caused by geodetic precession as was discussed in section 6.4.5. As expected the sensitivity of the array scales with the observing time t as $\sqrt{t}$. Similarly, we test the sensitivity as a function of total collecting area by adding more and more individual antennas to the phased-up array. This results in the linear trend (Figure 8.8) expected from the general relation $\mathrm{S/N} \propto \frac{A_{\mathrm{eff}} S_\nu \sqrt{\Delta\nu t}}{T_{\mathrm{sys}}}$, where A_{eff}, S_ν, $\Delta\nu$, T_{sys} are the effective collecting area, the flux density, the bandwidth and the system temperature, respectively.

Unfortunately, pulse searches on the remaining detected sources (Table 8.2) did not reveal any periodicity. Neither did we manage to obtain a pulse detection for the pulsars M15B and M15D. The latter can be due to either of two reasons: (i) The positions and proper motions of both pulsars are constrained with limited accuracy from pulsar timing. Therefore, we might have been correlating at the wrong positions that we determined by extrapolating the measured values to the observational epoch. We do, however, cover an area of 40×50 mas around the reported position and are confident, that we correlated at least once at the right location. (ii) The S/N that we obtain for M15A and M15C is, unfortunately, below (about a factor of 2) the one that is achievable with single dish observations with the Arecibo telescope using the standard pulsar backend WAPP.[4] Therefore, we suspect that we

[4] `http://www.naic.edu/~wapp/`, $\mathrm{S/N} \sim 25$ for M15A within 7 min of observations at 1.4 GHz and 100 MHz bandwidth.

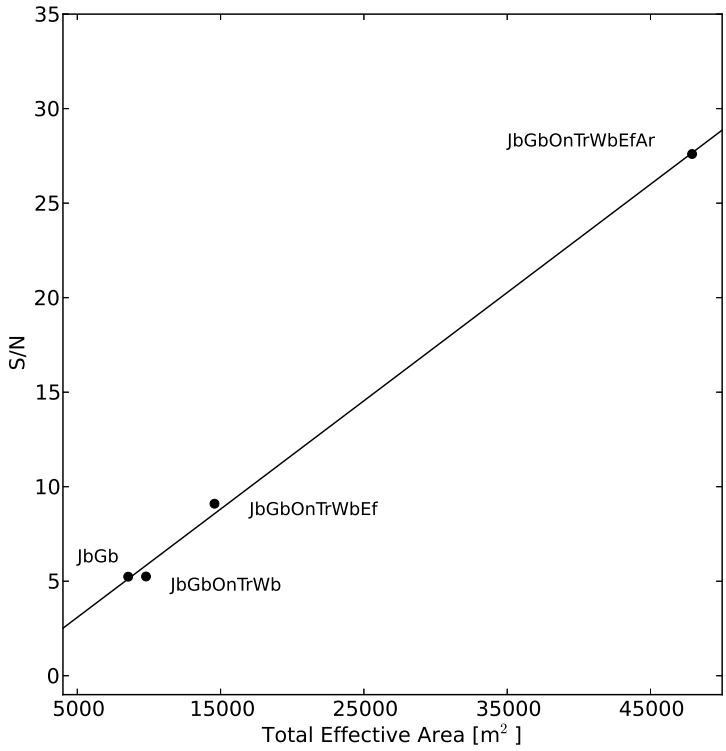

Fig. 8.8: Increase of S/N with total effective collecting area for the pulsar M15A. Dots are the S/N measurements obtained from folding 22 target scans that were correlated using the stations indicated in the figure. The solid line is a linear fit to the data points. Courtesy of Aard Keimpema.

lack in sensitivity to detect both M15B and M15D.[5] This is unexpected because besides the Arecibo telescope the array contains three 100-m class telescopes (GBT, Effelsberg, Jodrell Bank) and should, thus, be about a factor of 1.4 more sensitive than Arecibo alone. Since we kept the raw single dish data that were recorded with the standard VLBI backend, we were able to convert and fold this data to test if the correlation procedure introduces noise reducing the S/N. The signal strength we obtain from folding the single dish raw VLBI data is, however, still much lower than that obtained with typical pulsar observations at Arecibo. This indicates that it is not the correlation procedure itself, but the observational set-up and data recording strategy of VLBI observations that is causing the difference in sensitivity to pulsar signals. The exact cause for the degradation in sensitivity is still under investigation but possibilities include a non-ideal RFI situation or attenuation by the automatic gain control (AGC) or both. A further problem might be the calibration procedure

[5] Since the remaining four known pulsars in M15, M15E-H, are even fainter than M15D, we did not correlate at their positions.

lacking any polarization calibration. In fact, in order for LEAP to perform at its expected sensitivity, full polarization calibration had to be implemented (Kramer et al., private communication). The RFI might be affecting both the single dish data and also the correlated data. Once the RFI-mitigation algorithms discussed above are implemented, we expect to obtain a better S/N. In order to clarify the effect the AGC has on the VLBI data, we are planning VLBI observations with and without AGC. To investigate the issue of polarization calibration, we are also planning test observations involving a polarization calibrator source.

References

Ferdman, R. D., van Haasteren, R., Bassa, C. G., et al. 2010, Classical and Quantum Gravity, 27, 084014

Hobbs, G. B., Edwards, R. T., & Manchester, R. N. 2006, MNRAS, 369, 655

Hotan, A. W., van Straten, W., & Manchester, R. N. 2004, PASA, 21, 302

Jacoby, B. A., Cameron, P. B., Jenet, F. A., et al. 2006, ApJL, 644, L113

Kramer, M. & Champion, D. J. 2013, Classical and Quantum Gravity, 30, 224009

Lorimer, D. R. 2011, SIGPROC: Pulsar Signal Processing Programs, astrophysics Source Code Library

9 Summary and Outlook

In this thesis we have have demonstrated the versatile scientific applications of multi-epoch, high sensitivity global very long baseline interferometry (VLBI) observations of compact radio sources. The main focus was set on observations of pulsars aiming at determining their parallaxes and proper motions and implications thereof. However, the observations discussed in the previous sections, in particular in chapters 5 and 6, also revealed the power of VLBI to (i) put strong constraints on the existence of intermediate mass black holes (IMBHs) in globular clusters; and (ii) measure peculiar motions of compact radio sources with respect to their putative host environment, confirming or rejecting their association with the host. Moreover, we have developed and tested a phased-array mode for global VLBI observations, paving the way for global VLBI to enter high time resolution radio astronomy.

In chapter 5, based on the first five of a total of seven global VLBI observations of the globular cluster (GC) M15, we discussed the implications of the non-detection of a compact object at the assumed gravitational centre of M15. Such a compact object, most probably an IMBH, has been proposed to reside at the core of M15 by several authors (e.g. Newell et al., 1976; Gerssen et al., 2003). Assuming the putative IMBH to be actively accreting gas from the surrounding medium it can be expected to be visible as a compact radio moving with the global motion of the cluster. We detect no significant radio emission in any of our observations which allows us to constrain the flux density of the proposed IMBH to be below $10\,\mu$Jy at our observing frequency of 1.6 GHz. Employing the fundamental plane of black hole activity (Merloni et al., 2003; Falcke et al., 2004; Körding et al., 2006) our flux density limit implies an upper limit for the mass of the putative IMBH of $M_\bullet < 500\,\mathrm{M}_\odot$. This conservative 3σ upper mass limit is a factor of seven lower than that required to explain the dynamics of the cluster (van den Bosch et al., 2006). Therefore, we conclude that M15 most probably does not host an IMBH but that a collection of dark remnants such as white dwarfs and neutron stars resides within the central $\sim 0.05\,$pc of the cluster.

Our observations cover, however, a time span of two years only. It is possible that

the putative IMBH in M15 was inactive during our observations and that it might become observable during a period of high mass accretion rates. The close proximity of a star or compact object like a white dwarf to the central IMBH might at some point lead to a tidal disruption event. If this occurs, if a star close to the IMBH is being torn apart by tidal forces, this will lead to large amounts of mass falling onto the IMBH which, in turn, will be observable in the form of X-ray and radio emission. Further long-term monitoring of the GC in the X-ray and radio regime is necessary to clarify the constant quiescence or possible long-term variability of a putative central object in M15.

The same global VLBI observations of M15 including all seven observational epochs were discussed again in chapter 6. This time the focus was set on the implications of measured proper motions and parallaxes of all sources detected throughout the field of view of the interferometer. In total, we detected five sources: two pulsars (M15A and M15C), one low mass X-ray binary (AC211), and two thus far unclassified sources (S1 and S2, cf. chapter 6.3.1). The proper motions we measure for the known cluster members M15A, M15C, and AC211 read $(\mu_\alpha,\, \mu_\delta)_{\mathrm{M15A}} = (-0.54 \pm 0.14,\, -4.33 \pm 0.25)\,\mathrm{mas\,yr^{-1}}$, $(\mu_\alpha,\, \mu_\delta)_{\mathrm{M15C}} = (-0.75 \pm 0.09,\, -3.52 \pm 0.13)\,\mathrm{mas\,yr^{-1}}$, and $(\mu_\alpha,\, \mu_\delta)_{\mathrm{AC211}} = (-0.46 \pm 0.08,\, -4.31 \pm 0.20)\,\mathrm{mas\,yr^{-1}}$, respectively. Based on these parameters we estimate the global transverse motion of M15 as a whole to be $(\mu_\alpha,\, \mu_\delta) = (-0.58 \pm 0.18,\, -4.05 \pm 0.34)\,\mathrm{mas\,yr^{-1}}$. For S1 our position measurements are consistent with no apparent transverse motion and, accordingly, we conclude that this source is of extragalactic origin, most likely a background quasar. Knapp et al. (1996) already observed the source we call S2 in chapter 6, but the authors could not determine whether or not the object belongs to M15. We measure a parallax $\pi = 0.45 \pm 0.08\,\mathrm{mas}$ and a proper motion $(\mu_\alpha,\, \mu_\delta) = (-0.05 \pm 0.08,\, -1.27 \pm 0.17)\,\mathrm{mas\,yr^{-1}}$ for S2, which implies that the source is at a distance $d = 2.2^{+0.5}_{-0.3}\,\mathrm{kpc}$ moving at a transverse velocity $v_t^{\mathrm{S2}} = 26^{+5}_{-4}\,\mathrm{km\,s^{-1}}$ with respect to the local standard of rest. Hence, our observations indicate that S2 is a foreground source, probably a low-mass X-ray binary. Definitive proof of this hypothesis will only be possible by a detection of this source by X-ray observations. To date, however, the object has not been observed as an X-ray source, yet.

During the two-year time span covered by our VLBI campaign, the double neutron star system M15C faded beyond detection towards the middle of the observations, only to be observable again in the last of the seven epochs. Single dish follow-up observations conducted at the Arecibo telescope reveal a 2.5% phase shift in pulse arrival times compared to observations previous to the disappearance of M15C. The

most likely explanation for these observations is that due to geodetic precession the previously observable part of the patchy emission cone of the pulsar moved out of our line sight. The same effect subsequently moved a different part of the emission cone into our line of sight to the pulsar. Follow-up pulsar timing observations of all pulsars in M15 are currently under way (Ridolfi et al., in prep), aiming also at modelling the temporal evolution of M15C.

Unfortunately, despite their proximity to the cluster core ($\sim 0.07\,\mathrm{pc}$) the timespan of two years covered by our observations was insufficient to detect a signature of the orbits of M15A and AC211 about the central mass concentration of M15. One explanation might be that their orbits to a large part currently only have a radial component with respect to Earth, a notion that is supported by the surprising similarity of their transverse proper motions. It seems, however, very unlikely that both sources are on the same radial orbits. To shed light on this question further observations of the cluster, covering longer time ranges ($\sim 10\,\mathrm{yr}$) are required.

Our observations have demonstrated the potential of VLBI observations of pulsars in GCs to determine the global motion of the cluster as a whole. Globular clusters, in turn, are on an orbit about the centre of the Milky Way and as such are ideal targets to probe the Galactic gravitational field. As pulsar are very common in GCs, observations similar to the ones described in chapter 6, have the potential to map the Galactic gravitational field. Since GC pulsars are, in general, very faint and the majority of GCs hosting pulsars are only observable from the southern hemisphere, large scale campaigns of this kind will have to be postponed until the next generation telescopes such as the Square Kilometre Array (SKA) come online. Current interferometers on the southern hemisphere do not reach the required sensitivity limits.

The precise determination of pulsar parallaxes and proper motions was also the target of the observations discussed in chapter 7. The three young isolated pulsars B1929+10, B2020+28, and B2021+51 observed during this campaign were shown to have the following astrometric parameters: $(\mu_\alpha,\ \mu_\delta,\ \pi) = (94.03^{+0.02}_{-0.02}\,\mathrm{mas\,yr^{-1}}$, $43.10^{+0.03}_{-0.04}\,\mathrm{mas\,yr^{-1}}$, $2.77^{+0.07}_{-0.08}\,\mathrm{mas})$ for B1929+10, $(\mu_\alpha, \mu_\delta, \pi) = (-3.34 \pm 0.05\,\mathrm{mas\,yr^{-1}}$, $-23.65 \pm 0.11\,\mathrm{mas\,yr^{-1}}$, $0.72 \pm 0.03\,\mathrm{mas})$ for B2020+28, and $(\mu_\alpha, \mu_\delta, \pi) = (-5.08 \pm 0.42\,\mathrm{mas\,yr^{-1}}$, $10.84 \pm 0.25\,\mathrm{mas\,yr^{-1}}$, $0.80 \pm 0.11\,\mathrm{mas})$ for B2021+51. Based on these measurements and their uncertainties we performed Monte Carlo simulations tracing each pulsars' orbit back in time through the Galactic potential . The results of the simulations indicate that previous claims of a binary origin of B1929+10 and the runaway star ζ Oph in Upper Scorpius (Hoogerwerf et al., 2001; Bobylev, 2008;

Tetzlaff et al., 2010) can no longer be supported. Similarly, the proposed origin of B2020+28 and B2021+51 in a former binary system in the Cygnus Superbubble (Vlemmings et al., 2004) is ruled out by our astrometric results.

Finally, in collaboration with the Joint Institute for VLBI in Europe (VLBI), we developed and tested a phased-array mode for global VLBI observations. The scientific driver of the project was to provide the means of performing high sensitivity, high time resolution radio astronomy with global VLBI observations, potentially performing pulsar timing observations. To this end, the software correlator at JIVE (SFCX) was extended to provide a mode in which the data of all telescopes participating in global VLBI observations are coherently added instead of being cross-correlated. This observing mode is similar to what is being aimed for with the Large European Array for Pulsars[1] (e.g. Kramer & Champion, 2013), for which the five largest European radio telescopes are being phased up.
In chapter 8 we introduced the main idea of the phased-array mode, discussed its implementation, and also the first results. We could show that it is possible to detect pulsars with this new mode and that the obtained pulse profiles are in agreement with those obtained from standard single dish pulsar observations. This new mode has the potential to detect pulsars at a signal-to-noise ratio (S/N) higher that that of the largest single dish radio telescopes currently in operation and, thus, provide more accurate pulse arrival times. To date, however, the S/N we obtain is below that achievable with single dish pulsar observations at Arecibo, although the Arecibo telescope is part of the array we tested the algorithm on. The exact cause for the loss in S/N is still under investigation but might be caused either by radio frequency interference, the lack of polarization calibration, or the data recording process itself. As soon as the phased-array mode has been finalized it will be offered as a standard VLBI observing mode at JIVE. In particular timing observations of known pulsars can profit from the expected high S/N, but also exact localizations of pulsars with high levels of timing noise and accordingly poor timing solutions will be possible.

References

Bobylev, V. V. 2008, Astronomy Letters, 34, 686
Falcke, H., Körding, E., & Markoff, S. 2004, A&A, 414, 895
Gerssen, J., van der Marel, R. P., Gebhardt, K., et al. 2003, AJ, 125, 376
Hoogerwerf, R., de Bruijne, J. H. J., & de Zeeuw, P. T. 2001, A&A, 365, 49
Knapp, G. R., Gunn, J. E., Bowers, P. F., & Vasquez Poritz, J. F. 1996, ApJ, 462, 231
Körding, E., Falcke, H., & Corbel, S. 2006, A&A, 456, 439
Kramer, M. & Champion, D. J. 2013, Classical and Quantum Gravity, 30, 224009

[1] `http://www.epta.eu.org/leap.html`

Merloni, A., Heinz, S., & di Matteo, T. 2003, MNRAS, 345, 1057
Newell, B., Da Costa, G. S., & Norris, J. 1976, ApJL, 208, L55
Tetzlaff, N., Neuhäuser, R., Hohle, M. M., & Maciejewski, G. 2010, MNRAS, 402, 2369
van den Bosch, R., de Zeeuw, T., Gebhardt, K., Noyola, E., & van de Ven, G. 2006, ApJ, 641, 852
Vlemmings, W. H. T., Cordes, J. M., & Chatterjee, S. 2004, ApJ, 610, 402